UNIVERSIDADE FEDERAL DE MINAS GERAIS
ESCOLA DE ENGENHARIA
DEPARTAMENTO DE ENGENHARIA NUCLEAR

IVAN KEITI UMEZU

Computational Fluid Dynamics Modeling Methods Applied to a Lead-Cooled Nuclear Fast Reactor

Belo Horizonte

2023

Ivan Keiti Umezu

Computational Fluid Dynamics Modeling Methods Applied to a Lead-Cooled Nuclear Fast Reactor

Dissertation presented to the Graduate Program in Nuclear Sciences and Techniques at the Universidade Federal de Minas Gerais as a partial requirement for obtaining the title of Master of Science.

Supervisor: Prof. Antonella Lombardi Costa, Ph.D.
Co-supervisor: Prof. Dario Martin Godino, Dr.Eng.

Belo Horizonte

2023

Umezu, Ivan Keiti.
U48c Computational fluid dynamics modeling methods applied to a lead-cooled nuclear fast reactor [recurso eletrônico] / Ivan Keiti Umezu. - 2023.
1 recurso online (117 f. : il., color.) : pdf.

Orientadora: Antonella Lombardi Costa.
Coorientador: Dario Martin Godino.

Dissertação (mestrado) - Universidade Federal de Minas Gerais, Escola de Engenharia.

Bibliografia: f. 135-142.

Apêndices: f. 143-148.
Exigências do sistema: Adobe Acrobat Reader.

1. Engenharia nuclear - Teses. 2. Dinâmica dos fluidos computacional - Teses. 3. Materiais porosos - Teses. 4. Calor - Transmissão - Teses. 5. Reatores nucleares - Teses. I. Costa, Antonella Lombardi. II. Godino, Dario Martin. III. Universidade Federal de Minas Gerais. Escola de Engenharia. IV. Título.

CDU: 621.039(043)

Ficha catalográfica elaborada pela Bibliotecária Roseli Alves de Oliveira CRB/6 2121
Biblioteca Prof. Mário Werneck, Escola de Engenharia da UFMG

UNIVERSIDADE FEDERAL DE MINAS GERAIS

PROGRAMA DE PÓS-GRADUAÇÃO EM CIÊNCIAS E TÉCNICAS NUCLEARES

PCTN

FOLHA DE APROVAÇÃO

Computational Fluid Dynamics Modeling Methods Applied to a Lead-Cooled Nuclear Fast Reactor

IVAN KEITI UMEZU

Dissertação submetida à Banca Examinadora designada pelo Colegiado do Programa de Pós-Graduação em CIÊNCIAS E TÉCNICAS NUCLEARES, como requisito para obtenção do grau de Mestre em CIÊNCIAS E TÉCNICAS NUCLEARES, área de concentração ENGENHARIA NUCLEAR E DA ENERGIA.

Aprovada em 01 de dezembro de 2023, pela banca constituída pelos membros:

Prof.ª Antonella Lombardi Costa – Orientadora
Universidade Federal de Minas Gerais

Prof. Dario Martin Godino - Coorientador
Universidad Tecnológica Nacional / Centro de Investigación de Métodos Computacionales - CIMEC

Dr. Victor Coppo Leite
Idaho National Laboratory

Prof.ª Juliana Pacheco Duarte
University of Wisconsin-Madison

Prof.ª Maria Auxiliadora Fortini Veloso
Universidade Federal de Minas Gerais

Belo Horizonte, 1 de dezembro de 2023.

Dedico este trabalho
às minhas avós, Seko e Satiko,
aos meus pais, Elcio e Elisa,
à minha irmã Hanna
à minha querida Carol

Agradecimentos

Agradeço a Deus, fonte infinita de toda sabedoria, por sempre me permitir ver o caminho e me iluminar enquanto eu o traço.

Agradeço aos meus pais, por incentivarem minha educação e me apoiarem nas decisões que tomo.

Agradeço à Carol, por ser minha parceira, provendo seu amor e compreensão durante este período.

Agradeço à minha orientadora, Profa. Antonella, por confiar na minha visão para este projeto.

Agradeço ao meu coorientador, Dario, por acreditar na minha capacidade de executar este trabalho, e pela sua dedicação exaustiva a ele, tratando-o como seu próprio.

Agradeço à Profa. Claubia, por me orientar de todas as outras formas.

Agradeço ao Prof. Carlos, por me abrir as portas ao DEN e às oportunidades que a energia nuclear já me ofereceu, e ainda oferecerá.

Agradeço aos amigos do DEN, Nat, Cassimiro, Karytha, Isabella e Cristian pelo período de companheirismo e suporte mútuo.

Agradeço à UFMG, por ser meu lar durante tantos anos, e por me oferecer a educação que tenho hoje, e o futuro que terei.

Agradeço à AMAZUL e à Marinha do Brasil, por serem meus empregadores e permitirem que eu iniciasse minha carreira na área nuclear e concluísse este trabalho em paz.

Agradeço à CAPES pela bolsa concedida, IAEA e ICTP pelos eventos dos quais participei, e CNEN, CNPq e FAPEMIG, pelo apoio direto ao PCTN, ao DEN e a este trabalho.

"You cannot understand science and its relation to anything else unless you understand and appreciate the greater adventure of our time. You do not live in your time unless you understand that this is a tremendous adventure and a wild and exciting thing."

Richard P. Feynman, 1963

Abstract

In the current climate crisis, nuclear power, paired with renewable sources, should be one of the main technical options to decarbonize the world's electrical grids. However, to reach this, the progress of nuclear reactor technology deeply relies on efforts to make them more financially viable and (even) safer than the current operating fleet. For such, technical developments of innovative nuclear systems are underway by many public and private parties, and one of the main ongoing points concerns the development of new thermal-hydraulic design and analysis tools, including Computational Fluid Dynamics (CFD), to obtain better fluid flow visualization around complex geometries, and capture results from physical phenomena such as flow blockage, local hot spots, and thermal stratification, which help to develop more accurate models and, consequently, safer and more energy-efficient designs.

This Master's Dissertation work is dedicated to studying and proposing a set of thermal-hydraulic modeling methods in CFD, using ANSYS Fluent, to simulate the innovative nuclear system Swedish Advanced Lead Reactor (SEALER), a small modular Lead-cooled Fast Reactor (LFR). The work explores general CFD modeling aspects, such as mesh refinement studies, turbulence model selection, and boundary conditions, while also developing specific modeling strategies, as the SEALER CFD model is progressively expanded, thus dividing the work into three major parts: The first focuses on the reactor's core region, by modeling the Fuel Assemblies as porous media for the pressure drop considerations, and by implementing volume heat generation rate functions for the fission thermal power in the active regions. The second part develops the whole SEALER primary system, including modeling the pumps as boundary conditions, and the steam generators as a combination of porous media with temperature-dependent volume heat sink functions. The third and final part incorporates additional thermal considerations, by taking into account the influence of Conjugate Heat Transfer (CHT) and a combined radiative and natural convection energy loss boundary condition on the reactor vessel's outer wall. In this last part, the fuel temperature was also analyzed with respect to the influence of these additional thermal considerations.

Finally, the work concludes that the CFD modeling methods proposed in the first two parts presented themselves as adequate for the steady-state simulation of the SEALER, with detailed temperature and velocity fields that match the preliminary design data and other publications' results. The last part indicates that the additional thermal considerations do have an impact on the temperature fields inside the SEALER, however, they are not significant enough when analyzing their influence on the fuel's maximum temperatures.

Keywords: CFD; porous media; CHT; LFR; SMR; liquid metal thermal-hydraulics.

Resumo

Na atual crise climática, a energia nuclear, aliada às fontes renováveis, deverá ser uma das principais alternativas técnicas para descarbonizar as redes elétricas mundiais. No entanto, para alcançar este objetivo, o avanço da tecnologia de reatores nucleares depende profundamente de esforços para torná-los mais viáveis financeiramente e mais seguros do que a atual frota em operação. Para tal, estão em curso desenvolvimentos técnicos de sistemas nucleares inovadores por diversas entidades públicas e privadas, e um dos principais pontos diz respeito ao desenvolvimento de novas ferramentas de projeto e análise termo-hidráulicas, includindo a Dinâmica de Fluidos Computacional (CFD), para visualizar o escoamento em torno de geometrias complexas e capturar resultados de fenômenos físicos, como bloqueio de canais, *hot spots* locais, e estratificação térmica, que ajudam a desenvolver modelos mais precisos e, assim, projetos mais seguros e energeticamente eficientes.

Esta Dissertação de Mestrado dedica-se a estudar e propor um conjunto de métodos de modelagem termo-hidráulica em CFD, utilizando o ANSYS Fluent, para simular o sistema nuclear Swedish Advanced Lead Reactor (SEALER), um reator pequeno modular, rápido e refrigerado a chumbo (LFR). O trabalho explora aspectos gerais de CFD, como estudos de malha, modelos de turbulência, e condições de contorno, enquanto desenvolve estratégias de modelagem específicas, à medida que modelo do SEALER é expandido, dividindo o trabalho em três partes principais: A primeira concentra-se na região do núcleo do reator, onde este é modelado como meios porosos para a de perda de carga, acoplados a funções de potência. A segunda parte expande para todo o circuito primário, e inclui os modelos para as bombas como condições de contorno, e para os geradores de vapor como meios porosos combinados com funções de dissipador de calor. A terceira e última parte incorpora considerações térmicas adicionais, ao contemplar os efeitos da transferência de calor conjugada (CHT) e ao avaliar condições de contorno de perda de energia por radiação combinada à convecção natural na parede externa do vaso do reator. Nesta última parte, a temperatura do combustível também foi analisada referente a essas considerações térmicas adicionais.

Por fim, o trabalho conclui que os métodos de modelagem CFD apresentados nas duas primeiras partes se mostraram adequados para a simulação de estado estacionário do SEALER, e fornecem campos detalhados de temperatura e velocidade que correspondem aos dados preliminares do projeto e a resultados de outras publicações. A última parte indica que as considerações térmicas adicionais têm impacto nos campos de temperatura dentro do SEALER, porém, não são suficientemente significativas quando são analisadas as temperaturas máximas do combustível.

Palavras-chave: CFD; meios porosos; CHT; LFR; SMR; termo-hidráulica de metais líquidos.

List of Figures

List of Tables

Listings

List of Acronyms and Abbreviations

ALFRED: Advanced Lead-cooled Fast Reactor European Demonstrator

BC: Boundary Condition

CAD: Computer-Aided Design

CFD: Computational Fluid Dynamics

CFL: Courant–Friedrichs–Lewy Number

CHT: Conjugate Heat Transfer

CIMEC: Centro de Investigación em Mecánica Computacional / Center of Investigation in Computational Methods

CL: Center Line

DEN: Departamento de Engenharia Nuclear / Department of Nuclear Engineering

DHR: Decay Heat Removal

DNS: Direct Numerical Simulations

FA: Fuel Assembly

FP: Fission Products

GCI: Grid Convergence Index

GIF: Generation IV International Forum

HLM: Heavy Liquid Metal

HX: Heat Exchangers

IAEA: International Atomic Energy Agency

IEA: International Energy Agency

IPCC: Intergovernmental Panel on Climate Change

KTH: Kungliga Tekniska Högskolan - Royal Institute of Technology

LBE: Lead-Bismuth Eutectic

LES: Large Eddy Simulations

LFR: Lead-cooled Fast Reactor

LMFRs: Liquid Metal Fast Reactors

MSR: Molten Salt Reactor

MYRRHA: Multi-purpose hYbrid Research Reactor for High-tech Applications

NW: Near-Wall Mesh

Pb: Lead

PBC: Periodic Boundary Condition

PJ: Porous Jump

PM: Porous Media

RANS: Reynolds Averaged Navier-Stokes

RBC: Recirculating Boundary Condition

RC: Radiative and Natural Convection

RELAP: Reactor Excursion and Leak Analysis Program

RV: Reactor Vessel

SC: ANSYS SpaceClaim

SEALER: SwEdish Advanced LEad Reactor

SG : Steam Generator

SMR: Small Modular Reactor

STH: System Thermal-Hydraulics

TH: Thermal-Hydraulics

UFMG: Universidade Federal de Minas Gerais / Federal University of Minas Gerais

ULOF: Unprotected Loss of Flow

UNL: Universidad Nacional del Litoral / National University of Litoral

UTOP: Unprotected Trip of Power

List of Symbols

α: Porous Medium Permeability

β: Air Coefficient of Volume Expansion

Δp: Pressure drop

ΔT: Temperature Variation

δ_{th}: Thermal Boundary Layer

δ_v: Viscous Boundary Layer

ϵ: Turbulent Kinetic Energy Dissipation Rate

ε: Surface Radiative Emissivity

κ: Turbulent Kinetic Energy

μ: Dynamic Viscosity

μ_t: Turbulent Dynamic Viscosity

ν: Kinematic Viscosity

ρ: Density

σ: Stefan-Boltzmann's Constant

χ: Correction Coefficient for the Žukauskas Δp Model

ξ: Friction Coefficient for the Žukauskas Δp Model

ζ: Friction Factor for the Idelchik Δp Model

C_2: Inertial Resistance Factor

Cp: Specific Heat Capacity

d: Equivalent Diameter

$\hbar$: Convective Heat Transfer Coefficient

H: Active Fuel Height

H_e: Extrapolated Fuel Height

k: Thermal Conductivity

L: Equivalent Length

$\dot{m}$: Mass Flow Rate

Gr: Grashof Number

Nu: Nusselt Number

Pe: Péclet Number

Pr: Prandtl Number

Pr_t: Turbulent Prandtl Number

Ra: Rayleigh Number

Re: Reynolds Number

q'': Surface Heat Flux

q''': Volumetric Heat Generation Rate

Q''': Heat Sink Function

q'_0: Linear Power Axial Peak

T: Temperature

T_∞: Radiative External Temperature

T_{fs}: Convective Free Stream Temperature

T_w: Surface Temperature

Contents

Chapter 1

Introduction

As the challenge of mitigating climate change becomes increasingly more urgent, prompt action in deploying low-carbon energy sources has never been more relevant. To meet the ambitious objective set by the 2015 Paris Agreement — *to limit the temperature increase to 1.5°C above pre-industrial levels* [1] — a renewed interest in nuclear power places it as an indispensable component of the energy portfolio for nations committed to fight climate change. Nuclear energy plays a crucial role in supporting the sustainable integration of intermittent renewable sources such as wind and solar, by ensuring a dependable, on-demand, and and low-carbon energy supply [2]. Quantitatively, the significance of nuclear power in curbing emissions becomes evident in the Intergovernmental Panel on Climate Change (IPCC) Climate Change 2023 Synthesis Report, which suggests that by 2030, nuclear power has the potential to reduce net emissions by nearly 1 gigatonne of equivalent CO_2 per year compared to 2019 levels [3].

However, for nuclear to ensure its contribution to a net-zero carbon future, the International Energy Agency's (IEA) 'Net Zero by 2050 Roadmap' [4] projects that it will have to double its generation capacity, between 2020 and 2050. In agreement with this IEA Roadmap, the International Atomic Energy Agency's (IAEA) 2022 report [5] predicts that for the world's high-demand case, approximately 469 $GW(e)$ of capacity will have to be added from 2021 to 2050. This addition is equivalent to commissioning sixteen 1000 $MW(e)$ nuclear reactors every year, for twenty-nine years.

Addressing the challenge of expanding nuclear power installed capacity, particularly overcoming issues like construction costs and schedule overruns, it is fundamental to ensure the economic viability of these new energy projects. Once the large nuclear reactors (1000 $MW(e)$ or more) no longer have the economy-of-scale advantage [6], the Small Modular Reactors (SMRs), defined by the IAEA as units with an output smaller than 300 $MW(e)$

[7], have emerged as promising options. SMRs offer advantages such as 1) reduction of costs and time for the deployment of new projects, since these reactors can be factory-built and transported ready to use; 2) adaptation ease for smaller grids, which in turn reduces additional infrastructure investments; 3) enhancement of safety features; and 4) replacement for aging coal power plants, to further help the electricity grid decarbonization.

In addition to the trend towards SMR, various states and organizations are developing non-conventional nuclear reactor design technologies known as Generation IV (Gen-IV) reactors [8], whose main goals are to improve sustainability (fuel utilization and environmental impacts), economics (life-cycle costs and financial risks), safety and reliability, proliferation resistance, and physical protection (nuclear material diversion and terrorism).

The focus of this work lies in Lead Fast Reactors (LFRs) due to their interesting safety features stemming from the unique properties of molten lead as a coolant. Molten lead exhibits high thermal conductivity, density variation favorable to natural convection circulation, and elevated boiling temperature (1737 $°C$), enabling operation under low-pressure conditions and offering protection against reactivity issues associated with coolant voiding [9]. Additionally, lead provides outside shielding for γ radiation, while also having a small neutron capture cross-section, which helps sustain the fast neutron population in the core, keeping its criticality [9].

This dissertation primarily concentrates on the Thermal-Hydraulics of a Small Modular Lead-cooled Fast Reactor, using Computational Fluid Dynamics (CFD) techniques. The decision to explore this topic is motivated by the compelling blend of economic and practical advantages offered by SMRs, coupled with the technical benefits inherent in LFRs. The employment of CFD as a design tool promises valuable insights for a better understanding of these systems and, ultimately, contributes to their development by providing more precise and reliable calculation results. The following sections of this chapter will present the motivations, structure, and contributions of this work.

1.1 Motivation and Objectives

Given the challenges presented above, both for the climate crisis and for nuclear technology development, the Author searched for a field of relevance. The study of LFRs, their coolant's distinct properties, and their main simulation challenges were understood as an interesting path and a first step in the Author's career in the field of nuclear engineering. Furthermore, this work represents a substantial contribution to the ongoing research

activities at the Department of Nuclear Engineering (DEN-UFMG) of the Universidade Federal de Minas Gerais in Brazil, in collaboration with the Center of Investigation in Computational Methods (CIMEC-CONICET/UNL) of the National Scientific and Technical Research Council and the Universidad Nacional del Litoral in Argentina.

This work is an effort to contribute to the advancement of pool-type Lead Fast Reactors, by presenting a general methodology for simulating this type of reactors by using CFD tools. In the methodology proposed, the whole reactor's primary circuit (Core - Pumps - Steam Generators - Core) can be simulated under a steady-state operation condition. Although there are many strategies and current developments for steady-state simulations, the implementation of CFD tools in liquid metal reactors still has a lot to be explored, given the coolant's distinct behavior from water and the localized 3-dimensional flow details it provides.

Thus, this dissertation's general objective is to present a series of CFD modeling methods applied to simulating the hydraulic and thermal behaviors of small modular LFRs, under steady-state conditions. This general objective is mainly aimed at propagating and developing an overall understanding of the various engineering methods applicable to simulating lead-cooled nuclear systems, which are being constantly advanced by many research groups and designer companies.

To fulfill the general objective of simulating an LFR with CFD, the SEALER (**S**w**E**dish **A**dvanced **LE**ad **R**eactor) was selected as the reference system due to the availability of relevant design data, and modeled in the ANSYS Fluent R19.3 [10] [11] software installed in a single computer, with the following specifications: 2× 10-core Intel Xeon E5-2630 v4 2.20 GHz, 128 GB RAM, and 1× NVIDIA Quadro P5000 GPU. The dissertation's specific goals for this work are presented below:

- Develop a Computer-Aided Design (CAD) model of the SEALER, based on the available design data;
- Determine the CFD-related methodologies that are most suitable for addressing the problem in question. This includes defining mesh parameters through convergence studies, selecting an appropriate turbulence model, and establishing constants for both steady and transient solvers;
- Model the Fuel Assemblies (FAs) as simplified Porous Media (PM), each coupled with a power rate generation function. This approach is employed to minimize computational costs by avoiding the intricate modeling of individual fuel rods, spacing wires, and other geometrical details;

- Model the Coolant Pumps as interface Boundary Conditions (BC), that enforce fixed mass flow rate as momentum source. This simplifies the geometric complexity associated with these components.;
- Model the Steam Generators (SGs) as simplified PM coupled with Heat Sink functions, which are dependent on the coolant's temperature in the region, to balance the energy generation and dissipation in the primary loop;
- Evaluate the impact of incorporating Conjugate Heat Transfer (CHT) between solids and fluids on the reactor's temperature distribution.
- Evaluate the influence of the outside environment temperature BC on the outer Reactor Vessel (RV), through a parameter space investigation of the mixed Radiation and Natural Convection;
- Evaluate the influence of these different thermal considerations on the fuel temperatures (cladding and pellet).

1.2 Work Structure

This dissertation's structure starts with a Theory and Literature Review, in **Chapter 2**, covering some background overview on Lead Fast Reactors (LFRs), and Computational Fluid Dynamics (CFD). The work proceeds to the three main sections, which explore the SEALER modeling approaches incrementally, each with its detailed methodology, results, and conclusion sections.

Chapter 3 refers to the first step in modeling and understanding SEALER, in which its Core Barrel region (containing the Cold Pool, Core, and Hot Leg) is the domain. The main evaluations for this chapter are the porous media and power generation functions for each type of FA. Also, efforts in mesh refinement and turbulence model selection were made in this chapter, to be used in the following chapters.

Chapter 4 expands the previous model to include the Hot Pool and Cold Leg regions. For such, the coolant pumps and SGs were included. The pumps were modeled using an interface-based BC, while the SGs were modeled as a porous media with a temperature-dependent Heat Sink function. The included components were then calibrated, allowing the steady-state SEALER model to work as described in its original design. With the full SEALER primary loop complete, further investigations were possible to be carried out.

Chapter 5 implements additional thermal considerations, such as Conjugate Heat

Transfer (CHT) between fluids and solids and a simple Parameter Space Investigation to the SEALER's Reactor Vessel (RV) outer wall, where various combinations of radiation and natural convection BC are evaluated.

Chapter 6 presents the conclusions to this dissertation, the published and present works derived from the master's study period, and some future work recommendations.

Chapter 2

Background and Literature Review

This chapter presents a brief background review of the main topics related to this dissertation, i.e.: Lead-cooled Fast nuclear Reactors (LFRs), and Computational Fluid Dynamics (CFD). They are then followed by a literature and state-of-the-art review of CFD applied to LFRs.

2.1 Lead-cooled Fast Reactors - LFRs

Lead-cooled Fast Reactors (LFRs) refer to fast neutron spectrum nuclear systems whose cooling fluid is molten pure Lead (100% Pb), or Lead-Bismuth (44.5 $wt.\%$ Pb and 55.5 $wt.\%$ Bi) Eutectic alloy (LBE) [9]. Within the context of the new Generation IV reactor technologies [8], LFRs and Sodium-cooled Fast Reactors (SFRs) are the only two types of Liquid Metal Fast Reactors (LMFRs) under active research and development.

Lead's combination of neutronic and thermophysical properties allows LFRs to have some distinguished characteristics [12] for nuclear systems, such as:

1. High operating temperatures, at low pressures, due to lead's high boiling temperature (1737 $^{\circ}C$) and low vapor pressure (e.g.: 2.9×10^{-5} Pa at 400 $^{\circ}C$);
2. High thermal efficiency, due to the higher operating temperatures;
3. Low risk of core voiding due to coolant boiling;
4. Considerable thermal inertia, given lead's high heat capacity;
5. Favorable natural circulation Decay Heat Removal (DHR), due to lead's high buoyancy variation with temperature;

6. Sustained fast neutron spectrum, given the low microscopic scattering and absorption cross-sections;

7. Lead's low neutron moderation, which allows for greater pin spacing and consequently lower risk of flow blockage;

8. γ radiation shielding, and Fission Products retention up to 600 $°C$; and

9. Chemical inertness between lead and water, unlike sodium;

A general schematic of LFR systems is presented in Fig. 2.1. In pool-type LFR designs, the Heat Exchangers (HX) and pumps (when present) are located inside the reactor vessel submerged in the primary circuit's coolant. The secondary circuit is usually a traditional Rankine Cycle, when using water, or a Brayton Cycle, for gases.

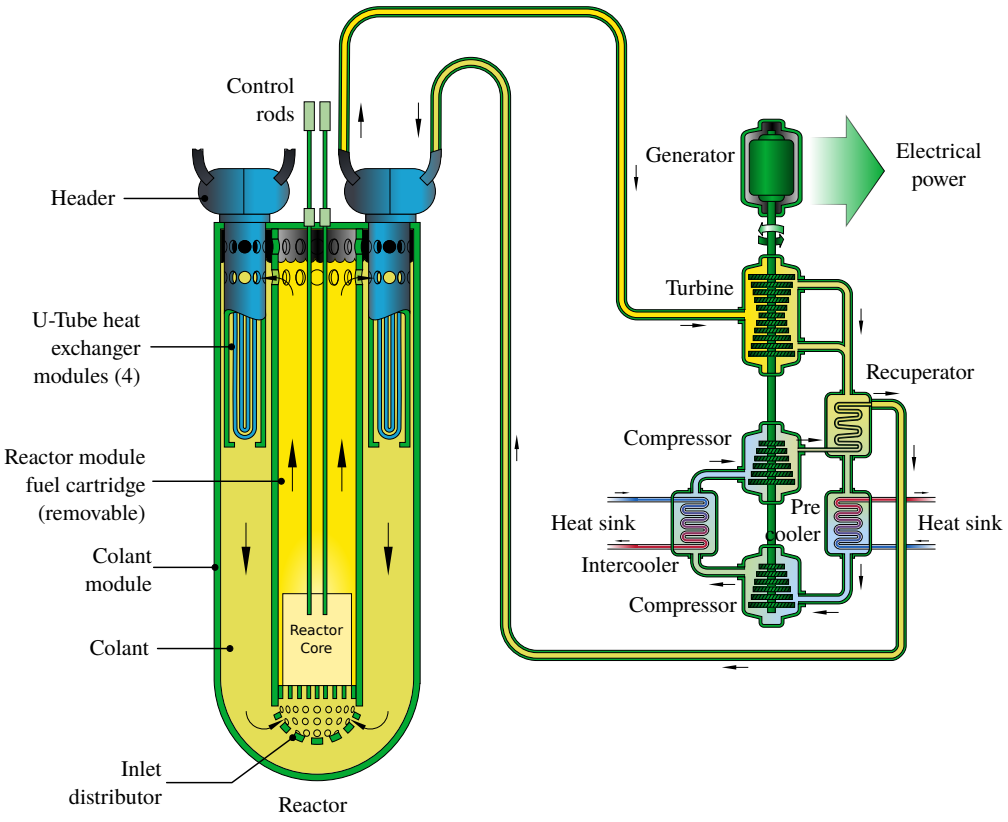

Figure 2.1: LFR general schematic [8].

Currently, several LFR designs have been proposed and are under development, as presented in Tab. 2.1, with their respective coolant type, thermal and electrical power, and designer.

Table 2.1: Current LFR designs.

Reactor	Coolant	Power [MW_{th}/MW_e]	Designer	Ref.
ALFRED	Pb	300/125	ENEA and Ansaldo Nucleare, Italy	[13], [14]
BREST-OD-300	Pb	700/300	JSC NIKIET, Russia	[15], [16]
SVBR-100	LBE	280/100	Atomenergoproekt, AKME, IPPE, Russia	[17]
ELECTRA	Pb	0.5	KTH, Sweden	[18], [19]
MYRRHA	LBE	100/-	SCK-CEN, Belgium	[20], [21]
SSTAR	Pb	45/20	LLNL and ANL, USA	[22]
SEALER Arctic	Pb	8/3	KTH and Blykalla Reaktorer, Sweden	[23]
SEALER-55	Pb	140/55	KTH and Blykalla Reaktorer, Sweden	[24]
URANUS	LBE	110/40	SNU, South Korea	[25]
LFR-AS-200	Pb	480/200	Newcleo, UK	[24]
CLEAR-I	LBE	10/-	CAS, China	[26]
Westinghouse LFR	Pb	950/450	Westinghouse, USA	[27], [28], [29]

2.1.1 Brief history of LFRs

The earliest development of LFRs dates back to 1957 when the Soviet Union Navy started the development of Project 645, which led to the first liquid-metal-cooled nuclear propulsion submarine, the K-27 [30], commissioned in 1965. Despite initial accidents and drawbacks, this pioneering design led to Project 705 Lira, which would later be known as the Alfa Class nuclear-powered attack submarines. This class of submarines was in commission between 1971 and 1996 and employed significant innovations for the time, such as an LBE-cooled nuclear reactor for naval propulsion, the first titanium alloy pressure hull, and extensive use of automation to reduce crew members. The possibility of having the highest possible power-to-weight ratio was speculated by Western intelligence to be the main reason for its development by the Soviet Navy, which indeed made the Alfa Class one the fastest submarines of all time [31]. In total, 10 naval reactors and 2 land prototypes cooled by lead/LBE were built and operated by the Soviet Union, amounting to 80 reactor-years of experience [32].

Following the 1990s, Russia continued to develop and research LFRs, however, focused on civilian energy production and technology demonstration. Basic LFR research in the United States, Europe, and Asia also started to advance around this time [33].

Interest in LFRs was renewed in the early 2000s, as they were included in the Generation IV International Forum (GIF) scope. As stated in GIF's 2021 report [8], its

LFR System Research Plan prioritizes molten lead as the reference coolant of choice, and LBE as a secondary option. Considering some of the main challenges and research needs on corrosion and fuel validation, a two-step industrial deployment is proposed: in the first step, reactors operating at lower power densities and temperatures would be deployed by 2030; in the second step, higher-performance reactors could be deployed by 2040.

2.1.2 Present technical challenges in LFRs

Throughout the recent developments of the many LFR designs, inherent technical challenges are present in most of them. Some of those could be faced before, with the experience gained from the early Soviet naval reactors, e.g.: molten lead handling, reactor decommissioning [34], and nuclear security and proliferation control [30]. As reported by [30], many of the technical issues faced with this technology arose from the lack of experience with LBE as a coolant, as the majority of the reported accidents were related to coolant leaking, freezing, corrosion, and slag formation.

Yet, those and some other technical challenges are still present but are now vastly studied and shared among the designers. The main topics are listed below, as explored by [35] [36] [37] [38] [12]:

- High melting temperature: for both lead (327 $°C$) and LBE (127 $°C$), the primary system is required to be maintained at values considerably higher than room temperature, to avoid freezing. Appropriate design configurations of the pool-type reactors, unlike the Soviet naval piped systems, can provide a safe solution to this issue. Also, designs that allow natural circulation for residual heat removal can help with the coolant freezing problem, by ensuring simultaneous safety in core passive cooling, and coolant heating;

- Opacity: the opacity of the coolant can make visual inspection, monitoring, and fuel handling difficult tasks for the operation and maintenance staff. To address this matter, some core configurations with FAs extended above the surface level have been proposed in designs like ALFRED and MYRRHA.

- High density: the large mass of whole lead-cooled systems requires more attention to mechanical design, such as for pumping systems, seismic conditions, and support and piping structural design. To address this issue, shorter reactor vessels, and seismic isolation are now incorporated into the new design proposals.

- Corrosive behavior: possibly the most challenging issue of those listed. This corrosive behavior of lead, when in contact with structural steels (e.g.: 316L SS and 15-15Ti) is further accelerated at temperatures above 500 $°C$, flow velocities above 2 m/s and higher Oxygen concentrations in the coolant. In the face of these challenges, intensive research has been dedicated to new materials for LFR applications, especially ceramic/oxide coatings for corrosion inhibition [38] and even completely new materials, such as the Alumina-Forming Austenitic Steel [39], a promising development that provides higher corrosion resistance without needing the oxide coatings.

2.1.3 Liquid lead thermophysical properties

To provide some comparative basis, Tab. 2.2 presents some basic characteristics of Lead, LBE, and water as reactor coolants:

Table 2.2: Basic characteristics of Pb, LBE, and Water as reactor coolants. Adapted from [9].

	Pb	**LBE**	**Water**
Atomic mass $[g/mol]$	207	208	18
Relative moderating power	1	0.82	421
Neutron absorption cross-section (1 MeV) $[mbarn]$	6.001	1.495	0.1056
Neutron scattering cross-section $[barn]$	6.4	6.9	3.5
Melting point at 1 atm $[°C]$	327	127	0
Boiling point at 1 atm $[°C]$	1737	1670	100

When compared with traditional cooling fluids, like water, liquid metals have a higher density, higher thermal conductivity, and lower specific heat capacity, i.e.: they conduct more heat, while not holding on to it, as opposed to water's behavior of holding the energy, while isolating its conduction. Additionally, heavy liquid metals (HLM), e.g.: lead, LBE, and mercury, have smaller values for kinematic viscosity, leading to higher values of Re for the same flow velocity [9]. The combination of these properties can be represented by the Prandtl number (Pr), as shown in Eq. 2.1.

$$Pr = \frac{\nu \cdot \rho \cdot Cp}{k} \tag{2.1}$$

This dimensionless number can be physically interpreted as the ratio between the diffusion of momentum and heat. So fluids with $Pr \sim 1$ (air, water) have both the viscous and thermal boundary layers at an equivalent thickness, Fig. 2.2 (b). In fluids with $Pr \ll 1$,

like liquid metals, the diffusion of thermal energy is larger than the diffusion of momentum, leading to a more developed thermal boundary layer in the same region, Fig. 2.2 (a). At last, in fluids with $Pr \gg 1$, like oils, the opposite happens, with a larger viscous boundary layer, when compared to the thermal one, Fig. 2.2 (c).

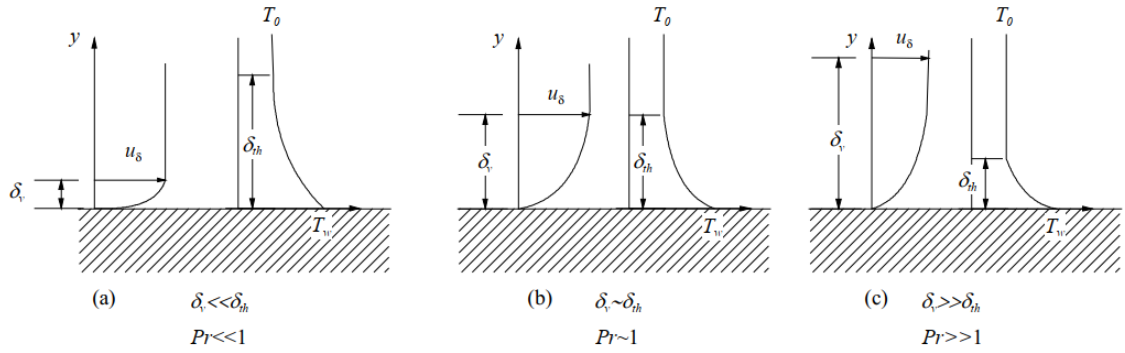

Figure 2.2: Influence of Pr on the viscous (δ_v) and thermal (δ_{th}) boundary layers over a plate. [9].

The properties presented in this Subsection, complemented by the ones presented in [9] and [40] and later in Chapter 3's Tab. 3.5, show that liquid lead as a coolant can be an interesting choice for nuclear systems. This presentation, however, is kept brief, just to bring attention to some of the relevant topics to this dissertation. And not without practical challenges, liquid lead still is vastly researched to help make LFRs feasible energy systems.

2.2 SEALER - Swedish Advanced Lead-cooled Reactor

This section will briefly describe the system of choice for this Dissertation. The SEALER was selected for two main reasons: 1) the availability of design information, which facilitated its modeling with few assumptions, and 2) its small size, which helped in keeping the computational domain small and accelerated the many cases simulated.

The acronym SEALER stands for "**S**w**E**dish **A**dvanced **L**ead-cooled **R**eactor" and is a design that arose from the experience of researchers from KTH (Kungliga Tekniska Högskolan - Royal Institute of Technology) and Blykalla Reaktorer AB (formerly LeadCold), both located in Stockholm, Sweden.

Originally presented in [23], the SEALER was proposed as a low-power system designed to meet the Arctic regions in Canada, thus its other denomination "SEALER Arctic", by offering an option for the mostly diesel-generated electricity and heat available there. Given the harsh environmental constraints, the SEALER design was approached with some distinguished requirements, such as:

- Elimination of refueling on-site, by using a core with 10 to 30 years of life;
- Small size (2.8 m diameter and 6 m height) and lightweight (30 tons), for transportation ease;
- Use of UO_2 fuel with enrichment lower than 20%, for licensing and proliferation matters.

On the descriptive side, the SEALER is a pool-type, small modular, lead-cooled fast nuclear reactor. That is, all the primary circuit is contained inside the reactor vessel, separated into inner and outer regions, where the liquid lead is heated in the core, circulated by pumps, cooled in the SGs, and returned to the core. Fig. 2.3 presents renderings of the SEALER, with indications of the main regions and components. Some of the reactor's main design parameters are presented in Tab. 2.3. For the full detailing of the SEALER's design, refer to [23].

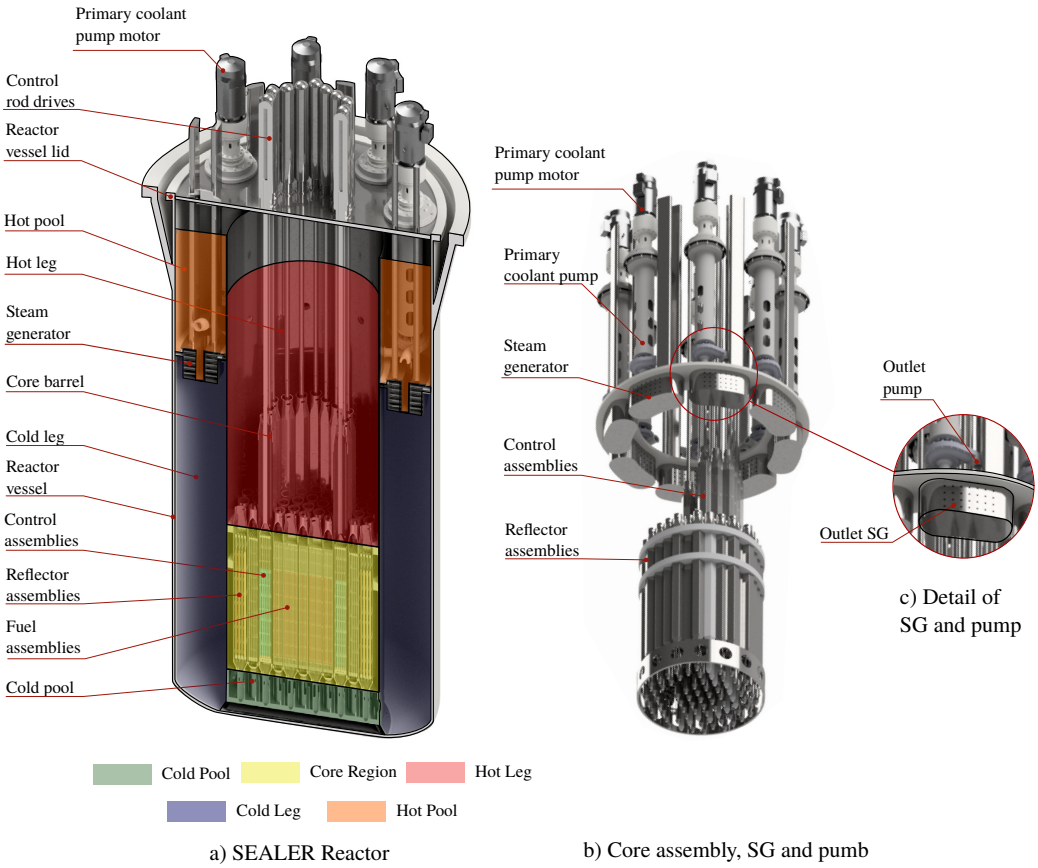

Figure 2.3: The SEALER reactor with its Core Barrel region highlighted. Source: Adapted from [23].

Table 2.3: SEALER design parameters [23].

Parameter	Value	Unit
Thermal Power	8	MW_{th}
Core average linear power	4.2	kW/m
Core inlet coolant temperature	663	K
Core outlet coolant temperature	705	K
Number of pumps	8	-
Mass flow rate of each pump	160	kg/s
Number of steam generators	8	-
Heat removal capacity of each steam generator	1	MW_{th}
Fuel composition	UO_2	-
Fuel enrichment of ^{235}U	19.75	$wt.\%$
Fuel assemblies	19	-
Fuel pins per assembly	91	-
Fuel assemblies active height	1100	mm

2.3 CFD - Computational Fluid Dynamics

Computational Fluid Dynamics (CFD) consists of a numerical technique to analyze engineering systems involving fluid flow, turbulence, mass and heat transfer, and chemical reactions. Since the 1960s, CFD has been developed and used to solve engineering problems in aerospace, combustion, aerodynamics, turbo-machinery, and nuclear power.

CFD analysis is often referred to as the process of 1) preparing (pre-processing) a physical problem, which involves modeling the geometrical domain using a CAD tool and meshing it, i.e.: dividing the domain into small grids of volume elements; 2) calculating a solution, using numerical methods and schemes to solve a set of differential equations that can describe several fluid's physical behaviors, and; 3) analyzing the results, with post-processing tool, that can aid the user to graphically visualize fields of interest, e.g.: pressure, velocity, temperature, etc., and obtain localized numerical values.

Following geometry modeling and meshing, based on the simulation setup with boundary conditions, material properties, etc., a series of algorithms and numerical methods are used to solve the applicable governing equations. In the case of this work, the Finite Volume Method (FVM) is employed, as per the default of ANSYS Fluent [11]. These equations, as presented in the following subsection are mostly coupled Partial Differential Equations (PDEs) and need to be integrated, discretized, turned into algebraic equations, and then solved by iterative methods [41]. Finally, with a converged solution, the results can be analyzed with a post-processor, in which scalar and vector field plots can be presented visually, aiding the understanding of the physical phenomena simulated.

The in-depth descriptions of the many algorithms and numerical methods are not

presented in this review, since it is not the focus of the Dissertation, however, the application of all of the steps previously described in this Section will be explored extensively in the next Chapters, as this case study encompasses a complete CFD analysis of a nuclear system.

2.3.1 Governing equations

Fluid domains

Continuum fluid flows are mathematically described using the governing equations, also known as the Navier-Stokes equations, which are a set of partial differential equations that describe the conservation of mass, momentum, and energy in a fluid. The Reynolds-Averaged Navier-Stokes equations can be written in terms of the independent variables (spatial coordinates and time) and the mean variables: pressure (p), internal energy ($\hat{u}$), or the enthalpy ($\hat{H} = \hat{u} + \frac{p}{\rho}$), velocity ($\mathbf{U}$) and density ($\rho$). Thus, the balance equations for Newtonian fluids are presented in a 3-dimensional simplified vector form as follows [41]:

- Continuity equation:

$$\frac{\partial \rho}{\partial t} + \nabla \cdot (\rho \mathbf{U}) = 0 \tag{2.2}$$

- Momentum conservation equation:

$$\frac{\partial (\rho \mathbf{U})}{\partial t} + \nabla \cdot \rho(\mathbf{U} \otimes \mathbf{U}) = -\nabla p + \nabla \cdot \tau_t + \rho g + S_m \tag{2.3}$$

- Energy conservation equation:

$$\frac{\partial (\rho \hat{u})}{\partial t} + \nabla \cdot (\rho \hat{u} \mathbf{U}) + \frac{\partial (\rho K)}{\partial t} + \nabla \cdot (\rho K \mathbf{U}) =$$

$$-\nabla \cdot \mathbf{q} - \nabla \cdot (p\mathbf{U}) - \nabla \cdot (\tau_t \mathbf{U}) + S_e \tag{2.4}$$

where $\tau_t = \tau + \tau_R$ is the turbulent stress tensor, τ is the viscous stress tensor, and τ_R is the Reynolds stress tensor. Assuming that there is a relation (eddy viscosity hypothesis) between τ, τ^R and the mean velocity $\mathbf{U}$:

$$\tau_t = \mu_{eff}[\nabla \cdot \mathbf{U} + (\nabla \cdot \mathbf{U}^T)] - \frac{2}{3}\mu_{eff}(\nabla \cdot \mathbf{U})I \tag{2.5}$$

where $\mu_{eff} = \mu + \mu_t$ is the effective viscosity, μ is the dynamic viscosity and μ_t is the turbulent viscosity. I the identity tensor, K the kinetic energy, g the acceleration of gravity,

k the thermal conductivity, and S_m and S_e are the source terms for momentum and energy equations, respectively. By introducing the Fourier law, the conductive term in the energy equation takes the following form $\mathbf{q} = -k\nabla T$.

Solid domains

For the solid domains, since no fluid-solid mechanical interaction is simulated, only the heat conduction equation is solved and the resulting equation is obtained from the energy conservation equation and the Fourier law:

$$\frac{\partial(\rho_s C_p T)}{\partial t} = \nabla \cdot (k_s \nabla T) + S_s \tag{2.6}$$

where S_s, k_s, ρ_s, and C_p are the heat generation source term, thermal conductivity, density, and heat capacity of the solid in question.

2.3.2 Turbulence modeling

Fluid flows can be primarily classified under the laminar or turbulent regimes, depending on their operating conditions. The Reynolds number (Re) is the dimensionless value that sets the separation threshold, by giving a measure of the relative importance of inertia forces and viscous forces [41].

Although laminar flow problems are simpler to solve, most applied engineering problems are turbulent, elevating the study of turbulence above theoretical interest. The need to consider these effects in CFD simulations led to the development of different turbulence models, that are added to the Navier-Stokes equations, and are indispensable if more accurate predictions of mass, momentum, and heat diffusion are expected in the numerical solving processes.

The advancement of turbulence understanding led to the development of three main categories of numerical approaches, in order of complexity representation and computational cost: Reynolds Averaged Navier-Stokes (RANS) equations, Large Eddy Simulations (LES), and Direct Numerical Simulations (DNS). Since only RANS methods are employed in this work, both LES and DNS will not be further explored in this Section.

In turbulence models for RANS, the focus is on the mean flow and the effects of turbulence on mean flow properties [41], and do not require extremely fine meshes to capture turbulent behavior, given the averaged approximations. Among the many RANS models, the $\kappa - \epsilon$ model is a 2-equation model well validated in Fluent, and adequate for this work's applications, including good predictions for flow separation and jet streams. In

this Dissertation, the Realizable $\kappa - \epsilon$ [42] variation will be the model used, as explored further in Subsection 2.3.2.

Standard $\kappa - \epsilon$

The standard $\kappa - \epsilon$ model [43] is a semi-empirical model that describes turbulence through a set of two transport PDEs, one for the turbulent kinetic energy (κ), Eq. 2.7, and one for its dissipation rate (ϵ) Eq. 2.8. Two relevant assumptions are that: the flow is fully turbulent, and the effects of molecular viscosity are negligible [10].

$$\frac{\partial(\rho\kappa)}{\partial t} + \nabla \cdot (\rho\kappa \mathbf{U}) = \nabla \cdot \left(\frac{\mu_t}{\sigma_k}\nabla\kappa\right) + 2\mu_t S.S - \rho\epsilon + S_\kappa \tag{2.7}$$

$$\frac{\partial(\rho\epsilon)}{\partial t} + \nabla \cdot (\rho\epsilon \mathbf{U}) = \nabla \cdot \left(\frac{\mu_t}{\sigma_\epsilon}\nabla\epsilon\right) + C_{1\epsilon}\frac{\epsilon}{\kappa}\mu_t S.S - C_{2\epsilon}\rho\frac{\epsilon^2}{\kappa} + S_\epsilon \tag{2.8}$$

where μ_t is the turbulent viscosity and is defined by Eq. 2.9:

$$\mu_t = \rho C_\mu \frac{\kappa^2}{\epsilon} \tag{2.9}$$

The model constants in equations 2.7, 2.8 and 2.9 are by default [44] :

$$C_\mu = 0.09 \qquad C_{1\epsilon} = 1.44 \qquad C_{2\epsilon} = 1.92$$

$$\sigma_k = 1.0 \qquad \sigma_\epsilon = 1.3$$

$C_{1\epsilon}$ and $C_{2\epsilon}$ allow for the correct proportionality between the terms in Eq. 2.7 and Eq. 2.8. σ_k and σ_ϵ are the turbulent Prandtl numbers for κ and ϵ that connect the diffusivities to the turbulent viscosity μ_t. S_κ and S_ϵ are the user-defined source terms. S is the modulus of the mean rate-of-strain tensor. epsilon

Realizable $\kappa - \epsilon$

The Realizable $\kappa - \epsilon$ model was proposed by [42] and improved the original $\kappa - \epsilon$ model by adopting the following [10]:

- A new formulation for eddy-viscosity formula involving a variable C_μ; and
- A new model equation for dissipation (ϵ), using the dynamic equation of the mean-square vorticity fluctuation.

The model has the assessed benefits of providing better predictions for the spreading rate of planar and circular jets, and also better performance in simulating flows involving rotation, boundary layer separation, and recirculation. This model is referred to as "realizable" because it can satisfy some mathematical constraints on the Reynolds stresses, making it more consistent with the physics of turbulent flows, unlike the previous $\kappa - \epsilon$. Since the κ equation remains unaltered, the new ϵ takes the form of 2.10. The following mathematical notation is taken from the ANSYS Fluent's Theory Guide [10], since those are the actual equations solved in this dissertation :

$$\frac{\partial(\rho\epsilon)}{\partial t} + \nabla \cdot (\rho\epsilon \mathbf{U}) = \nabla \cdot \left(\frac{\mu_t}{\sigma_\epsilon}\nabla\epsilon\right) + \rho C_{1\epsilon} S_\epsilon - \rho C_{2\epsilon}\frac{\epsilon^2}{\kappa + \sqrt{\nu\epsilon}} + S_\epsilon \tag{2.10}$$

where the $C_{1\epsilon}$ coefficient is:

$$C_{1\epsilon} = \max\left[0.43, \frac{\eta}{\eta + 5}\right], \quad \eta = S\frac{\kappa}{\epsilon}, \quad S = \sqrt{2S_{ij}S_{ij}}$$

The model's constants are:

$$C_{2\epsilon} = 1.9, \quad \sigma_\kappa = 1.0, \quad \sigma_\epsilon = 1.2$$

The difference in the C_μ in the Realizable $\kappa - \epsilon$ is that it is no longer a constant, but a function of the mean strain and rotation rates, system angular velocity, and the turbulence fields (κ and ϵ), as presented in Eq. 2.11 and its additional relations below.

$$C_\mu = \frac{1}{A_0 + A_s\frac{\kappa U^*}{\epsilon}} \tag{2.11}$$

where

$$U^* \equiv \sqrt{S_{ij}S_{ij} + \tilde{\Omega}_{ij}\tilde{\Omega}_{ij}}$$

and

$$\tilde{\Omega}_{ij} = \Omega_{ij} - 2\epsilon_{ijk}\omega_k$$

$$\Omega_{ij} = \bar{\Omega}_{ij} - \epsilon_{ijk}\omega_k$$

where $\bar{\Omega}_{ij}$ is the tensor for the mean rate of rotation, viewed in a rotating reference frame with the angular velocity ω_κ. The constants A_0 and A_s are given by:

$$A_0 = 4.04, \quad A_s = \sqrt{6}\cos\phi$$

where

$$\phi = \frac{1}{3}\cos^{-1}(\sqrt{6}W), \quad W = \frac{S_{ij}S_{jk}S_{ik}}{\tilde{S}^3}, \quad S_{ij} = \frac{1}{2}\left(\frac{\partial u_j}{\partial x_i} + \frac{\partial u_i}{\partial x_j}\right)$$

2.3.3 Modeling low-Prandtl number fluids

When computationally modeling low-Prandtl metallic fluids, like lead, contained in large volumes, some aspects require attention, to avoid known over-simplifications and mistakes in the model.

The use of temperature-dependent properties should be preferred in cases with significant temperature variations. This is mainly relevant to the density, which can vary greatly in heavy liquid metals, making natural convection a significant phenomenon. This large density variation renders the Boussinesq Approximation invalid for simulating large volumes of liquid lead [45] [46] [47]. Thus, it is recommended to use a function for $\rho(T)$ instead;

When simulating with Reynolds Averaged Navier Stokes turbulence models, the Turbulent Prandtl (Pr_t) number constant should be modified to values larger than unity. This has been long discussed [48] [49] [50] [51] and is mostly justified by the reason that the Reynolds Analogy is not valid for low-Prandtl fluids and also because the Pr_t values in turbulence models were mostly empirically obtained with conventional fluids experiments.

In short, the Pr_t is analogous to the Pr, but refers to the ratio of eddy diffusivity of momentum and enthalpy. Most recent studies of comparison between Direct Numerical Solution (DNS) and Large Eddy Simulation (LES) references with modified Pr_t RANS cases indicate that values of $1.5 - 2.0$ can lead to better agreement. However, this area of CFD modeling is still under study and, possibly, completely new models will have to be developed and implemented to address this matter.

2.4 Thermal-hydraulics advancements in LFRs

The last Section of this Chapter presents a review and the state-of-the-art on the use of CFD to help develop nuclear reactor thermal-hydraulics research, focused on LFRs.

As presented in [52]'s review of 40 years of nuclear thermal-hydraulics, along with its experimental advancements, the computational evaluations also came a long way. The system analysis codes, e.g.: RELAP, TRACE, CATHARE, etc., were essential in the development of mainly water-cooled reactors starting in the 1980s. Although these codes have been widely used, developed, and trusted by reactor designers and regulators, they still have some limitations. Aside from the lack of user-interface friendliness (which can impact simulation case preparation efficiency), these codes cannot provide local flow details, given their component-based nature for simulating large systems. This deficiency should

not be overshadowed by their power and computational efficiency in providing general and valuable information, such as in power transients, accidents, and neutronic coupling, for example.

Also in the 1980s, CFD as a tool for nuclear thermal-hydraulics started to gain attention, not only due to its already-mentioned new benefits but also because of the possibility of being coupled to traditional STH codes, which meant that models could be modeled with STH where it is beneficial to, e.g.: FAs and HXs, and modeled with CFD where detailed 3-D results are of interest, e.g.: plena and pools. However, as described by [52], not until the 2000s that CFD could start being explored by the nuclear community with turbulence modeling limited to Reynolds Averaged Navier Stokes (RANS) approaches and, when considered large scale, domains would not surpass 10^6 volume cells.

From the 2000s into the 2020s, with the 10^5 times increase in computational power, CFD could be explored more fully in the new nuclear reactor design applications, which now can enjoy the newly found possibilities of visualizing detailed flow patterns around complex geometries, identifying abnormal temperature distribution phenomena, e.g.: hot-spots, boiling, local thermal stratification, flow-induced vibrations [53], etc. Along with general purposes CFD codes, like ANSYS Fluent [10] [11], specific CFD codes for nuclear have been developed, like GeN-FOAM [54] [55], which brings multiphysics for neutronic, mechanical deformations, fuel analysis, and porous models calculation packages, and others, to enhance its general applicability and to nuclear open source research.

In the context of LFR development, the rise of CFD matched many of its development needs [56] [57], by allowing the design and understanding of coolant flow without the exhaustive need for prototypes and mock-ups, not only saving initial design costs and time but also avoiding accidents, as happened with the first naval LFRs [31] [30].

Some of the general whole-system CFD simulations of LFRs include the European studies for the MYRRHA [58] [59] [60] [61] [62], ALFRED [63], as well as some experimental facilities, such as E-SCAPE [64] [65], TALL-3D and CIRCE [63]. These works, and many others brought experiment validation support, and a strong sense of the CFD visualizing powers to those systems cooled by lead, which is completely opaque.

By taking advantage of smaller domains, the mesh refinement can be compensated in computationally restricted conditions (nonetheless under rapid expansion). Naturally, with more computing power, new explorations to high-fidelity simulations of rod bundles, spacers, and wire-wrapped assemblies (e.g.: for MYRRHA [66] [67], BREST-OD-300 [68] [69], ALFRED [70] and general wire-wrapped assemblies [71] [72]). Also, validation works

could be explored in the context of RANS cases against LES and DNS simulations and physical experiments [73] [74] [49] [75].

Finally, the ultimate efforts for high-fidelity CFD have been dedicated to allowing its application to large domains, by combining the advantage of high-power computing (HPC) and novel efficient solver codes, e.g.: GPU computing-oriented solvers to accelerate the simulations. [76] [50] [53] [75] [77]. In the following years, considering the observed steady fast-paced growth, conditions will be favorable for high-fidelity CFD to enhance the quality of nuclear design, and safety analysis, to ultimately assist the faster licensing and deployment of new projects.

Within the context of this dissertation, the SEALER system has been simulated using CFD tools in some works, such as [24] [78] [79], under steady and transient working conditions. However, all three main references employed some simplifications and considerations of their own, which the Author saw as opportunities to explore or develop further. For instance, in [24] significant geometry simplifications were made, which have impacts on the flow distribution in some of the SEALER's regions, and limited information on the methods was disclosed (due to commercial reasons, supposedly). In [78] and [79], heat transfer between different regions through solid walls, i.e.: CHT, was not considered, the Steam Generators were simplified in geometry and function, and considerations on energy loss to the domain's outside were absent. This work is an attempt to address some of those open matters regarding the SEALER's CFD modeling strategies, and to contribute to the knowledge on LFR CFD simulations.

Chapter 3

Core Barrel Region Analysis

3.1 Motivation and objectives

As described in Chapter 1, the SEALER CFD analysis was split into three steps, this being its first. In this Chapter, the SEALER's core barrel region is simplified to a quarter and simulated in a steady-state condition. Fig. 2.3 presents this region highlighted. The Cold Pool is in blue, the Core in yellow and the Hot Leg in red.

As this Chapter is mainly focused on modeling the core region, porous jumps and porous media methods were employed to account for the pressure drops along the FAs, and heat generation functions were applied to their active regions. Besides the specific modeling methodologies used in the core, other important analyses for this dissertation were carried out, such as turbulence model selection, mesh size definition, and symmetry boundary condition adequacy, all to be employed further in the next Chapters.

The main motivation of this Chapter is to present the validation of the methods chosen for modeling SEALER's core and to evaluate general CFD approaches to be used in the whole domain in the following Chapters.

3.2 Methodology

The methodology outlined in this chapter follows a sequence of steps, beginning with the geometric modeling of the domain, proceeding to the determination of momentum sink coefficients (for porous jumps and media), and concluding with the definition of the power distribution functions, both of which are reached analytically.

The steps developed in this chapter comprehensively address the essential aspects of CFD, from the selection of the turbulence model to the generation and refinement of the mesh, whose parameters are used in subsequent chapters.

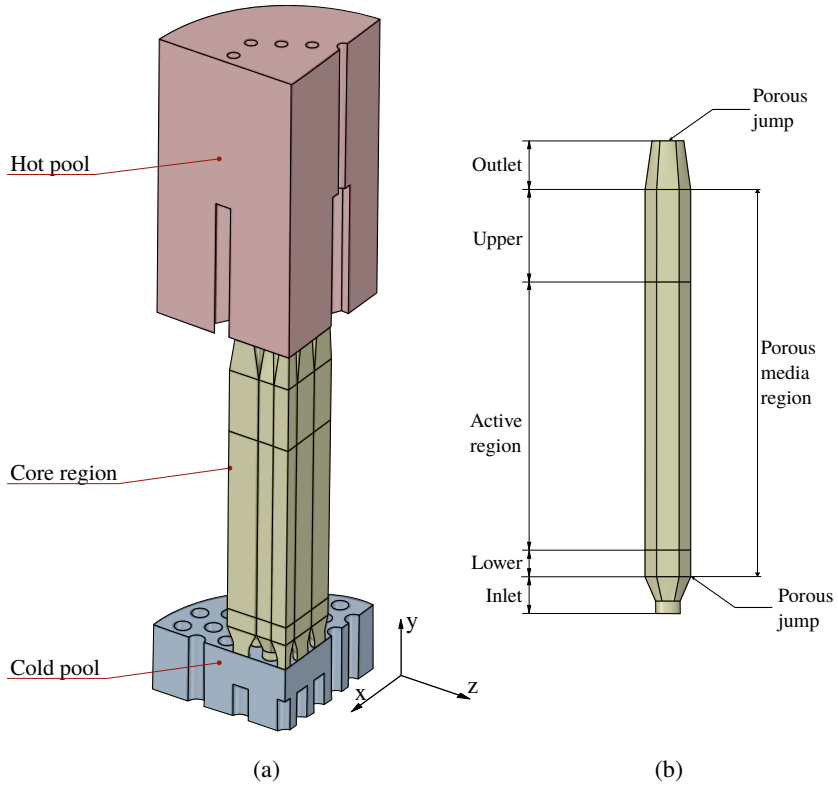

Figure 3.1: SpaceClaim CAD used in this Chapter: (a) SEALER reactor and (b) FA height divisions.

The validation of the CFD approach involves several stages, including mesh definition and final result validation, all conducted with a 1/4 model utilizing a steady-state solver for initial conditions, then stabilizing the results with a transient solver. This chapter serves the dual purpose of establishing the mesh size to be employed in forthcoming Chapters and validating the engineering methodologies applied to model the SEALER core.

3.2.1 Geometry description and assumptions

To perform the simulations outlined in this section, it was necessary to first establish a common geometry model. The CAD model was developed using SolidWorks and was based on the available geometry data from the original SEALER design references [23] [80]. Certain simplifications were introduced to accelerate the convergence of the CFD cases while preserving the overall quality of the results. Subsequently, the CAD model from SolidWorks was imported into ANSYS SpaceClaim (SC) to assign names and tags to the fluid regions and domain boundaries. Figure 3.1 (a) depicts the CAD model in ANSYS SC.

The main geometry simplifications were applied to the core region, particularly by excluding individual fuel pins and support structures. Since the porous media approach was chosen, the volume equivalent to the fuel assemblies had to be modeled anyway. This means that the inner volumes inside the hexagonal fuel assembly wrappers were considered as the

fuel assemblies themselves. Details on porosity and momentum loss inside these volumes are presented in the next Section in more depth. This way of modeling fuel assemblies has been widely employed [81] [62] [82] [24] when simulating full reactor systems, as the mesh size required to capture small-scale fluid flow behaviors would be computationally prohibitive.

For each modeled FA, its total height was divided into five regions: inlet, lower, active, upper, and outlet, presented in Fig. 3.1 (b). The lower, active, and upper regions represent the heights containing the fuel rods where porous media is applied. For the active region, in particular, power distribution functions were also applied. The inlet and outlet FA regions were considered simple fluid regions only. However, their contributions to the CFD model come from their geometry, in which their cross-sections change from circular to hexagonal. This change has implications for the velocity and pressure fields that cannot be ignored.

Although this approach of modeling the fuel assemblies as volumes was chosen, not all assemblies were modeled in this way. The assemblies used for the reactor's control rods, shielding, and reflectors were not included since they account for almost null fluid flow given their highly constricted inlets and also do not contribute to the coolant's heating. These assemblies will later be modeled as static lead volumes in Chapter 5.

In the cold pool region, the assemblies' cylindrical inlets (also referred to as 'feet' in [23]) were modeled as non-slip walls since they were considered relevant for the average velocity in this region, and their absence could impact the coolant's behavior around the fuel assemblies' inlets. However, there were differences between the fuel assemblies and the other foot structures. For the fuel assemblies, the upper half of the feet was not modeled as walls since it would lead to a more complex mesh, and no dimensional data was available for this option. Modeling most of the feet structures outside the fuel core region was already significant for improving the model quality in this region. Fig. 3.2 (a) and Fig. 3.2 (b) present the isolated Cold Pool region, where the FA feet at half height can be observed, as well as the region's space distribution with the feet from the other assemblies, which were modeled in full as non-slip walls. The FA orifices are internal surfaces that allow fluid to flow up the FAs.

In the Hot Leg region, the most noticeable geometry features are the control rod auxiliary structures, such as the hexagonal wrapper extension and the control actuation rods, which were considered walls, as presented in Fig. 3.3. This choice was based on the understanding that these structures have a relevant impact on the flow distribution in this

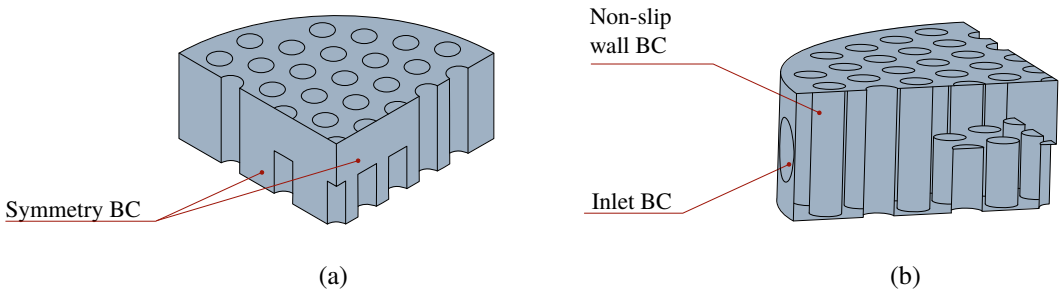

Figure 3.2: Cold pool region - (a) External surface and (b) Inner walls.

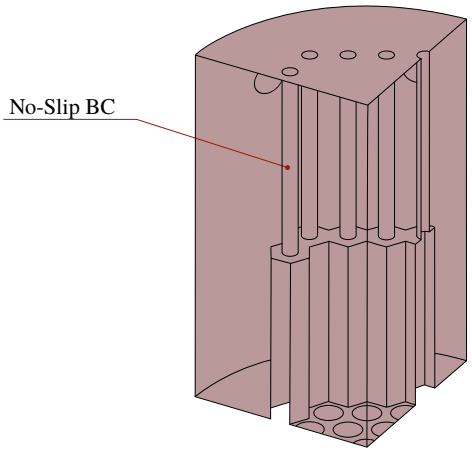

Figure 3.3: Hot Leg region inner walls.

volume. A preliminary hypothesis was that the division made by the hexagonal wrapper extension could lead to flow stagnation and possible thermal stratification in the outside region. Although this behavior was not observed, as presented in this section's partial results, lower average temperatures and velocities were indeed observed.

Initially, the domain was modeled as a full 1/1 core barrel region and then reduced to a 1/4. The viability of using the quarter model with symmetry boundary conditions is shown in Appendix A, where the comparison between a full and a quarter model is presented in more detail.

The choice for the quarter size instead of other fractions (such as 1/2, 1/6 or 1/8), was because the core is hexagonal (not divisible by 8 parts), while there are eight pumps and steam generators (not divisible by 6 parts). Finally, the 1/2 fraction was not chosen because it would lead to a mesh double the size of the 1/4 model but not reduce the simplifications, since it would still need to employ symmetry BCs anyways.

As presented in Fig. 3.4, for a 1/4 model, there are two practical options for dividing the core. With Symmetry Option 1, in pink, the pumps and steam generators would need to be cut in half. With the Symmetry Option 2, in blue, the core would be divided the same way but with a +30° rotation however, with the implementation of rotational

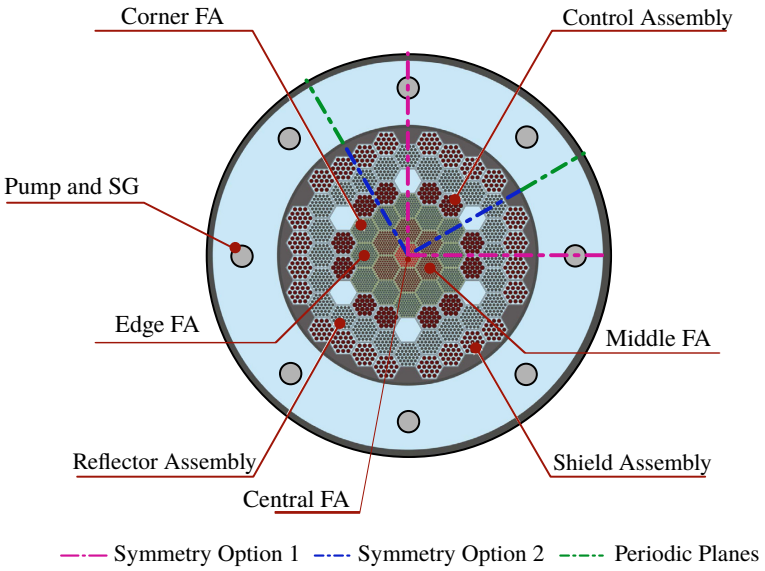

Figure 3.4: Domain division and symmetry planes.

periodic boundary conditions, the pumps and steam generators would not need to be cut. For this reason, the Author chose to use the Symmetry Option 2, in this Chapter, and implement the rotational periodic BC in Chapter 4. Later in Fig. 3.7, it is possible to see the positioning of the inlets of the pump, corresponding with the Symmetry Option chosen.

3.2.2 Porous media and porous jumps modeling

The Porous Media (PM) theory is a useful approach to account for pressure and velocity drops without having to model detailed geometry in a certain fluid flow region. In this Chapter, the methodology related to PM is mainly focused on how it is considered in ANSYS Fluent and how it was implemented for the modeling of the SEALER's FAs.

In ANSYS Fluent, the PM approach employs the Darcy-Forchheimer model for the momentum sink term, [10], presented in Eq. 3.1, where it is used as a negative momentum source (S_m) in the Governing Equation 2.3, for each cell located in the porous region. As the default, the Superficial Velocity Porous Formulation was kept [10].

$$S_{mi} = -\left(\frac{\mu}{\alpha} v_i + C_2 \cdot \frac{1}{2}\rho|v|v_i\right), \; i = x, y, z \tag{3.1}$$

where α^{-1} is the inverse medium permeability (Darcy term) and C_2 is the inertial resistance factor (Forchheimer term), the two main inputs for porous media modeling in Fluent. μ and ρ are the fluid dynamic viscosity and density, respectively. To calculate the porous coefficients, average values for μ and ρ were used.

In Fluent, this momentum source term is applied to every cell within a region

defined as a porous medium for each unit vector direction. Thus, by setting different α^{-1} and C_2 values for each direction, the flow can be oriented.

Table 3.1: Operation Conditions in SEALER's Fuel Assemblies. Adapted from [23].

	Central	**Middle**	**Edge**	**Corner**
Number of FAs	1	6	6	6
Coolant mass flow rate $[kg/s]$	105	88.3	60.2	49.9
Power (P_j) $[MW]$	0.66	0.55	0.37	0.31
Axial Velocity (v_y) $[m/s]$	1.41	1.19	0.81	0.67
Δp_{Bundle} $[kPa]$	125	93	47	34
Δp_{Inlet} $[kPa]$	1.0	33	80	93
Δp_{Outlet} $[kPa]$	0.7	1.0	1.41	1.5

For the fuel assemblies, which all have the same rod bundle geometry, the α and C_2 coefficients were determined using the graphical approach [11], using data from [23] in Tab. 3.1, where the bundle pressure drop can be related to the fluid velocity. The Darcy term and the Forchheimer term were related to the function $\Delta p(v_y)$, which was obtained by fitting a second-degree polynomial function to the data. The function was defined in Eq. 3.2 and plotted in dashed red in Fig. 3.5.

$$\Delta p(v_y) = 16739 \cdot v_y + 51176 \cdot v_y^2 \tag{3.2}$$

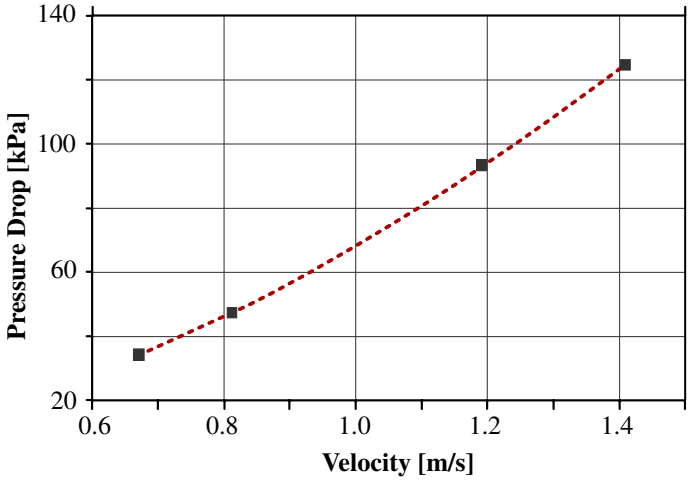

Figure 3.5: $\Delta p(v_y)$ Function Plot.

The Darcy and Forchheimer terms were set equal to the $\Delta p(v_y)$ function, and the resulting equations for α and C_2 were presented in Eq. 3.3 and Eq. 3.4, respectively. The calculated values of α and C_2 were presented in Tab. 3.2, and refer to the preferred flow direction within the fuel assemblies (v_y). The values for the x and z directions were considered 10^3 times larger to avoid cross-flow and to ease the calculation convergence.

$$\frac{\mu}{\alpha} v_y = 16739 \cdot v_y \tag{3.3}$$

$$C_2 \cdot \frac{1}{2} \rho |v| v_y = 51176 \cdot v_y^2 \tag{3.4}$$

Table 3.2: Porous Media Coefficients for the Fuel Rod Bundles.

Coefficient	Value	Unit
α	1.8998×10^{-7}	m^2
α^{-1}	5.2638×10^{6}	m^{-2}
C_2	6.1289	m^{-1}

The inlet and outlet pressure drops were considered through Porous Jumps (PJ) [10], which are simplified one-dimensional porous regions applied to a modified internal surface, earlier indicated in Fig. 3.1. For the implementation of the PJs, each fuel assembly type was assigned its own inertial loss term. Using the same Tab. 3.1, and dismissing the viscous inertial term, due to the predominant dynamic nature of the regions, the inertial loss terms were obtained through the simplified Darcy-Forchheimer model, as seen in Eq. 3.7. A similar approach was used in the work of [81].

$$S = -\left(\frac{\mu}{\alpha} v + C_2 \cdot \frac{1}{2} \rho |v| v \right) = -\frac{\Delta p}{L} \tag{3.5}$$

$$\left(\cancelto{0}{\frac{\mu}{\alpha}} v + C_2 \cdot \frac{1}{2} \rho v^2 \right) = \frac{\Delta p}{L} \tag{3.6}$$

$$C_2 = \frac{2 \Delta p}{\rho v^2 L} \tag{3.7}$$

The values of the Forchheimer coefficients applied to the fuel assemblies inlets and outlets porous jumps are presented in Tab. 3.3. For the inlet PJs, it was used $L = 0.1\ m$ and for the outlet PJs, $L = 0.2\ m$. These length values are derived from the original SEALER design [23].

Table 3.3: Porous Jump Coefficients for the Fuel Assemblies Inlets and Outlets.

	Central	Middle	Edge	Corner
Inlet C_2 $[m^{-1}]$	0.9578	44.3748	232.1863	394.5027
Outlet C_2 $[m^{-1}]$	0.3352	0.6723	2.0316	3.1815

3.2.3 Core axial power distribution functions

Although there are available axial power distribution profiles in [24], obtained by neutronic Monte Carlo simulations, a simpler approach was chosen, using a cosine-shaped distribution of the total power density in each assembly. This approach allows for analytically-defined functions to be applied to the fuel volume regions while still keeping the total power generated within the active regions.

The option of employing a constant-value heat source was considered and evaluated, however, it was not deemed appropriate. In short, this approach results in essentially the same temperature increase but provides a different profile for bulk coolant heating. As the heat source is a constant value applied uniformly along the FA active height, the coolant temperature rises as a constant-slope linear function. This is understandable since coolant temperature rises are derived from the energy transfer rates (i.e.: thermal power), which in turn is the result of the integration of these functions over the FA volumes. The differences in the way the coolant heats are relevant to future analyses, as disparities of as much as 10 K were observed at the same axial position in preliminary analyses. These differences could not be ignored, since for the CHT analyses further in this work, the temperature fields along the core region will most likely have significant influences.

An important observation regarding notation: here the use of q''' $[W/m^3]$ to denote volumetric heat generation rate is not related to the volume of the fuel pellets but to the active FA volume contained within the hexagonal fuel wrapper region (Hex Can). This choice of volume is justified by the use of porous media to model the FA regions, as there are only fluid volumes, and the total power, when multiplied by the active volume, has to be equal to the design references. The volumetric energy generation rate functions have the form of Eq. 3.8, as suggested by many nuclear engineering references, such as [83] and [84]

$$q'''_j(y) = q'''_{max_j} \cdot \cos\left(\frac{\pi(y - H/2)}{H_e}\right) \tag{3.8}$$

where q'''_{max_j} is the maximum volumetric energy generation rate in the j^{th} assembly (central, middle, edge, and corner), defined in Eq. 3.12. The presence of "$-H/2$" is to account for the axial offset to the height zero ($y = 0$ mm) in the FA, which instead of being in the center is at the bottom of the active region. To reach the value of q'''_{max_j} for each j^{th} FA, it is necessary to integrate the $q'''_j(y)$ function over the FA's active height, i.e., from $y = 0$ mm to $y = H = 1100$ mm, as presented below.

$$\frac{\int_0^H q_j'''(y)\ dy}{H} = \frac{\int_0^H q_{max_j}''' \cdot \cos\left(\frac{\pi(y - H/2)}{H_e}\right)\ dy}{H} \tag{3.9}$$

From Eq. 3.9, the average value for the $q_j'''(y)$ function is taken, in order to reach the constants for the P_j over the active volume V_{Active}, which is, in fact, the volume-averaged power in each j^{th} FA. The right-hand side can be integrated by parts, which follows to Eq. 3.11.

$$\frac{P_j}{V_{Active}} \cdot \left[\frac{y}{H}\right]_0^H = \frac{q_{max_j}'''}{H} \int_0^H \cos\left(\frac{\pi(y - H/2)}{H_e}\right)\ dy \tag{3.10}$$

$$\frac{P_j}{V_{Active}} \cdot \cancel{\left[\frac{y}{H}\right]_0^H}^{1} = \frac{q_{max_j}'''}{H} \cdot \frac{2H_e \cdot \sin\left(\frac{\pi H}{2H_e}\right)}{\pi} \tag{3.11}$$

Therefore, the q_{max_j}''' values for each j^{th} FA can be obtained using Eq. 3.12 and are presented in Tab. 3.4.

$$q_{max_j}''' = \frac{P_j}{V_{Active}} \cdot \frac{\pi H}{2H_e \cdot \sin\left(\frac{\pi H}{2H_e}\right)} \tag{3.12}$$

Where H is the fuel assembly active height ($H = 1100\,mm$) and H_e is the extrapolated fuel height, ($H_e = H + \delta = 1300\ mm$), with $\delta = 100\ mm$ as the estimated extrapolation distance [83], and V_{Active} is the hexagonal wrapper inner volume for the active height ($V_{Active} = 0.02439\,m^3$), obtained by hand calculations. P_j is the total power in the j^{th} assembly, as presented in Tab. 3.1. All four volumetric energy generation rate functions from Eq. 3.8 are presented in Fig. 3.6, where the axial position $y = 0\ mm$ refers to the bottom of the active length.

Table 3.4: Maximum volumetric energy generation rate per each FA type

FA	$\mathbf{q_{max}'''}$ **[MW/m³]**
Central	37.0473
Middle	30.8728
Edge	20.7690
Corner	17.4010

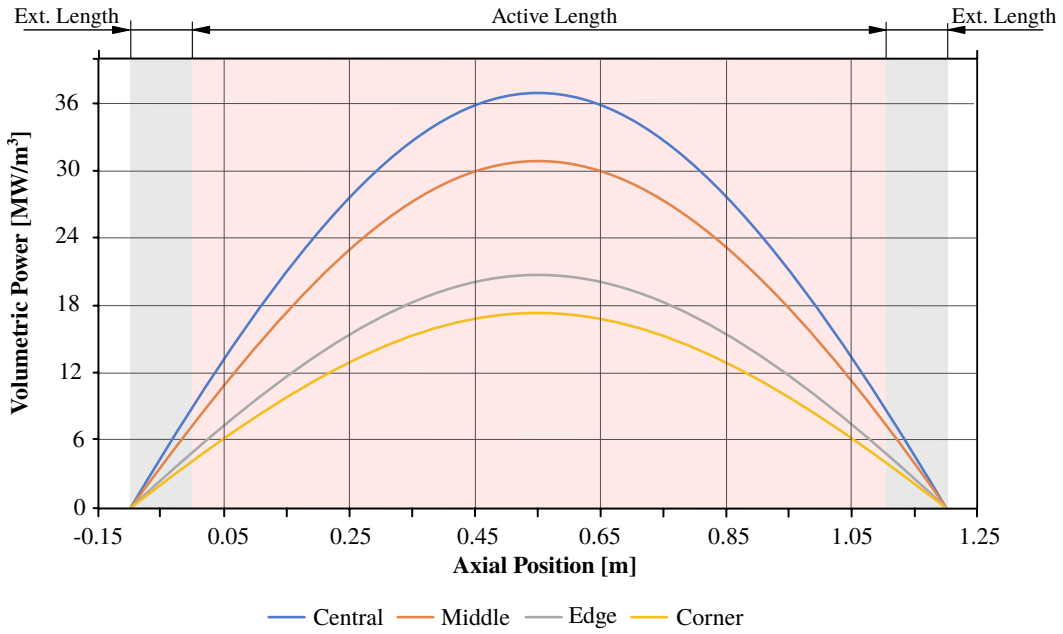

Figure 3.6: Core axial volumetric heat generation rate functions.

3.2.4 Turbulence model selection

The turbulence model selection process in this work was brief. Although it is known that, in a given CFD model, different turbulence models can provide different results in the momentum and energy fields at smaller scales, however, at macroscales, no significant divergence in results should be observable.

For this case, the selection of the turbulence model was restricted to choosing between less expensive approaches that are adequate for bulk fluid flows and that do not require much mesh refinement close to the walls.

As for the least computationally expensive methods, a model with fewer equations to solve should be preferable. Although Spallart-Almaras is the only one-equation option in ANSYS Fluent, it was originally developed for aerodynamic applications and wall-bounded flows [85], and its use for general industrial 3D flows, and also for liquid metals, was not validated. So the two equation options, such as the $\kappa - \omega$ and $\kappa - \epsilon$ models, were next in line to be evaluated. As this case focuses mainly on the far-field bulk flow, employing the $\kappa - \omega$ SST could be an option, since it combines $\kappa - \omega$ (mostly applicable for low-Re and near-wall flows) and $\kappa - \epsilon$, however, in Fluent the Enhanced Wall Treatment function is the approach used in all $\kappa - \omega$ models, which leads to a finer mesh requirement close to the wall ($y^+ < 5$). y^+ is a dimensionless value that represents the distance from the wall to the center of the first layer of volume cells and can be described as $y^+ \equiv \frac{\rho y u_t}{\mu}$, where y is the first cell height, u_t is the shear velocity, ρ and μ are the fluid's density and viscosity respectively.

Since such fine results close to the wall are not of interest in this work, using $\kappa - \omega$ SST would be more expensive and pointless if the $\kappa - \omega$ benefits were not explored. Therefore, the $\kappa - \epsilon$ models were chosen for employing less restrictive wall functions, being preferable for far-field flows, and ultimately consuming less computational resources.

Within the many options of the $\kappa - \epsilon$ model variations, the $\kappa - \epsilon$ Realizable with the standard wall function was chosen, mainly due to its robustness, lower mesh requirements ($y^+ > 30$ close to the walls) [10][11][42] and also because it can predict more accurately the spreading rate of round jets (an applicable case to this work, considering the core's outflow jets), mainly due to its enhanced modeled dissipation when compared to the standard $\kappa - \epsilon$ model. It is also likely to provide superior performance for flows involving rotation, and boundary layers under strong adverse pressure gradients, separation, and recirculation [10].

With a minimum mesh quality requirement set, the mesh generation process can be carried out by sufficing the wall inflation layers first and then proceeding to refine the volume cells in the bulk regions. An interesting alternative for wall function exclusive to ANSYS Fluent is the Enhanced Wall Treatment [10] option; however, it requires a higher resolution near-wall mesh ($y^+ < 5$), which is not aligned with the goal for this section. This option was used by [24] in its SEALER CFD model, which might lead to further research on the applicability of this wall treatment choice.

It is worth noting that both the $\kappa - \omega$ and $\kappa - \epsilon$ models do have wall functions implemented in ANSYS Fluent, meaning that any mesh with $y^+ < 5$ or $y^+ > 30$ could provide good results. However, having the $\kappa - \omega$ or the $\kappa - \omega$ SST demand more computation to solve for slightly better results close to the walls was considered unnecessary.

An important modification applied to the turbulence modeling in this work is on the Turbulent Prandtl (Pr_t). The default value of $Pr_t = 0.85$ is used in most turbulence models, however, as recommended by [51], modifying this model constant to $Pr_t = 2$ brings more accurate results for simulations of low Prandtl number fluids ($Pr \leq 0.01$), such as liquid-metals, as described in more depth in Chapter 2.

3.2.5 Boundary Conditions (BC)

Since in this chapter the $1/4$ model was chosen, the surfaces where the original model was cut had to be modeled as symmetry boundary conditions. Although this choice leads to somehow "easier" solutions when compared to periodic BC, for instance, it is important to note that when using symmetry BC, in the symmetry plane there is zero normal velocity and also zero normal gradients of all variables [10]. Thus, it is not a trivial choice for this

problem because, although the core cut is symmetrical, the cuts around the inlets and outlets are not. For this reason, an analysis was conducted to ensure the appropriateness of this approach. This analysis is presented in Appendix A and demonstrates that, for the aspects relevant to this chapter, the use of symmetry boundary conditions is indeed suitable.

The inlet boundaries were prescribed with a fixed pressure condition set at 513 kPa, as illustrated in Fig. 3.7 (a), while the two outlets were assigned as mass flow rate boundaries, each set to 164 kg/s, which corresponds to the operational capacity of one functioning pump, as outlined in Fig. 3.7 (b) [23]. This specific mass flow rate value was taken from the models developed by [24], and agrees with the total sum in Tab. 3.1, of approximately 162 kg/s for the FAs only, i.e.: the bypass and other flows are conservatively not considered. It should be stated that since lead has a high density, this 2 kg/s difference accounts for a mere 1.9×10^{-4} m^3/s.

It is worth noting that, although defining a fixed mass flow rate for both the inlet and outlet boundaries might seem logical, complications arise due to the temperature-dependent density of lead. Such an approach would pose substantial challenges in satisfying the continuity equation throughout the entire domain, as it would result in a net outflow of fluid exceeding the inflow. Therefore, guided by pressure data from the region [24], a pressure inlet boundary condition was selected and employed to regulate the inlet mass flow rate effectively.

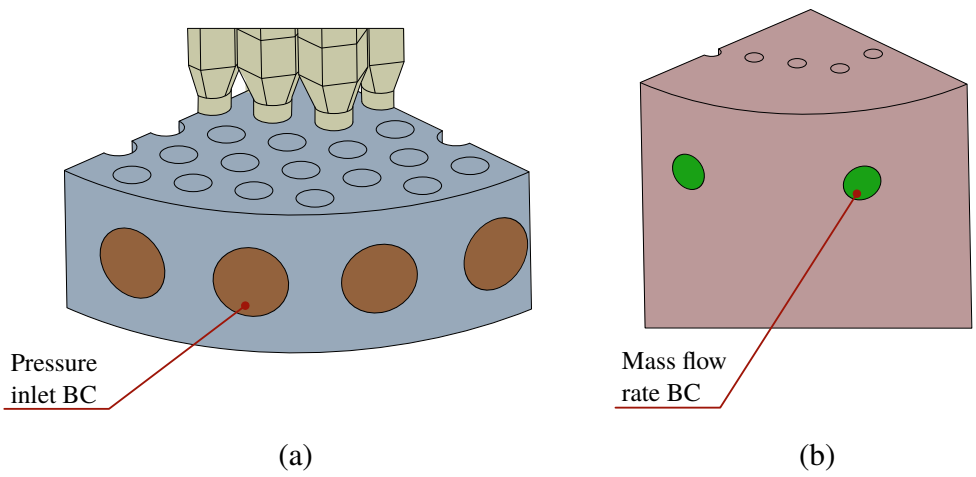

Figure 3.7: Boundary Condition. (a) Inlet BC: Fixed pressure and (b) Outlet BC: Mass flow rate.

The FA's and the core barrel's walls were modeled as adiabatic walls, as the heat transfer to outside media is not yet considered in this chapter.

The upper surface, representative of the lead coolant-free surface height in steady state conditions, was modeled as a slip wall (zero-shear wall stress), in order to avoid using

two-phase modeling approaches. Zero-shear stress wall BCs were also applied to the inner wall of the FAs, since the results for a near-wall velocity field would not be relevant, or make sense, for this case.

3.2.6 Coolant thermal-physical properties

The coolant employed in this analysis was liquid lead, modeled with temperature-dependent properties, as presented in Tab. 3.5. The functions were implemented in ANSYS Fluent via interpreted user-defined functions (UDF) [11], and taken directly from the recommended correlations in [9], except for the specific heat (C_p), which was linearized ($R^2 = 0.9996$) between the temperatures of 620 K and 870 K and directly implemented in ANSYS Fluent's interface.

Table 3.5: Thermal-physical properties of liquid lead. Source: Adapted from [9]

Property	**Temperature-dependent Function**	**Units**
Density (ρ)	$\rho(T) = 11441 - 1.2795 \cdot T$	$[kg/m^3]$
Thermal Conductivity (k)	$k(T) = 9.2 + 0.011 \cdot T$	$[W/m\ K]$
Dynamic Viscosity (μ)	$\mu(T) = 4.55 \times 10^{-3} \cdot e^{1069 \cdot T^{-1}}$	$[Pa\ s]$
Specific Heat (C_p)	$C_p(T) = 159.05 - 0.0185 \cdot T$	$[J/kg\ K]$

3.2.7 Equation solving methods and schemes

Taking advantage of ANSYS Fluent's exclusive capabilities, its Pressure-Velocity Coupled Solver was chosen. As presented in [10] [11], this solver offers a more robust and efficient single-phase implementation for steady-state flows and is recommended for high-density fluids, such as in this case. Also, the pseudo-transient method was used for the steady-state cases, as it helps stabilize the case while providing faster convergence [11] when compared to the segregate alternatives.

Following the methodology used in [82], where a natural convection condition was assessed for a lead-cooled reactor, this work's approach involved the utilization of a steady-state solver. This choice was made to expedite the case solution by establishing stable initial conditions. Subsequently, a full transient solving process was executed, resulting in a reduction in the overall simulation time. To initiate this process, the case was initially run in a steady-state mode, with a minimum requirement of 2000 iterations, ensuring the stabilization of scaled residuals and specific solution monitors, such as average velocity, temperature, and mass flow rate.

The use of a transient solver for steady-state flow is not an uncommon practice when

dealing with high-variable density fluids (such as liquid lead) and when natural convection plays an important role [10]. In this case, given the large volume of fluid subjected to natural convection, numerical instabilities are expected to be observed when trying with a steady-state solver. For instance, this was the case, as the scaled residuals were not enough to assess the case convergence since the continuity equation residuals would not reach 1×10^{-5}. As transient solvers usually have higher relaxation parameters and can account for time, they can capture a true steady flow condition as time allows for the fluid flow fields to stabilize.

For the transient solver, the adaptive time step approach was chosen, while setting the Courant–Friedrichs–Lewy (CFL) number to $CFL = 10$. The usual $CFL = 1.0$ was not employed due to the objective of the transient solving step, which was not to observe fine time-dependent flow behavior but instead, it is to stabilize the solution and allow for a faster convergence. For the mesh size definition study, 10 s of flow were simulated. As presented in the partial results subsection, the 10 s choice was shown enough compared to the 30 s, from which little difference in results was observed. Longer simulation times are up for evaluation in future studies and can present interesting flow behaviors not observed within 30 s.

Tab. 3.6 presents the main solution methods used with the Coupled solver scheme for both steady and transient calculations. Tab. 3.7 presents the relaxation factors used for the steady (pseudo-transient explicit relaxation factors) and transient (explicit relaxation factors for momentum and pressure and under-relaxation factors for the rest) solvers. For both, Fluent's default values were kept.

Table 3.6: Spatial discretization methods used with the Coupled solver scheme.

Spatial Discretization	**Solution Methods**
Gradient	Least Squares Cell Based
Pressure	Second Order
Momentum	Second Order Upwind
Turbulent Kinetic Energy	First Order Upwind
Turbulent Dissipation Rate	First Order Upwind
Energy	Second Order Upwind

Table 3.7: Relaxation factors used in each solver type.

Property	Steady	Transient
Momentum	0.50	0.75
Pressure	0.50	0.75
Density	1.00	1.00
Body Forces	1.00	1.00
Turbulent Kinetic Energy	0.75	0.80
Turbulent Dissipation Rate	0.75	0.80
Turbulent Viscosity	1.00	1.00
Energy	0.75	0.95

3.2.8 Mesh size definition

Once the engineering modeling methods and CFD resolution techniques were established, the first preliminary simulations for this chapter were carried out. These simulations served to define a mesh size that will be used throughout the Dissertation work. It is important to note that the goal of the mesh definition study is not a primary goal but rather a means to make this work more complete. Thus, specific methods for assessing grid convergence, such as the Grid Convergence Index (GCI) Method [86], were not explored in this work. However, a practical example of such a procedure applied to an LBE-cooled sub-channel was carried out by the Author in [87].

The method for defining the mesh size to be used in this and the following chapters is essentially divided into two parts: Near-wall mesh and bulk mesh. The near-wall (NW) mesh definition was limited to the prism inflation layers by testing the number of layers and their first heights. For the bulk mesh, various sizes were compared regarding differences in results for temperature fields, as this will be the most relevant parameter for the CHT analysis in Chapter 5. In this Subsection, the results for the NW simulations are presented as part of this methodology because only the values of the area-weighted average y^+ are evaluated. In the Partial Results Section, a more complete presentation of the results of the bulk mesh analysis is shown.

As presented in the Turbulence Model Selection section, the minimum mesh requirement was set for the NW cells. For this case, the use of prism inflation layers was the approach chosen to quickly satisfy the standard wall function requirement of $30 < y^+ < 300$. For such, a series of 3 meshes were evaluated, all varying the base bulk volume mesh size from 40 mm to 50 mm, and varying the first prism height and prism quantity, as shown in Tab. 3.8. The analysis was performed starting from a coarser NW mesh to a finer one since the y^+ goal was relatively large. For this stage of analysis, only the coupled steady-state

solver was used, since the objective was to obtain a brief comparison of the values of y^+. As presented in the next Subsection, the differences for y^+ values between steady and transient solutions were not significant.

Table 3.8: Evaluated NW meshes details.

	NW mesh 1	**NW mesh 2**	**NW mesh 3**
Surface Mesh (min/max) $[mm]$	20/50	15/40	15/40
Volume Cell Maximum Size $[mm]$	50	40	40
Number of Inflation Layer	4	4	4
Inflation Layer First Height $[mm]$	5	3	1
Number of Volume Cells	160,264	252,819	259,636
Average y^+	88.492	59.904	23.543

After running the preliminary steady-state cases, the prism layer study indicated that 4 layers and a first height of 3 mm were adequate to reach an area-weighted average value of $y^+ > 30$, while NW mesh 3 was too fine, providing $y^+ < 30$, NW mesh 1 was within the $30 < y^+ < 300$ range, and there were regions with y^+ values higher than 150 due to its coarser nature. Thus, the mesh parameters of NW mesh 2 were chosen for the following bulk mesh analysis.

Subsequently, the bulk mesh was selected, using the previously chosen mesh near the wall as the base size. Two coarser meshes and two finer meshes were created, varying only the bulk size. Their sizes are presented in Tab. 3.9 and they vary in relation to the base mesh. For this step, differently from the NW, a transient solving approach had to be implemented. This necessity was noted as values for temperature along the FA were significantly different between the cases solved with steady and transient solvers. The cases were run with the coupled transient solver, for the equivalent of 10 s, with a $CFL = 10$

Table 3.9: Evaluated bulk meshes details.

	Coarse 2	**Coarse 1**	**Base**	**Fine 1**	**Fine 2**
Surface Mesh (min/max) $[mm]$	20/80	20/60	15/40	10/40	10/20
Volume Cell Maximum Size $[mm]$	80	60	40	40	20
Number of Volume Cells	131,231	155,058	252,819	347,431	513,545
Size Comparison with Base	52%	61%	100%	137%	203%
Minimum Orthogonal Quality	0.178	0.140	0.080	0.084	0.121
Average Orthogonal Quality	0.930	0.936	0.950	0.951	0.960
Maximum Aspect Ratio	78.495	53.932	84.622	50.217	68.244

It is worth noting that for the FA volumes and upper wall, a zero-shear stress boundary condition was applied to these walls, implying zero, or close to zero, y^+ values. Thus, only the non-slip walls had their y^+ values assessed. This approach was used to save

computational resources since results near these surfaces do not provide valuable insights. For instance, analyzing a detailed velocity field inside the FA volumes would not mean much, once the whole volume is a simplified geometrical region where porous media is applied.

To allow the visual comparison of the evaluated meshes, Fig. 3.8 presents all 5 meshes side-by-side, on the XY plane. It is possible to notice the size differences mostly in the bulk regions, farther from the walls. Additionally, Fig. 3.9 presents the mesh visual comparison in deeper detail, on other indicated planes.

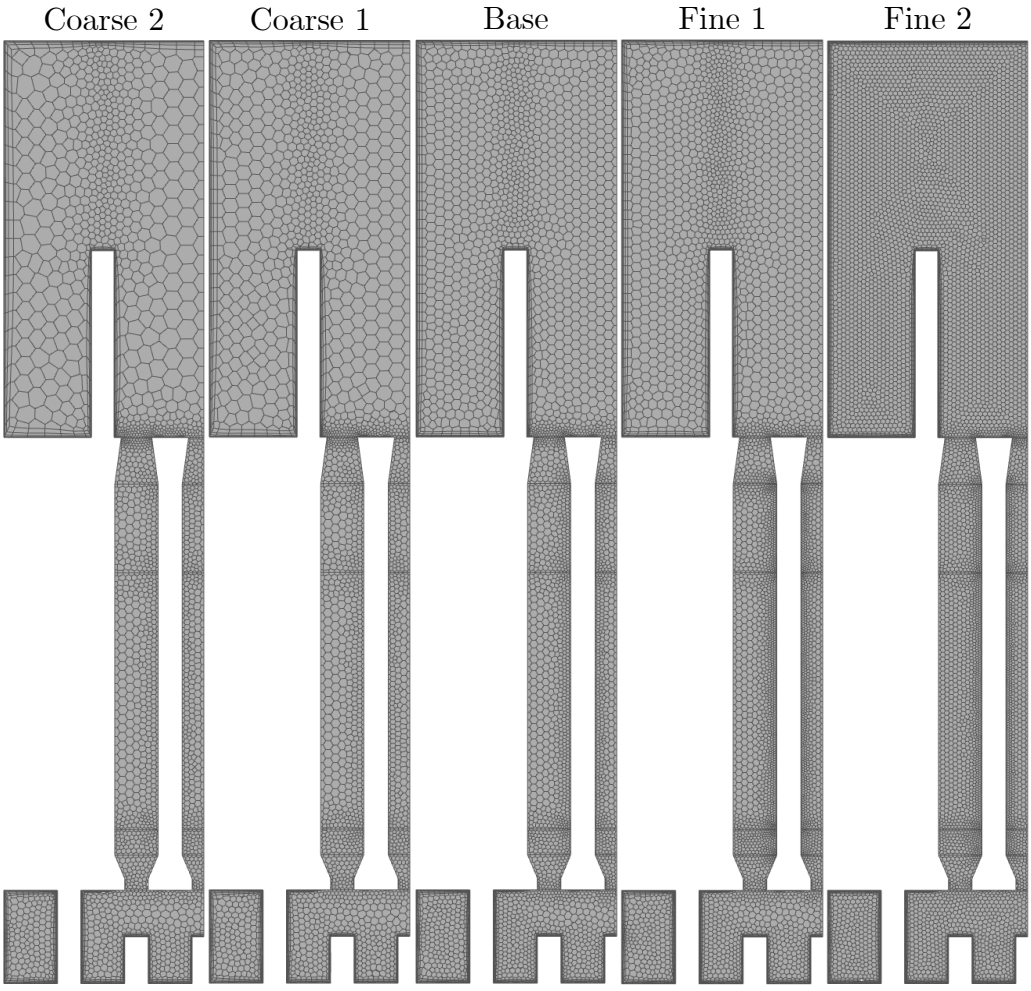

Figure 3.8: Evaluated meshes visual comparison - XY plane.

3.3 Partial Results

This Partial Results Section will be presented in two parts: the bulk mesh definition, after comparing the results obtained by simulating the 5 proposed meshes, and the complete analysis of SEALER's Core Barrel Region with the chosen mesh, in order to evaluate if

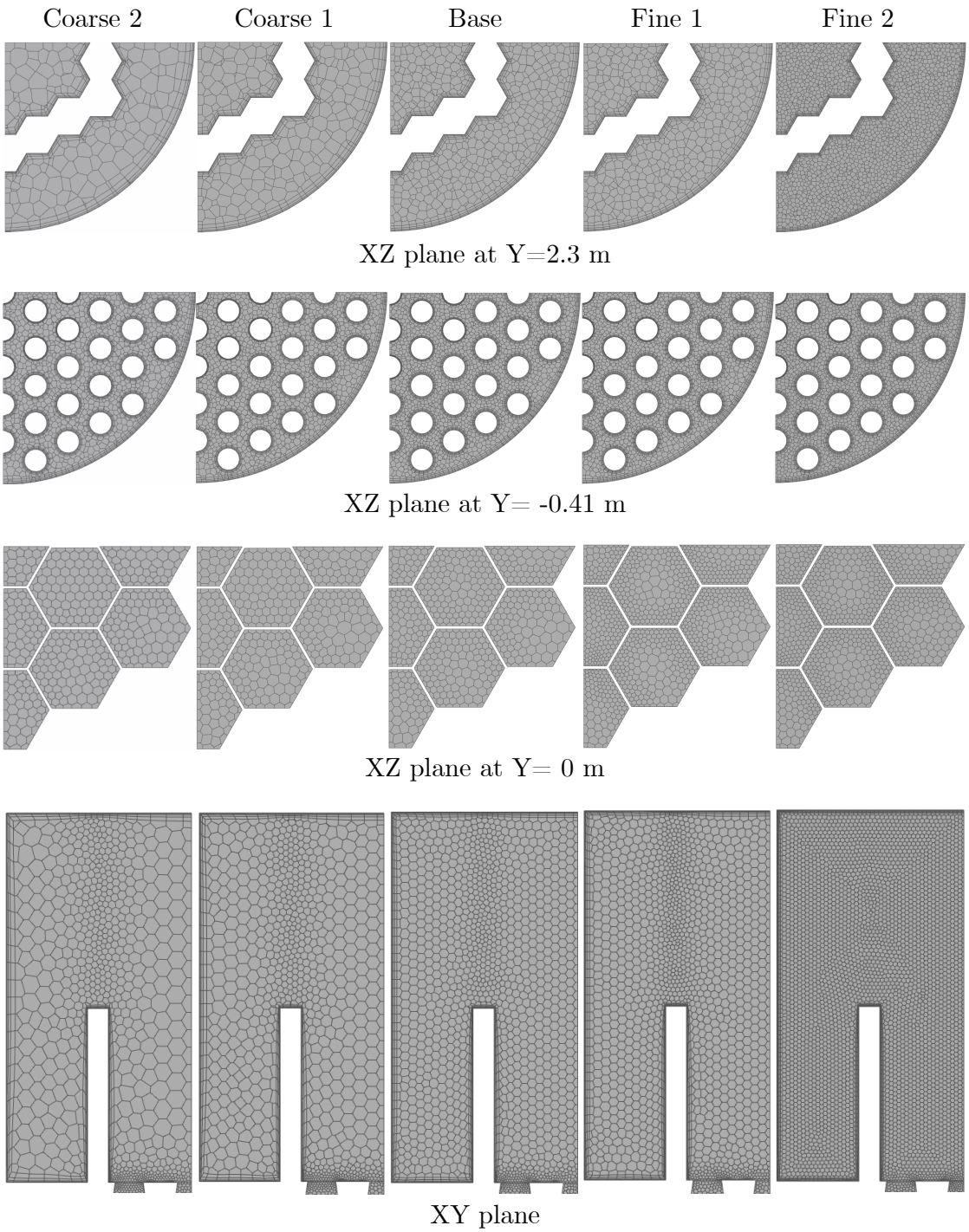

Figure 3.9: Evaluated meshes detailed visual comparison.

the methods used in this model were adequate by comparing their results to the original design proposal from [23].

The results were evaluated on defined planes and lines, whose geometric descriptions are presented in Tab. 3.10, for the planes and in Tab. 3.11, for the lines. It is important to mention that the model origin (0,0,0) is located at the bottom of the Central FA's active region. Also, the coordinate system referenced is the Cartesian default $[\vec{i}\ \vec{j}\ \vec{k}]$.

Table 3.10: Results evaluation planes.

Plane Name	Normal Vector ($\vec{n}$)	Origin [m]
XY	$\vec{n} = \vec{k}$	$(0, 0, 0)$
YZ	$\vec{n} = \vec{i}$	$(0, 0, 0)$
$Y = -0.41\ m$	$\vec{n} = \vec{j}$	$(0, -0.41, 0)$
$Y = 2.3\ m$	$\vec{n} = \vec{j}$	$(0, +2.3, 0)$
$Y = 3.1\ m$	$\vec{n} = \vec{j}$	$(0, +3.1, 0)$

Table 3.11: Results evaluation lines.

Line Name	Line Origin [m]	Line End [m]
$XZ\ Y = 2.3\ m$	$(0, 2.3, 0)$	$(-0.603, 2.3, -0.603)$
$XZ\ Y = 3.1\ m$	$(0, 3.1, 0)$	$(-0.603, 3.1, -0.603)$
Central FA	$(0, -0.4, 0)$	$(0, 2, 0)$
Middle 1 FA	$(0, -0.4, -0.166)$	$(0, 2, -0.166)$
Middle 2 FA	$(-0.143, -0.4, -0.083)$	$(-0.143, 2, -0.083)$
Edge 1 FA	$(-0.143, -0.4, -0.249)$	$(-0.143, 2, -0.249)$
Edge 2 FA	$(-0.287, -0.4, 0)$	$(-0.287, 2, 0)$
Corner 1 FA	$(0, -0.4, -0.332)$	$(0, 2, -0.332)$
Corner 2 FA	$(-0.287, -0.4, -0.166)$	$(-0.287, 2, -0.166)$

Since the result for the NW mesh analysis was already presented in subsection 3.2.8, it will not be necessary to present it here again.

For the bulk mesh size analysis, the cases with all five meshes were run with the steady-state solver (until stabilization) and then with the transient solver for 10 s, as detailed in the subsection 3.2.7. The comparison between the meshes was mainly focused on the temperature fields, since they will be the field of relevance when evaluating the CHT between the regions.

Following the results, Tab. 3.12 presents the volume-averaged temperature in the Hot-Leg region for each mesh size. In this table, it is clear that no significant difference in absolute values is observable. The maximum fluctuation is in the decimal places, but all of them are around the temperature of 703 K. Also in Tab. 3.12, values for area-averaged y^+ on all no-slip walls are presented, in order to show that the bulk mesh size influences y^+, but not greatly. When comparing y^+ values between the NW Mesh 2 and the Base mesh, which are the same, the slight difference can be justified by the use of the transient solver for the Base bulk mesh analysis.

Next, Fig. 3.10 presents the plot for temperature increase along the Central Fuel Assembly region, the hottest channel, for each evaluated mesh. Again, minor differences can be observed, none of which lead to significant divergence around the outlet value of $T \approx 710\ K$. For all meshes, the curve shapes are essentially the same, indicating that, for

Table 3.12: Bulk mesh comparison results

	Coarse 2	Coarse 1	Base	Fine 1	Fine 2
Hot Leg Average Temperature [K]	703.314	703.294	703.163	703.339	703.314
Walls Average y^+	56.079	54.924	60.551	64.674	64.9615

the methods employed for the momentum sink and heat source in the region, the evaluated meshes are mostly converged.

Fig. 3.11 shows in bar graphs the absolute differences between the average temperatures from Fig. 3.10 for each consecutive mesh. It is worth noting that the maximum differences barely surpass 0.1 K, indicating that all five meshes can be considered converged for the FA regions when considering the employed models.

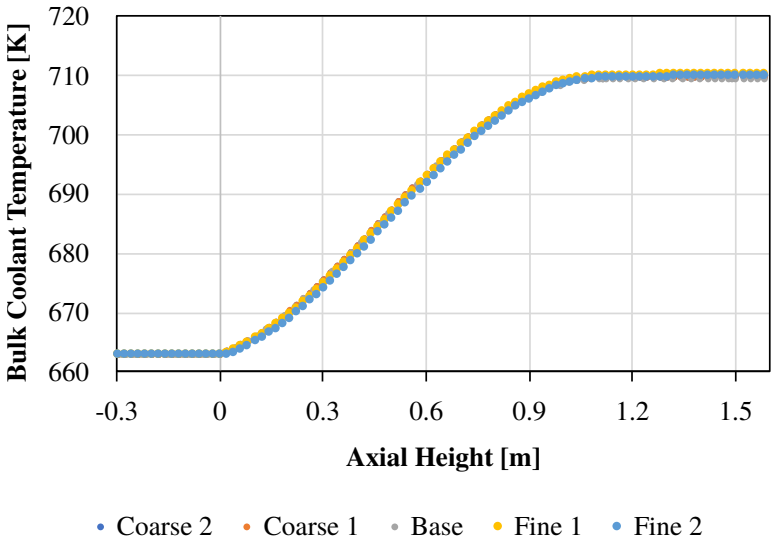

Figure 3.10: Coolant bulk temperature along the Central FA - Comparison between evaluated meshes.

Fig. 3.12 presents the planes and lines of interest in the Hot Pool region. It is worth noting that as the Lines $XZ\ Y = 2.3\ m$ and $XZ\ Y = 3.1\ m$ cross solid regions, their result plots have gaps. Fig. 3.13 presents the temperature plots along the Line $XZ\ Y = 2.3\ m$. In this figure, shape differences are more noticeable, especially in the region closer to the core outlet streams (between $-0.4\ m$ and $0\ m$). The same behavior can be observed in Fig. 3.14, which plots the velocity magnitude along the Line $XZ\ Y = 3.1\ m$. As this line is at a higher elevation, the core outlet jets can become more mixed, reducing the differences in relation to the coarser meshes. A more visual result is presented in Fig. 3.15, where the contours for velocity magnitude are presented on the XY plane. In this figure, the outflow jets from the core are clearly more separated in the Fine 2 mesh than in the Coarse 2 mesh.

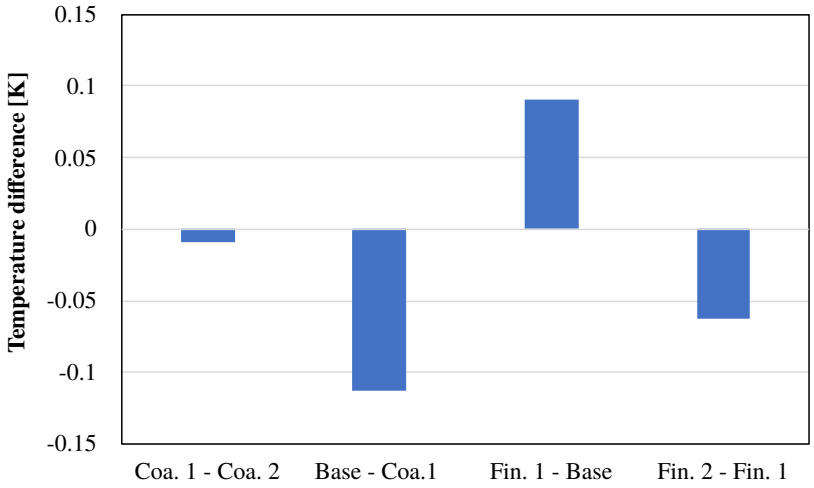

Figure 3.11: Absolute differences in average temperature values between the evaluated meshes.

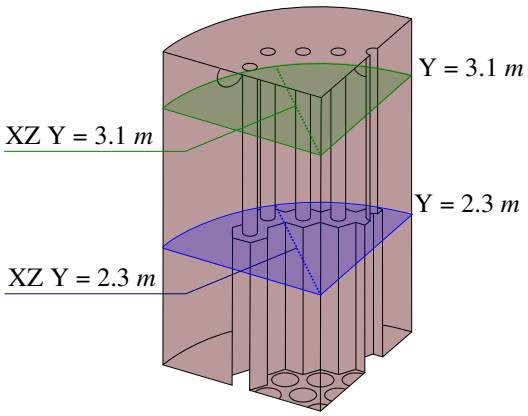

Figure 3.12: Lines and planes in the Hot Pool region.

Although this detailing is indeed an interesting advantage to understanding the flow behavior, it does not impact the average temperature in the Hot-Leg volume. The coarser meshes' behaviors can be understood as the averaged result given by the finer meshes, which can capture the fields with higher resolution, but do not contribute to the analyses. This same behavior is observable in the velocity contours.

As analyzed in this subsection, it becomes clear that all five meshes provide close results for the same problem. Although finer meshes do offer finer results for the flow field contours, the averaged values for temperature do not seem to be affected by mesh resolution. This statement leads to the partial conclusion that, for the sake of efficiency and computational resource economy, the Coarse 2 mesh, with 131 231 volume cells, should be defined as the standard mesh size to be employed in future chapters' models.

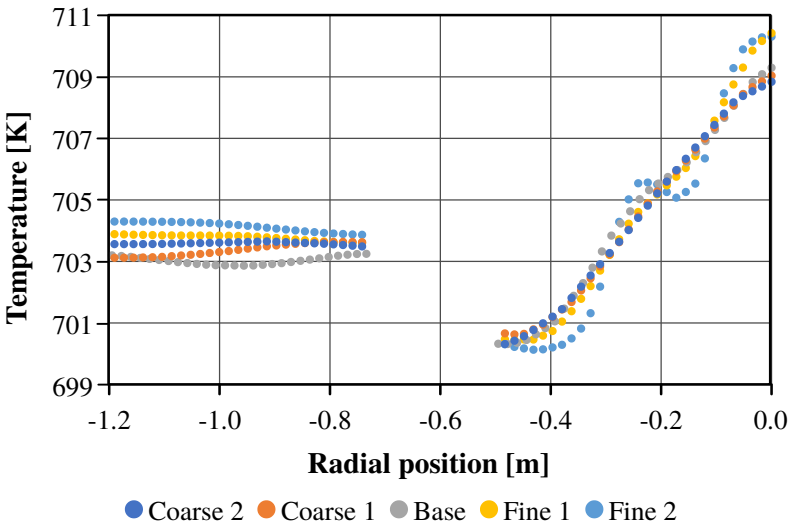

Figure 3.13: Temperature at XZ line $Y = 2.3$ m.

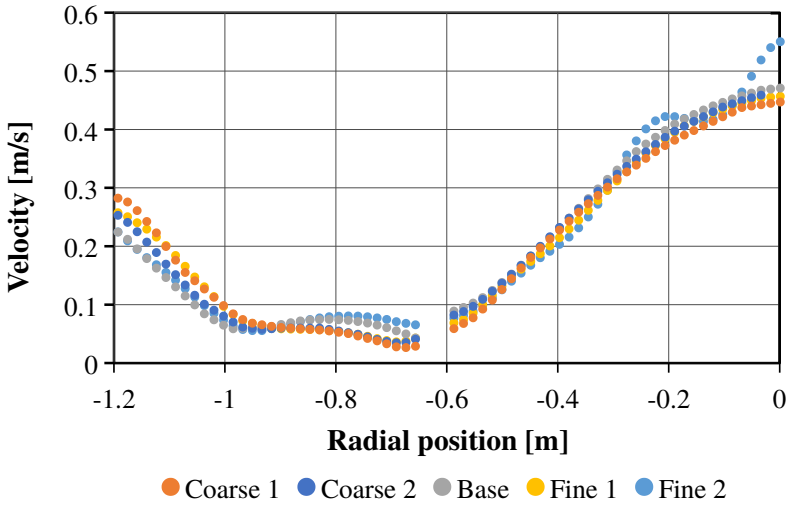

Figure 3.14: Velocity magnitude at XZ line $Y = 3.1$ m.

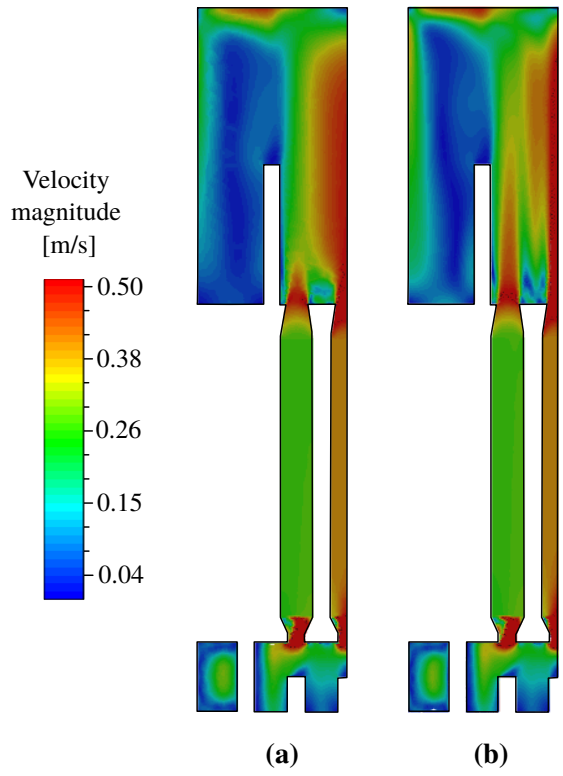

Figure 3.15: Velocity magnitude contour comparison between (a) Coarse 2 and (b) Fine 2 meshes.

3.3.1 SEALER's Core Barrel region steady-state solution

Once the mesh size was defined, more results could be presented regarding the modeling strategies employed, i.e.: porous media, porous jumps, and the FA heat generation functions. Although the same results are available for all the other meshes, these will not be presented in this subsection, as they are similar enough. The following results for the Middle, Edge, and Corner FAs, whose center lines are presented in Fig. 3.16, are taken as the simple average results from their respective 1 and 2 assemblies. This is to simplify the analysis since FA 1 or 2 in each case are very similar.

The plots for temperature increase along the different FAs center lines can be seen in Fig. 3.17, where all the FAs present the same shape for the temperature curves, differing in their slope and maximum values. As defined in Eq. 3.8, the coolant starts heating at $Y = 0\ m$, up to $Y = 1.1\ m$, which are the active region limits. From $Y = 1.8\ m$, where the FAs end, the temperature curves start converging to the average Hot Leg temperature of around 703 K, so the Central and Middle FAs start decreasing while Edge and Corner FAs start increasing slightly. Hereinafter the values along the FAs center lines will be referred to as 'bulk', as they are representative enough, and serve as a term simplification for the following chapters.

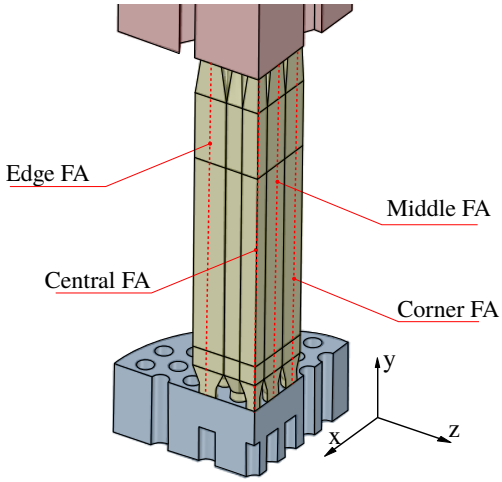

Figure 3.16: Lines for result analysis in the different FAs.

The results that can be most exclusively linked to the porous media and porous jump methodologies are the hydraulic values extracted from the FA volumes, such as pressure drop and velocity. Figs. 3.18 and 3.19 present the plots for static pressure and velocity magnitude, respectively, along the Central, Middle, Edge, and Corner FAs. The inlet porous jumps are located at $Y = -0.11\ m$ and the outlet porous jump at $Y = 1.68\ m$. At these positions, in both the pressure and velocity plots, drops can be observed, all

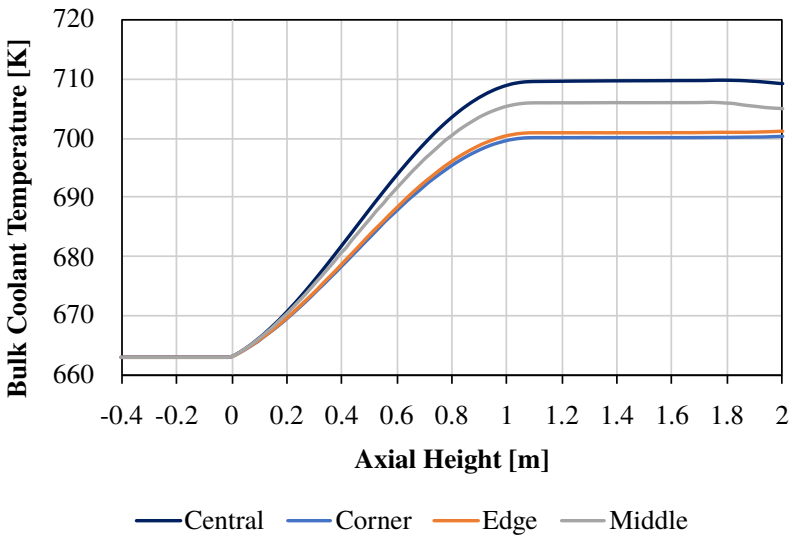

Figure 3.17: Temperature along FA types.

proportional to the coefficients defined in Tab. 3.3. Also, it is possible to identify the use of porous jumps as an effective method to account for localized pressure drops (such is the case for the inlets and outlets orifices), instead of using Porous Media applied to a small volume. For the Porous Media, which were implemented using the same coefficients for all FAs (since the fuel bundle arrangement is indeed the same for all FAs), their influence on the pressure and velocity drops along the FAs' heights can be identified by the constant slopes (for pressure) and constant values (for velocity) between $Y = 0.0\ m$ and $Y = 1.11\ m$.

For the heights within $-0.26\ m < Y < -0.11\ m$ and $1.48\ m < Y < 1.68\ m$, where no porous approach was employed, the steeper variations in pressure and velocity come mostly from the funneling geometry of the transition from cylindrical foot to hexagonal wrapper, converging or diverging. The contours for temperature are shown in Fig. 3.20 while the contours for velocity magnitude are shown in 3.20.

In Fig. 3.20 (a), the temperature contours for the Planes XY and YZ are displayed, indicating that the coolant is uniformly heated among the various FA types. Despite different heat generation functions, temperature regulation is achieved through coolant flow control. This suggests that the coefficient values for porous jumps and media are appropriate, as these momentum sink approaches provide a good balance for coolant flow velocity and temperature. Fig. 3.20 (b) and 3.20 (c) presents the temperature contours on the transversal XZ planes at $Y = 3.1\ m$ and $Y = 2.3\ m$ respectively. Although higher temperatures are observed closer to the core center line, the overall temperature distribution is homogeneous, close to the average 703 K in the region. No temperature stratification was observed for the 10 s of simulation time.

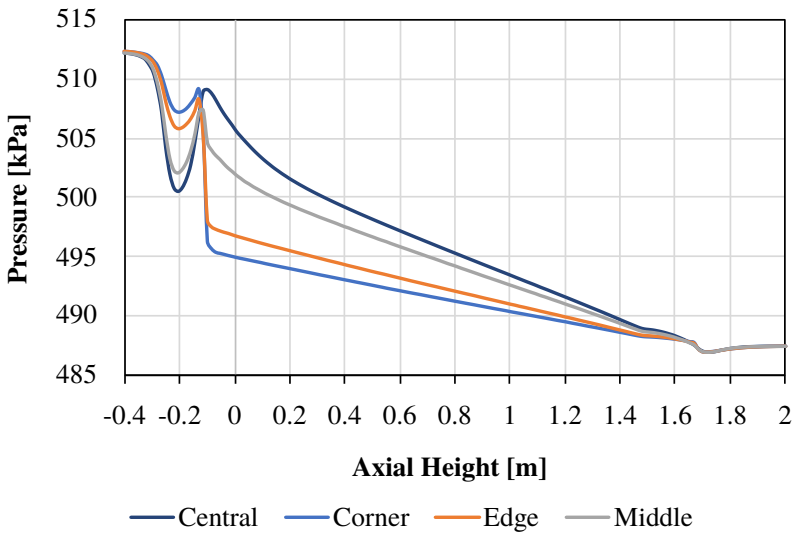

Figure 3.18: Pressure along FA types.

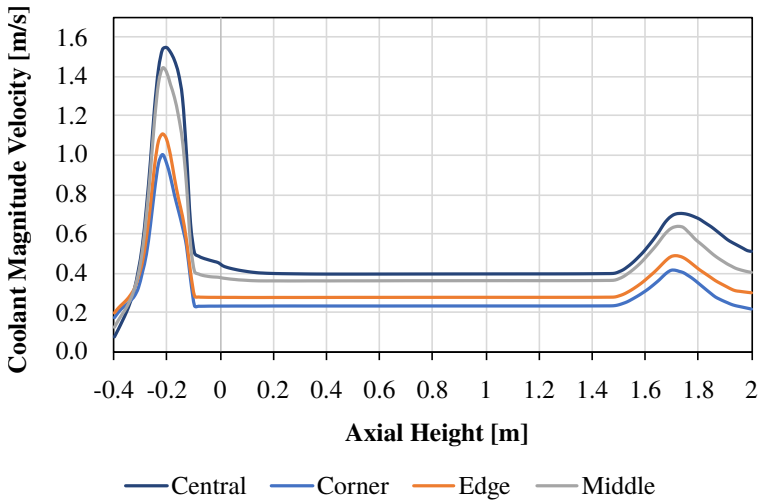

Figure 3.19: Velocity magnitude along FA types.

Moreover, the results presented in Tab. 3.12 and Fig. 3.17 indicate that the average temperature rise in the core is approximately 40 K, which is in close agreement with the proposed value of 42 K in the original design reference by [23]. However, the minor difference of 2 K may be attributed to simplifications and assumptions made in this model.

For the velocity magnitude contours, Fig. 3.21 (a) presents the results for the longitudinal planes, where the highest velocities are observed in the center of the Hot Leg volume as a result of the core's outlet jet streams. In the FAs, lower velocities in the Corner FAs can be attributed to the greater constrictions imposed by the inlet porous jumps. One relevant point is the difference between the inner and outer regions in the Hot Leg, divided by the Control Assemblies' hexagonal extensions. As supposed in this Chapter's methodology section, this physical division resulted in lower velocities in the

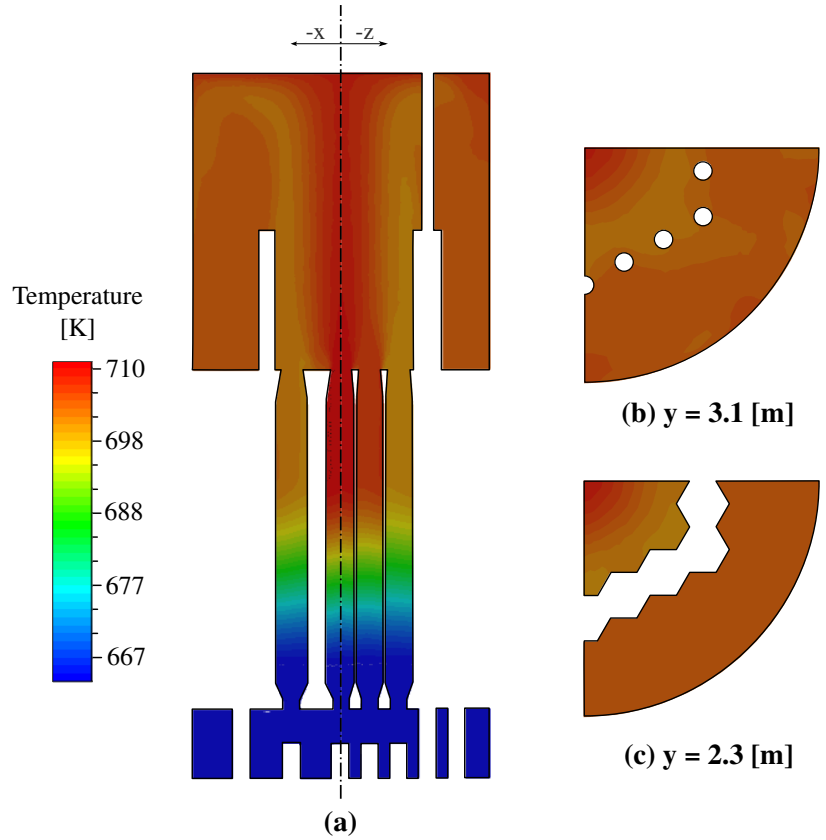

Figure 3.20: Temperature contours: (a) Longitudinal YZ and XY planes, (b) transversal XZ plane at $Y = 3.1\ m$ (c) and $Y = 2.3\ m$.

outer region, especially closer to the bottom. However, the temperature contours indicated that, although there is a velocity gradient in the region, it does not lead to thermal stratification.

Fig. 3.21 (b), 3.21 (c) and 3.21 (d) display the contours for velocity magnitude on the transversal planes, where the same higher velocities are observed close to the core center line. On plane $XZ\ Y = -0.41\ m$ the influence of the FA feet (cylinders) is noticeable, since its distribution acts as a tube bank, slowing the incoming coolant flow, and homogenizing the velocity field closer to the FA inlets.

3.4 Partial Conclusions

In this chapter, the Core Barrel Region of the SEALER reactor was simulated in a steady-state condition, employing various CFD methodologies. The goal was to model the region in a computationally efficient manner while accurately representing the reactor's core barrel region behavior as designed, which was reached in this partial chapter.

The methods used to define an adequate mesh size will be helpful for future chapters, as they provide a basis for determining the appropriate mesh size without the need for

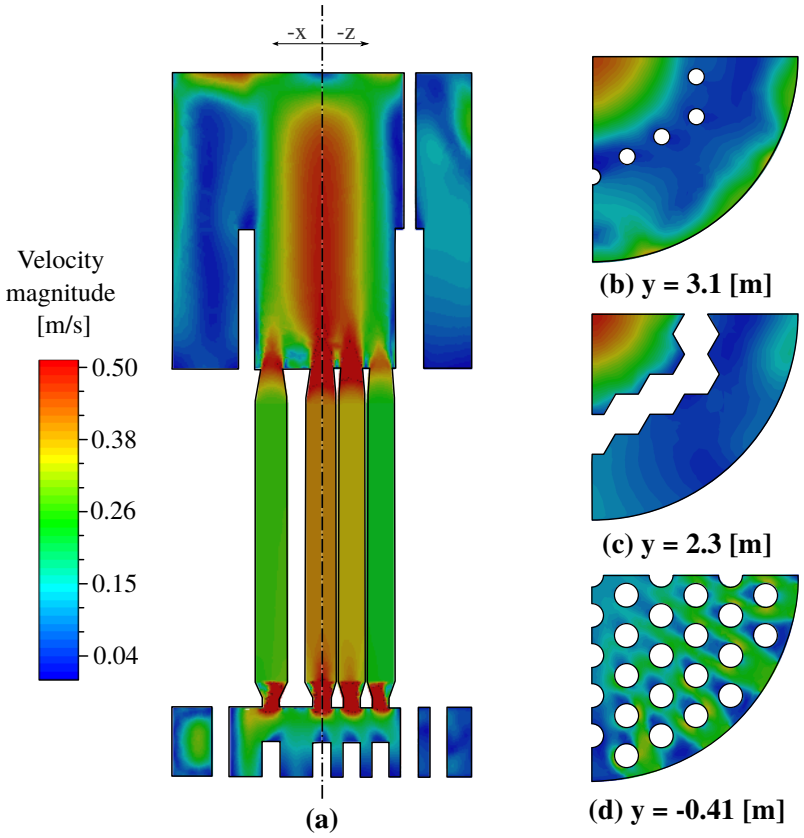

Figure 3.21: Velocity magnitude contours: (a) Longitudinal YZ and XY planes, (b) transversal XZ plane at $Y = 3.1\ m$, (c) $Y = 2.3\ m$, and (d) $Y = -0.41\ m$.

additional tests.

The results for the FA hydraulic modeling strategies are particularly relevant, as they demonstrate the effectiveness of porous approaches in simulating coolant flow control despite being mathematical simplifications of complex geometry-dependent flows. This control is critical in ensuring that the temperature rise is homogeneous among the different FAs, given their individual heat generation rate functions. Through a combination of these methods, a temperature increase close to the design value was achieved, which is essential for future CHT analyses, as are the velocity and temperature field distributions obtained as the major results.

Chapter 4

SEALER Full Loop - Primary Circuit Analysis

4.1 Motivation and objectives

In this Chapter, the whole SEALER reactor is simulated under a steady-state operation condition. By expanding the domain, aside from the additional volume, the pumps and Steam Generators (SGs) are included, and their modeling strategies are presented. Also, Periodic Boundary Conditions (PBC) are implemented to account for the rotational periodicity brought by the domain reduction, parallel to the use of Symmetry BC in the Core Barrel Region.

The main motivation of this chapter is to complement the previous chapter's results and to demonstrate that the whole SEALER full primary system can be modeled using the methods chosen. Special focus is given to the modeling schemes used in the SGs, namely the temperature-dependent heat sink function and the porous media applied to these volumes, for which two methodologies were implemented and compared.

The partial results focus on comparing the two models developed, which differ in the SGs porous media setting, and indicate that the methods employed (for both settings) and the solving schemes were adequate to simulate the full SEALER's primary circuit in a steady-state condition.

4.2 Methodology

This chapter's methodology section encompasses three main engineering modeling methods: Recirculating Boundary Condition (RBC) to model the pumps in steady-state,

two different porous medium models, and a temperature-dependent heat sink function for the SGs.

For the setting of the porous media in the SGs, two main methods were found to be dedicated to transversal flow across staggered tube bundles. Their comparison is presented in the Partial Results Section.

Nonetheless, the extended domain was first simulated without thermal power (nor sinks) to verify whether the hydraulics were working adequately. The main effort in this first simulation step was to implement the Periodic Boundary Condition to the Hot Pool and Cold Leg's cut planes. Once the hydraulics were proven to work well with the PBC, the thermal contributions were evaluated, especially to calibrate the heat-sink function.

It is worth mentioning that the numerical and solving schemes were not changed from the ones presented in the previous chapter. Therefore, all the simulations were run with the same parameters described before.

4.2.1 Geometry description and assumptions

Similar to the previous Chapter, the main geometry features were modeled based on the available data from SEALER's original references, which include the reactor vessel diameter and thickness, SGs basic dimensions, and relative heights between components. Fig. 4.1 presents the extended CAD model used in this Chapter.

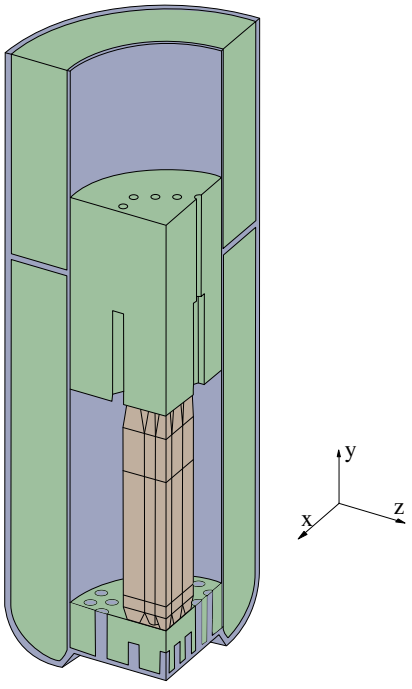

Figure 4.1: The SEALER Full Reactor CAD model.

In this Chapter, the solid regions such as the Core Barrel and the Reactor Vessel

were modeled as solid stainless steel. Although these solid regions were modeled and meshed, their walls in contact with liquid lead were kept adiabatic. This choice was to segregate the evaluation of methods from the evaluation of the CHT, which was left for the next Chapter.

Some simplifications were introduced, particularly concerning the pumps, for two primary reasons: Firstly, detailed dimensions for this component were unavailable, and secondly, since no assessments were intended within this volume, there was no need to model the complex pump geometry. Instead, they were represented as extended elbow piping, redirecting fluid from the Hot Leg in the Core Barrel Region to the Hot Pool. The pump design is presented in Fig. 4.2, and it's worth noting that a similar approach was also employed by [78] [79].

By substituting a complex volute geometry with the simplified elbow, the CAD design and meshing procedures became more straightforward. However, it is essential to acknowledge that there is an angular offset compared to the original design, resulting in the pump outlet being radially aligned with its inlet. To accommodate this offset, the SGs also had to be adjusted, positioning their centers beneath the pump outlet. As indicated in the partial results section, the coolant tends to homogenize as it descends from the SGs before re-entering the Core Barrel. Consequently, no adverse effects were observed due to the implementation of this simplification.

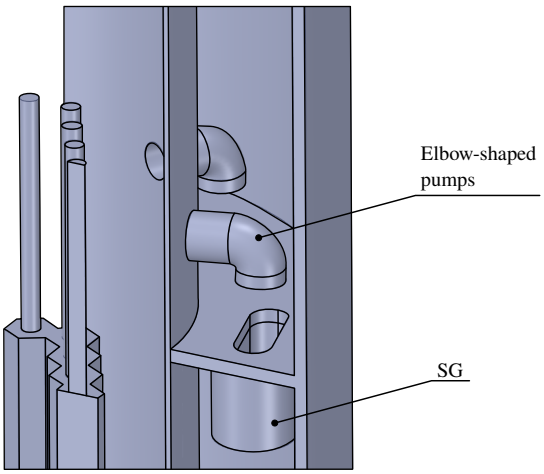

Figure 4.2: Elbow-shaped Pumps.

The SGs were also modeled with two simplifications: I) Due to the use of a porous medium, the tube bundles were not modeled into the geometry, leaving the inner volume as a continuous fluid region. II) The SGs were designed as simple extended circles, instead of the original bean shape [23], since no detailed dimensions were available, and no major impact was expected to result from this. Fig. 4.3 presents the SG CAD model section.

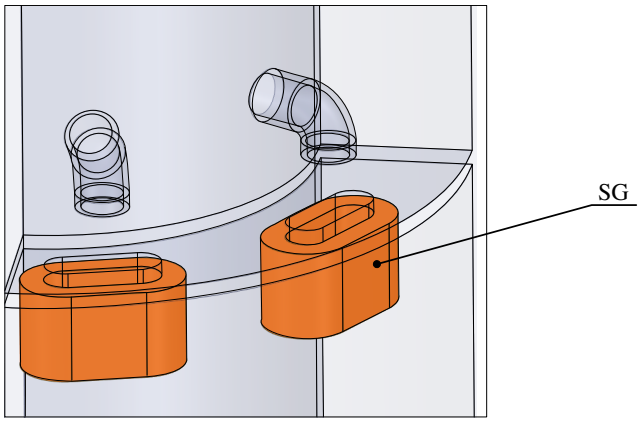

Figure 4.3: Steam Generators (SGs).

4.2.2 Rotational Periodic Boundary Condition

As briefly mentioned in this section's introduction, Rotational Periodic Boundary Conditions were applied to the cut planes in the Hot Pool and Cold Leg regions. Differently from the Core Barrel, which used Symmetry BC, these two volumes are farther from being symmetrical, given the pumps' and SGs' positions, which are not equally distanced from both surfaces. In Fluent, the flow at a PBC is treated as if the opposing periodic pair plane is in direct contact with its cells, giving it periodic continuity [10].

Fig. 4.4 presents visually the two Rotational Periodic BC interfaces, which are periodic in an angle of $\pi/2$ rad. To implement this BC in Fluent, it was necessary to combine the two interfaces on each side, so there would be only one pair. To implement this BC, the pairs had to be set starting from the meshing stages. That is because the interfaces can only be associated with one another when they have the same mesh layout.

4.2.3 Pumps - Recirculating Boundary Condition

A simple approach was employed for the pumps, given the steady condition. Instead of a fixed-value momentum source, or a traditional head $\times$ flow rate curve, the Recirculating Boundary Condition (RBC) was used.

This interface BC is non default ANSYS Fluent feature, in which the user can set an outlet with a constant mass flow rate and its paired inlet. Between the two, an increase in temperature or a heat source can be implemented, making this BC useful for heating and cooling systems with known temperature variations. However, for this application, the RBC was solely employed for its constant mass flow rate ($\dot{m} = 164\ kg/s$ for each), without varying temperature values.

This approach was found to be the simplest way to represent the momentum

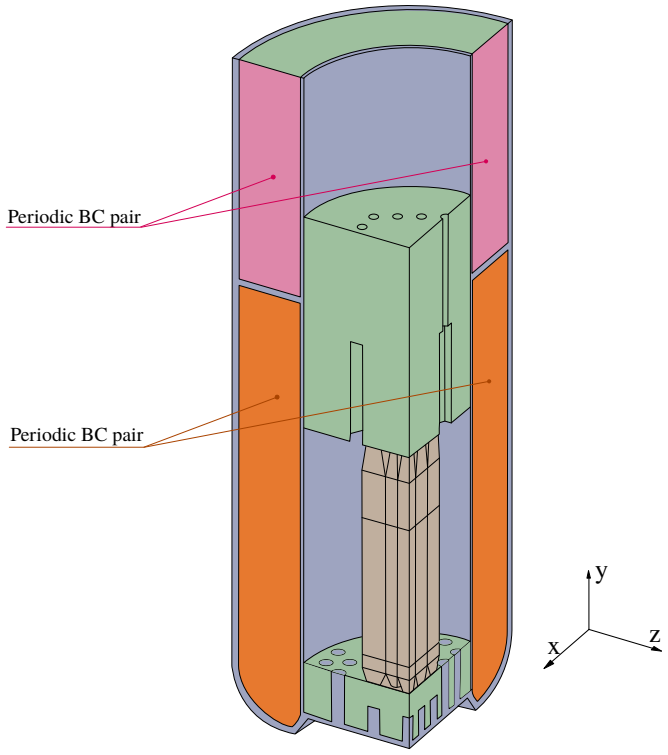

Figure 4.4: Periodic Boundary Condition (PBC) plane pairs.

increase given by a pump working in steady conditions. Thus, instead of trying to adjust the right value of a volumetric momentum source, the RBC option allows for the right coolant mass flow rate. To enable this BC option, the user can input the following command into Fluent's TUI (Text User Interface):

Listing 4.1: Text User Interface - Pump recirculation boundary condition

```
(rpsetvar icepak #t)
(models-changed)
```

As mentioned in the geometry modeling of the pumps, the elbow simplified design used by [78] [79] was also implemented in this work. Due to the RBC interface nature, two surfaces have to be paired (one for the outlet, another for the inlet), however, they must not be connected by volume cells, as the flow between them is already imposed, and not solved. To satisfy this condition, a cylindrical region was reserved for the pumps, as highlighted in Fig. 4.5, with their upper and lower circle faces defined as the outlet and inlet interfaces, respectively. Finally, to physically disconnect them, the cylindrical volumes were simply suppressed from the mesh, and the RBC was successfully implemented.

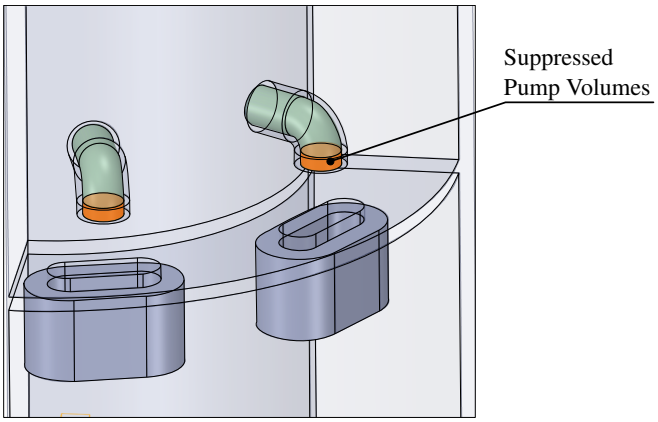

Figure 4.5: Suppressed Pump Volumes.

4.2.4 Steam Generators Porous Media

For the SGs porous media (PM), the Darcy (viscous) term from the Darcy-Forchheimer Equation (3.1) was suppressed, given the high velocities and turbulence in the SGs regions, placed right under the pumps. Eq. 4.1 presents the equation used to find the C_2 value employed in the SG PM, where ρ is the average fluid density (considered at 683 K), w is the average fluid velocity in the SG region and L is the SG region's real thickness.

$$C_2 = \frac{2\Delta p}{\rho w^2 L} \tag{4.1}$$

The main focus of this subsection is on the methods used to find the pressure drop through the SGs tube banks, Δp. Upon consulting references for pressure drop across tube bundles, two main methodologies were found and considered for comparison: 1) The Handbook of Hydraulic Resistances by Idelchik, 2008 [88], and 2) Heat Transfer from Tubes in Crossflow by Žukauskas, 1972 [89], which is commonly referenced by traditional references, such as Kazimi & Todreas [83], and Incropera & DeWitt [90].

Both methods were used to find Δp (and consequently C_2 through Eq. 4.1) with the available data for the SGs tube banks [23], and their calculation steps are presented as follows:

Idelchik approach for Δp

In the methods compiled by Idelchik, the final objective is to find the friction factor ζ, which relates to Δp by Eq. 4.2:

$$\Delta p = \zeta \rho \frac{w^2}{2} \tag{4.2}$$

Although there are many equations for ζ, each is only applicable for certain ranges of bundle geometry, which makes identifying geometric parameters the first step in this method. For instance, SEALER's SG was identified as being a "staggered smooth-wall bundle of tubes", with its relevant dimensions listed in Tab. 4.1. Fig. 4.6 presents the cross-section of the tubes and the relevant dimensions.

Table 4.1: Main SG tubes bundle dimensions.

Bundle Dimension	Value [mm]
s_1	40.70
s_2'	23.5
d	20
$\bar{s}$	5.9143
s_1/d	2.035
s_2'/d	1.175

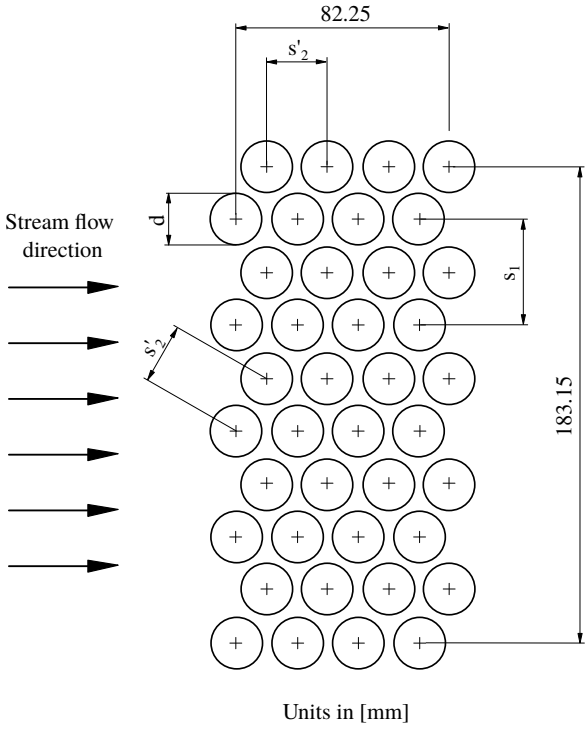

Figure 4.6: Tube Bundle Cross-section.

Given dimensions and values for s_1, s_2', d and $\bar{s} = (s_1 - d)/(s_2' - d)$ presented above, Eq. 4.3 could be selected for determining ζ, given the conditions of $1.44 \leq s_1/d_{out} \leq 3.0$ and $1.7 \leq \bar{s} \leq 6.5$

$$\zeta = 0.44(\bar{s}+1)^2 Re_m^{-0.27}(N+1) \tag{4.3}$$

Where N is the number of tube rows, $Re_m = w_{0m} \cdot (d/\nu)$ is the reference Reynolds Number, $w_{0m} = w_{in} \cdot (T_m/T_{in})$ is the reference velocity, w_{in} is the inlet velocity to the SG region, $T_m = (T_{in} + T_{ex})/2$ is the reference average temperature. All their values are presented in Tab. 4.2.

One important notice to make is that this method (and also the following) considers a simple 2-dimensional problem, where the inlet velocity (w_{in}) is usually a fixed input. However, for the simulated SG extended-circle geometry, a set of considerations were made to define the inlet velocity, as follows:

1. The SG inner internal surface was taken as a reference ($A_{SG} = 0.282\ m^2$). Its area was obtained from the CAD model, and considered as a planar projection;

2. The tube bundles' projected area was calculated ($A_{Bundle} = 0.094\ m^2$) and subtracted from the projected reference area, resulting in the effective flow area ($A_{Eff} = A_{SG} - A_{Bundle} = 0.188\ m^2$);

3. The total mass flow rate of $\dot{m} = 164\ kg/s$ (equivalent to one pump) was considered as passing through the reference surface;

4. The inlet velocity was obtained by the standard relation between mass flow rate, flow area, and fluid density (considered at the Hot Leg average $T = 703\ K$). Thus, $w_{in} = \frac{\dot{m}}{A_{eff} \cdot \rho} = 0.828\ m/s$.

Table 4.2: Input parameters for Idelchik [88] hydraulic resistance model.

Input Parameter	Value	Units
Re_m	781.3301	-
w_{0m}	0.0805	m/s
w_{in}	0.0828	m/s
T_{in}	703	K
T_{ex}	663	K
T_m	683	K

Finally, with Re_m and w_{0m} calculated, ζ can be obtained from Eq. 4.3:

$$\zeta = 0.44 \cdot (6.9143)^2 \cdot (781.3301)^{-0.27} \cdot 9 = 31.3418 \tag{4.4}$$

Also, Idelchik [88] points out that for situations when heat transfer is involved, the values of ζ in Eq. 4.3 should be supplemented with the term $\Delta\zeta$ given by Eq. 4.5, which

accounts for density variations within the medium, and its consequences on acceleration pressure drop.

$$\Delta\zeta = 2 \cdot \left(\frac{T_{ex} - T_{in}}{T_m} \right) = 0.1171 \tag{4.5}$$

In this way, $\zeta_{total} = \zeta + \Delta\zeta = 31.2247$ could be reached and used in Eq. 4.2, providing $\Delta p = 1068.1175\ Pa$.

Ultimately, with Eq. 4.1 the $C_2 = 390.3089\ m^{-1}$ coefficient value could be determined and implemented to the first SGs porous media model.

Žukauskas approach for Δp

In Žukauskas' article [89], the proposed path to determine the hydraulic resistance of a tube bank is presented in a graphical approach (Fig. 4.7), where the geometry and flow parameters can be used to easily find the friction coefficient (ξ) and correction factor (χ). The Δp obtained with this method is analogous to the previous one, presented in Eq. 4.6 below:

$$\Delta p = \frac{\xi}{\chi} \left(\frac{N}{2\rho} \right) \left(\frac{\dot{m}}{A_{Eff}} \right)^2 \chi \tag{4.6}$$

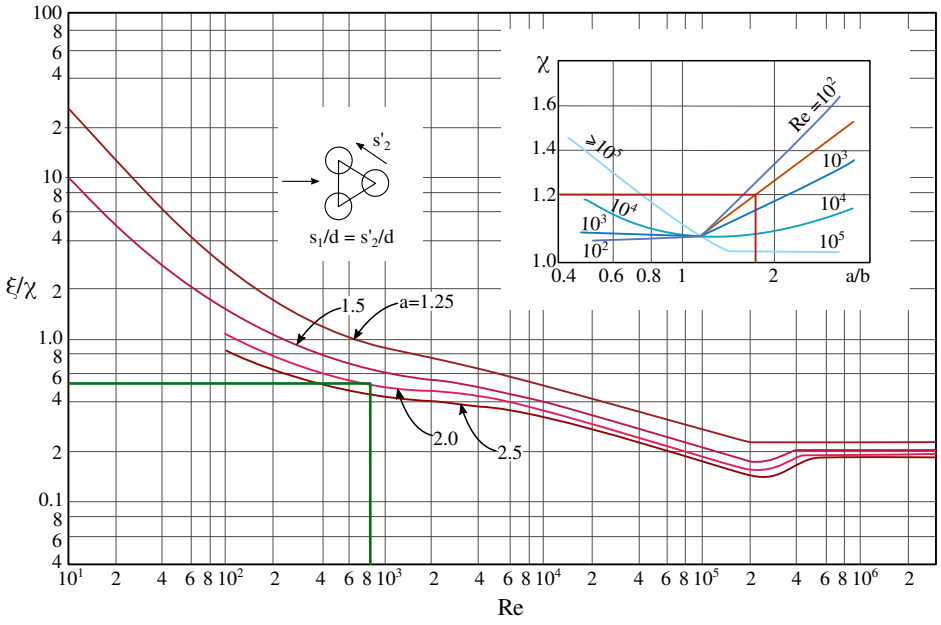

Figure 4.7: Friction coefficient (ξ) and the correction factor (χ) ratio as a function of Re and a for use in Eq. 4.6 for staggered tube arrangement. Adapted from Žukauskas [89] and [83].

Where $a = s_1/d$ and $b = s_2'/d$, given the same dimensions s_1, s_2' and d from Fig. 4.6 and Tab. 4.1. For the R_e number, it was followed the recommendation by Kazimi

& Todreas [83] , since they too adopt this Žukauskas methodology. Eq. 4.7 presents the equation used for finding the applicable R_e number to this graphical method.

$$R_e = \frac{d \cdot \dot{m}^2}{\mu} \tag{4.7}$$

With all the above-mentioned equations, the following inputs were obtained: $a = 2.035$, $b = 1.175$, $a/b = 1.7319$, and $R_e = 801.7687$. Although this value is close to the previous $Re_m = 781.3301$, it is different due to the velocity considered, where for Re_m, the w_{0m} was used, for this R_e, w_{in} was used. Since both are close in magnitude, the author chose to keep following the recommendations described in each method.

By intersecting in the graph (illustrated in Fig. 4.7) it is obtained: $\chi \simeq 1.2$ and $\xi/\chi \simeq 5.0$. Thus, inputting in Eq. 4.8:

$$\Delta p = \frac{5}{1.2}\left(\frac{8}{2\rho}\right)\left(\frac{\dot{m}}{A_{Eff}}\right)^2 1.2 = 1728.9838\ Pa \tag{4.8}$$

Finally, with Eq. 4.1 the $C_2 = 600\ m^{-1}$ coefficient value could be determined and implemented to the second SGs porous media model.

It is worth noting that this value is significantly larger than the previously obtained, and this lead to the understanding of the importance of comparing both strategies.

4.2.5 Steam Generator heat sink function

This last subsection explores the methods for defining the heat sink function. At first, it was thought that a simple constant-value volumetric (negative) energy source would solve the problem. However, several early tests with this condition showed that it was not adequate for modeling the SGs thermal behavior, due to the following identified points:

1. The use of a constant negative energy source led to an excessive local cooling behavior since the whole simulation domain was started at the same temperature $T = 683\ K$. Even if time were accounted for in a startup transient condition, the SGs would be much colder when the heated fluid got to it;

2. The SGs are expected to have heat removal power at a maximum ($1.05\ MW$), given engineering limitations, and at a minimum (zero or close to zero) to avoid coolant freezing at last. So without a temperature-dependent heat sink function, the SGs would keep removing energy from the coolant at a maximum rate even if was below

freezing temperature. Thus, it is only logical to try to work a less aggressive function in lower coolant temperatures, and constant above a certain working temperature.

3. There is a fixed temperature drop expected from the SGs, which should be the same as the temperature increase from the core. Given the nature of the forced convection around the tube bundles, the coolant's temperature variation (ΔT) within the SGs influences directly its heat extraction. Therefore, with the same ΔT as observed in the core, it is possible to define the function mentioned in point 2.

To address the points mentioned above, the approach for the volume heat sink was based on Eq. 4.9, which is a simple modification of the Specific Heat Capacity correlation in terms of energy rate and the SG volume (V_{SG}).

$$Q'''_{SG} = \frac{\dot{m} \cdot C_p}{V_{SG}}(\Delta T) \tag{4.9}$$

However, to turn the expression in Eq. 4.9 into a function of coolant temperature through the SG volume, it was necessary to establish the constants and variables involved. As per the recommendation of [90], if ΔT were to be assumed as the difference $\Delta T = (T_s - T_{fluid})$, where T_s is the tube bundle surface temperature, the heat exchange rate could be significantly overestimated. [90] proposes that as $T_{fluid} \to T_s$ and $|\Delta T| \to 0$, ΔT's appropriate form should be the logarithmic temperature difference ΔT_{lm}, presented in Eq. 4.10.

$$\Delta T_{lm} = \frac{(T_s - T_i) - (T_s - T_o)}{\ln\left(\frac{T_s - T_i}{T_s - T_o}\right)} \tag{4.10}$$

Where T_i and T_o are the coolant's inlet and outlet temperatures from the SGs. Therefore, by combining Eq. 4.9 and Eq. 4.10, it is possible to achieve a preliminary Heat Sink Function with relation to the SG inlet coolant temperature, given by Eq. 4.11.

$$Q'''_{SG}(T_i) = \frac{\dot{m} \cdot C_p}{V_{SG}} \cdot \left[\frac{(T_s - T_i) - (T_s - T_o)}{\ln\left(\frac{T_s - T_i}{T_s - T_o}\right)}\right] \ [MWm^{-3}] \tag{4.11}$$

Where the $\frac{\dot{m} \cdot C_p}{V_{SG}} = 0.84549\ MW/m^3$ term is taken as a constant, given $C_p = 146.415\ J/kgK$ at $T = 683\ K$ and $V_{SG} = 0.0284\ m^3$ measured in the Fluent model. $T_o = 663\ K$, as the

desired SG outlet temperature, which should be the same as the SEALER's core inlet temperature, modeled in Chapter 3.

On the other hand, T_s was obtained by successive attempts to adjust the function. The reason for the trial and error approach instead of an analytical one is due to the function shape and domain limits. For instance, as mentioned in point 2 of this subsection, there are upper and lower limits that the function should respect, and if unrestricted, the function from Eq. 4.11 surpasses the maximum heat removal power and also reaches its zero in temperatures below freezing. To address this issue, domain limitations were tested, and adjusted by varying the values for T_s and T_{min}, the temperature for which all function values give 0 MW/m^3. Fig. 4.8 shows the graphical representation of the considered SG heat sink functions, whose parameter combinations are described in Tab. 4.3.

It is important to note that although T_s originally refers to a tube surface temperature, in this model, it should be understood only as a constant in a function, as there are no surfaces in the SG porous region. This approach can be considered adequate since the whole model is simulated under a steady-state condition, where just the energy balance is of interest.

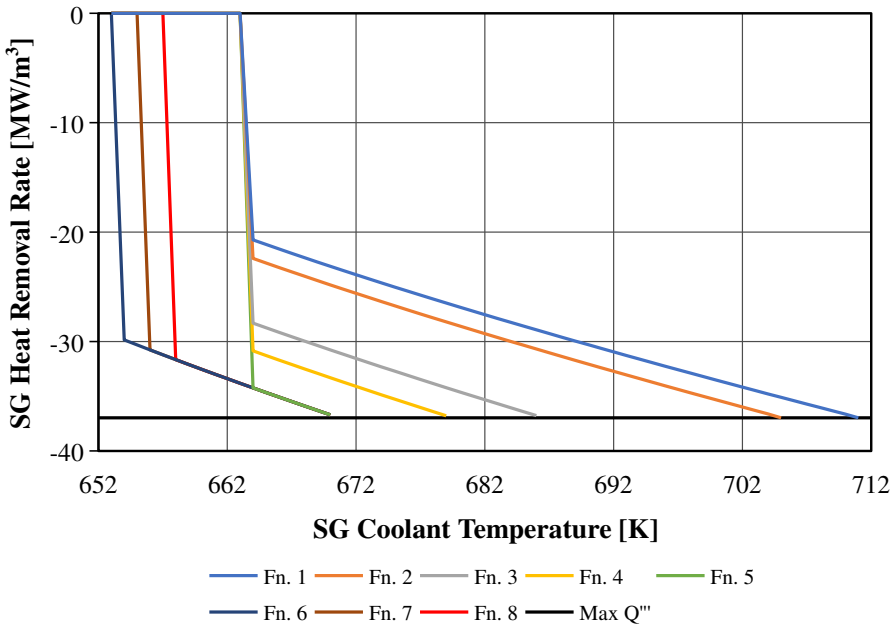

Figure 4.8: SG Heat sink functions.

These tests were run in steady-state simulations, with a preliminary Idelchik SG model, using the same methods presented in Chapter 3. The comparison is shown in Tab. 4.4. Also, cases with the Žukauskas model, and with transient simulations were also run, but showed no relevant (larger than 1 K) differences. Thus, only the referred steady Idelchik SG model was used in this comparison.

Table 4.3: Average temperatures with varying function parameters.

SG Function Variation	Function Parameter [K]			
	$\mathbf{T_0}$	$\mathbf{T_s}$	$\mathbf{T_{max}}$	$\mathbf{T_{min}}$
1	663	639	711.00	663
2	663	637	705.50	663
3	663	630	686.50	663
4	663	627	679.50	663
5	663	623	670.50	663
6	663	623	670.50	653
7	663	623	670.50	655
8	663	623	670.50	657

After the successive tests, Function 8 was chosen, with $T_s = 623\ K$ and $T_{min} = 657\ K$, for providing a Cold Pool average temperature closest to 663 K, as observed in Tab. 4.4.

Table 4.4: Average temperatures with varying function parameters.

SG Function Variation	Volume Averaged Temperature [K]	
	Hot Leg	**Cold Pool**
1	739.62	697.52
2	733.61	691.55
3	716.74	674.75
4	711.92	669.96
5	710.90	668.96
6	702.78	660.86
7	703.66	661.75
8	704.95	663.07

Finally, given the additional conditions presented, the final heat sink function employed is presented in a set of four conditional functions, presented in Eq. 4.12 It is important to note that the function in Eq. 4.11 is undefined in $T_i = 663\ K$, for this reason, it was also considered as a conditional. For the maximum heat sink power, the design value of 1.05 MW was simply divided by the CAD-obtained region volume of 0.0284 m^3, leading to a maximum volumetric power of $-36.9752\ MW/m^3$

$$Q'''(T_i) = \begin{cases} 0\ [MW/m^3],\ T_i \leq 657\ K \\ Q'''_{SG}(T_i),\ 657\ K \leq T_i \leq 670.5\ K \\ -36.9752\ [MW/m^3],\ T_i \geq 670.5\ K \\ -33.8195\ [MW/m^3],\ T_i = 663\ K \end{cases} \tag{4.12}$$

The function above was applied to Fluent as a UDF input, shown as follows:

Listing 4.2: User Defined Functions - Heat Sink source for the SGs.

```
SG_Function == IF(StaticTemperature<=657[K], 0[W m^-3], Cond_1)

Cond_1 == IF(StaticTemperature<=670.5[K], Cond_2, -36.9752e6[W m^-3])

Cond_2 == IF(StaticTemperature == 663[K], -33.81957e6[W m^-3], Log_Temp)

Log_Temp == 0.845492183e6[W m^-3]*(((623[K] - StaticTemperature) +
+ 40[K])/(log((623[K] - StaticTemperature)/(-40[K])))/1[K])
```

4.2.6 Meshing and solver

Following Chapter 3's meshing study in Subsection 3.2.8, the models evaluated in this Chapter employed the same meshing parameters defined, resulting in a mesh size of 513,192 polyhedral volume cells. Tab. 4.5 presents its general quality parameters.

Table 4.5: Mesh quality parameters.

Mesh Quality Parameter	Value
Number of Volume Cells	513,192
Minimum Orthogonal Quality	0.200
Average Orthogonal Quality	0.935
Maximum Aspect Ratio	84.829

Since solid regions were included, they also had to be meshed. Fig. 4.9 presents the interface between the solid and fluid regions on the YZ plane. Attention should be paid to the prism inflation layers, expanded to all the new volumes (Hot Pool and Cold Leg).

Fig. 4.10 and Fig. 4.11 present some volume mesh cross sections, where the polyhedral cells' sizes and distribution in each region can be more intuitively visualized.

The solving scheme was the same as the one employed in Chapter 3, i.e.: first a steady solution, for 2000 iterations, followed by a transient solution of 10 s, using a $CFL = 10$, until solution stabilization. Both steps used ANSYS Fluent's Coupled solver.

4.3 Partial Results

In this results section, the proposed methodologies in this chapter are evaluated individually, followed by the complete SEALER reactor results for temperature, velocity, and pressure fields.

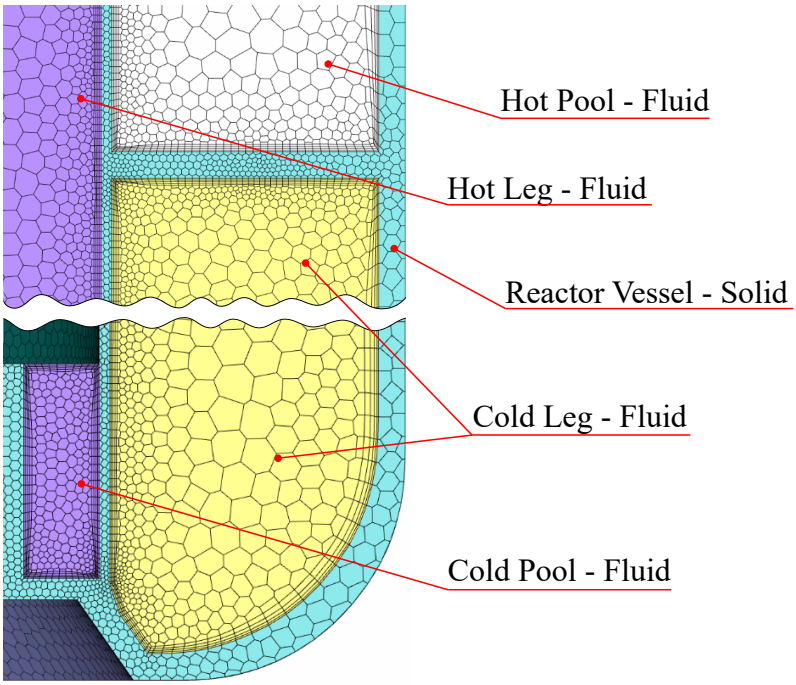

Figure 4.9: Inflation layers - Inflation layers details.

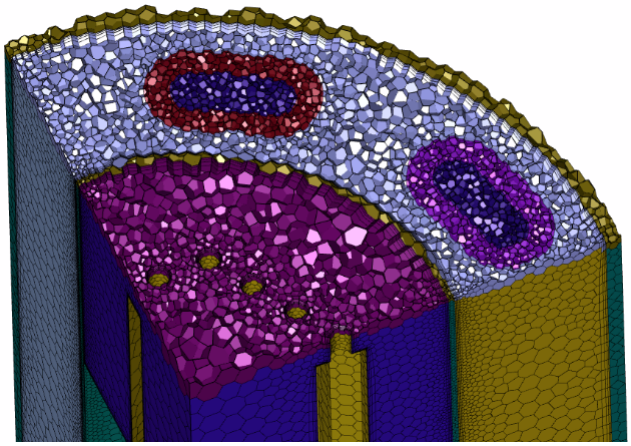

Figure 4.10: Volume mesh cross section on the $Y = 2.5\ m$ plane.

Since a comparison between the PM based on Idelchik [88] and on Žukauskas [89] was initially proposed, the first results will be on the behavior and influence of using the two models.

Before proceeding to the results, Table 4.6 indicates the position of the lines and planes where the model comparisons will be made. Fig. 4.12 shows the plans proposed to report the results. The new lines are placed on the Plane $Y = 0.55\ m$, along the SG2 (closer to the YZ plane) longitudinal and transversal axes.

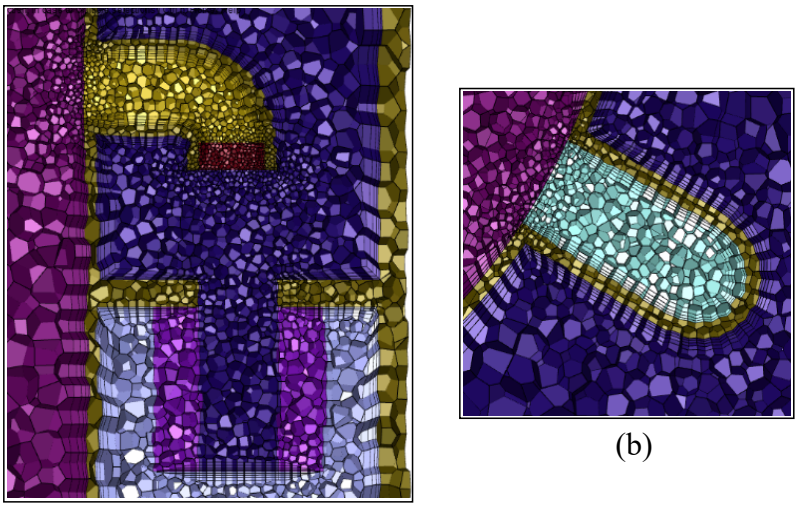

Figure 4.11: Volume mesh details. (a) Pump 1 and SG 1 lateral cut and (b) Pump 2 vertical cut.

Table 4.6: SG evaluation lines.

Line Name	Line Origin [m]	Line End [m]
SG Longitudinal	$(0, 2.5, -1.16)$	$(-0.58, 2.5, -1)$
SG Transversal	$(-0.24, 2.5, -0.93)$	$(-0.325, 2.5, -1.25)$

4.3.1 Idelchik and Žukauskas SG Porous Media comparison

As previously presented in the Subsection 4.2.4, the two different approaches for defining the pressure drop of the staggered-tube SG gave the coefficients $C_2 = 390.3089\ m^{-1}$ (Idelchik model) and $C_2 = 600\ m^{-1}$ (Žukauskas model). Since this difference was considerable, the author proposed to simulate the SEALER Full Loop model with both considerations and compare them.

Once the only difference between both models lies in the SG PM coefficient, the volume-averaged temperatures of the SEALER's main regions are evaluated to check the models' impacts on the whole domain, shown in Tab. 4.7, and also, curves and contours from the SG region are considered, to asses the local influence, presented in Fig. 4.13.

Table 4.7: Volume-averaged temperature comparison for the SG PM models.

	Idelchik PM	Žukauskas PM	Difference [K]
Cold Leg [K]	664.07	663.74	-0.33
Cold Pool [K]	663.07	662.92	-0.16
Hot Leg [K]	704.95	704.82	-0.13
Hot Pool [K]	704.00	703.79	-0.21
Average [K]	682.01	681.76	-0.26

From both comparisons presented above, it is clear that although the C_2 values

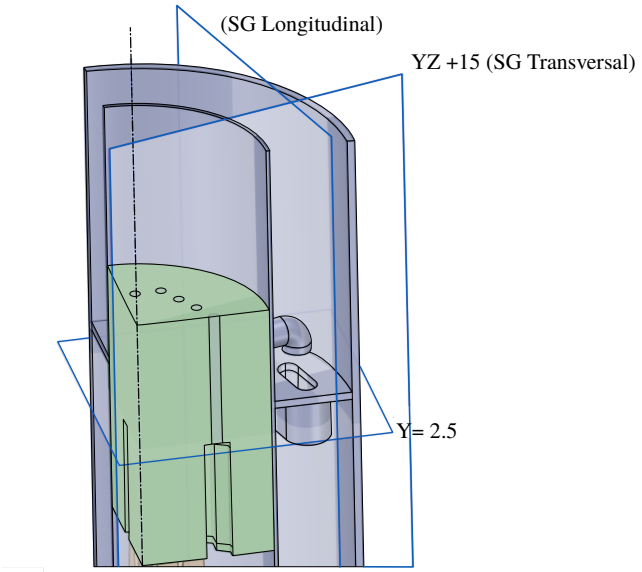

Figure 4.12: New evaluation planes.

were far from each other, their impact on the whole domain and also locally was not significant. Given the proximity of values in the temperature and velocity plots, contours are not presented, for they are mostly indistinguishable. This leads to the understanding that both C_2 coefficients are in an adequate order of magnitude and that either approach can be considered acceptable.

However, the Žukauskas model provides an easier path to determining the pressure drop value and requires fewer assumptions to reach this goal. Additionally, since it is also employed as a main reference in many textbooks, it should be the SG PM model of choice in the next Sections.

4.3.2 Periodic Boundary Condition (PBC)

One of the most direct ways to evaluate the adequacy of the PBC is to check if there is continuity from one side to the other, visible in matching contours on both sides of the PBC. Fig. 4.14 and 4.16 present the contours for velocity magnitude and temperature, respectively, on the YZ and XY planes. In the figures, it is possible to observe that the contours on both sides of the PBC (Hot Pool and Cold Leg) do match, whilst the contours in the Hot Leg, where symmetry BC was used, do not. Fig. 4.15 presents the velocity magnitude contours at some of the SEALER's cross-sections. Also, in all of them, there is flow continuity from one PBC plane to the other.

From the velocity contours presented, there is a notable predominance of low velocities in the Hot Pool and Cold Leg, with the exception of the pump region, presented

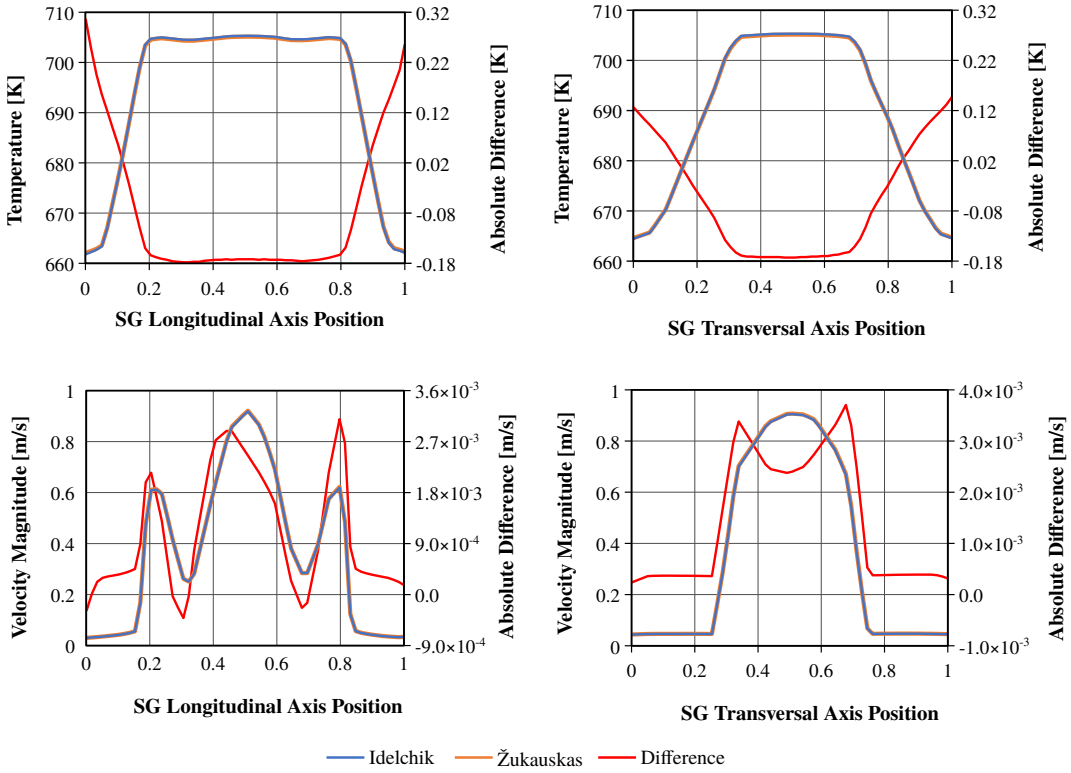

Figure 4.13: Temperature and velocity inside SG2 comparison.

in detail in the next Subsection, and closer to the Cold Pool inlets, where fluid is sucked in.

Fig. 4.17 presents an extended view of a cross-section of the SEALER, at the plane $Y = 2.5\ m$. The pink lines indicate the cuts where PBC was applied, and the blue line, where symmetry was used. In this figure, the contour continuity is evident around the SGs.

Both temperature contours show that the hot regions are mostly homogenized at the Core's average outlet temperature, rapidly cooling when passing through the SGs, as highlighted in Fig. 4.17. The coldest temperatures are found around, and between, the SGs, where less mixing happens, and small recirculation patterns appear, as shown in the next Subsection. There was, however, no observable temperature stratification in the cold regions.

In conclusion, the contours above demonstrate that the PBC provides noticeable differences in flow contours, and allows for the CAD model to properly represent the asymmetry in the pumps and SG distribution.

4.3.3 Pump and SG Behavior

This subsection focuses on the local evaluation of the Pump and SG region. As presented in this Chapter's Methodology Section, both the pump and the SGs were modeled upon some simplifications.

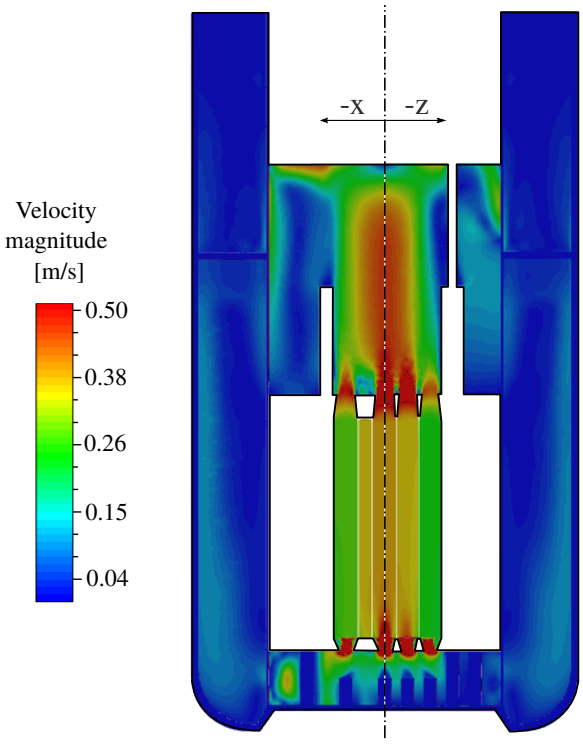

Figure 4.14: Velocity magnitude contour - Transversal YZ and XY Planes.

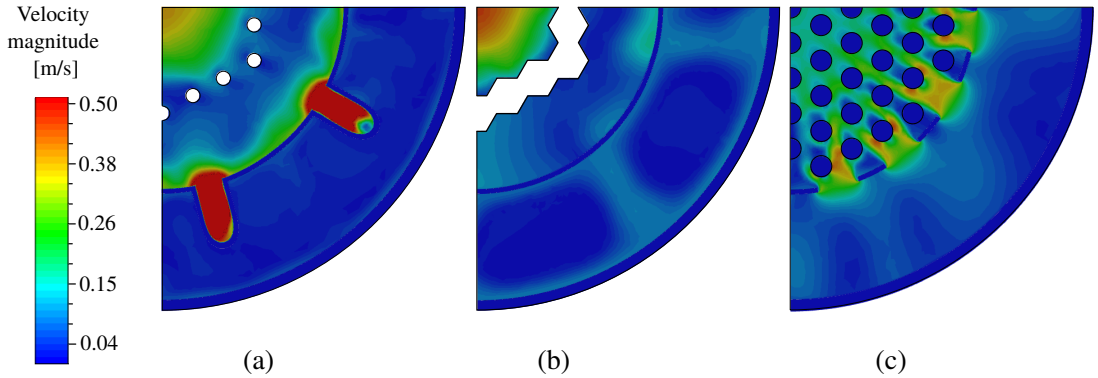

Figure 4.15: Velocity magnitude contour - Cross-section Planes at (a) $Y = 3.1\ m$, (b) $Y = 2.3\ m$ and (c) $Y = -0.4\ m$.

For the pumps, the RBC was applied to provide the constant mass flow rate value of 164 kg/s, considered as acceptable for the global SEALER steady operation conditions. Thus, no additional evaluation is necessary for the pumps, besides their adequate functioning, which was assessed by measuring the mass flow rate and flow direction, both compliant.

For the SGs, two main methods were previously evaluated as well. The temperature-dependent heat sink functions, whose sole purpose was to balance out the energy input by the core, while providing a stable solving process. As mentioned in the Methodology, the function selected met those two requirements, by matching the design-defined volume-averaged temperatures in the main regions and allowing for a self-stabilizing solution. Fig.

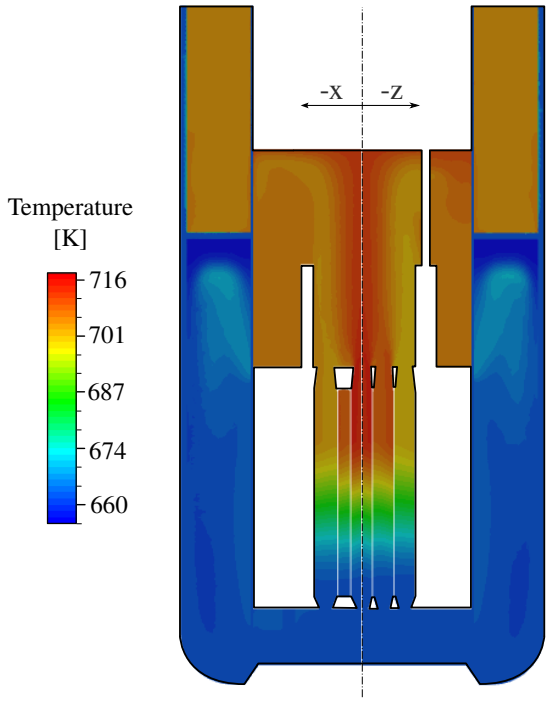

Figure 4.16: Temperature contour - Transversal YZ and XY Planes.

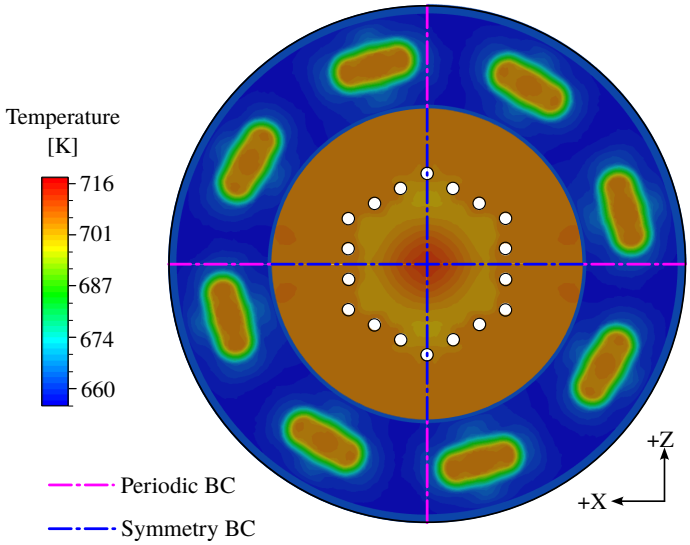

Figure 4.17: Temperature contour - Y=2.5 m extended plane.

4.18 presents an example of this latter aspect, where the average temperatures of many regions were monitored during the CFD case solves. The brown and red curves represent the SGs' oscillating behavior in the beginning, but converging later.

Fig. 4.19 presents the temperature contours on the evaluation planes for the pump and SG region. In this figure, the coolant temperature transition from hot to cold is more evident in a 3-dimensional visualization, where the SG porous volume successfully removes the heat uniformly across its domain.

Although the temperature contours appear to show a homogeneous field in each

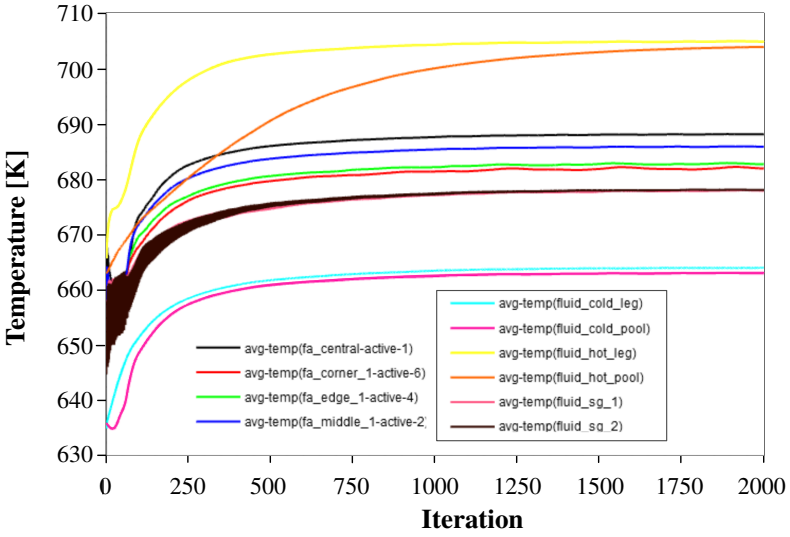

Figure 4.18: Volume-averaged temperature monitors during the steady solving.

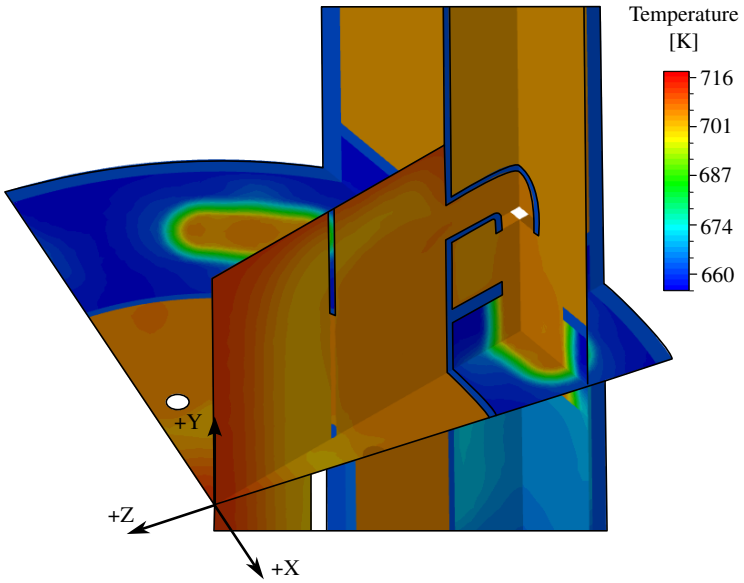

Figure 4.19: Temperature contour SG evaluation planes.

region, this is not the case for the velocity vector fields, presented in Fig. 4.20. In the SG transversal plane, Fig. 4.20 (a), it is possible to visualize that some of the pumped coolant is deflected upwards upon hitting the walls around the SG entrance, however, when inside the SG, the downward flow is mostly slowed down while passing through the SG volume. The deflected flow helps to explain the homogeneous temperature distribution in the Hot Pool, as part of the mixed Hot Leg fluid is directly recirculated.

In the longitudinal plane in Fig. 4.20 (b), an interesting recirculation behavior can be observed, where part of the pumped flow returns to the outflow jet, and mostly does not escape the region, as the surrounding vectors indicate.

Finally, in Fig. 4.20 (c), it is possible to observe that the outward flow from both

SGs is regular in all directions, a behavior that is consistent with the PM setup of the C_2 coefficient in the transversal axes. There is a clear interface where the streams from both SGs meet, but do not cross each other. In this interface, the flow is diverted vertically, mostly downwards, given the gravitational influences.

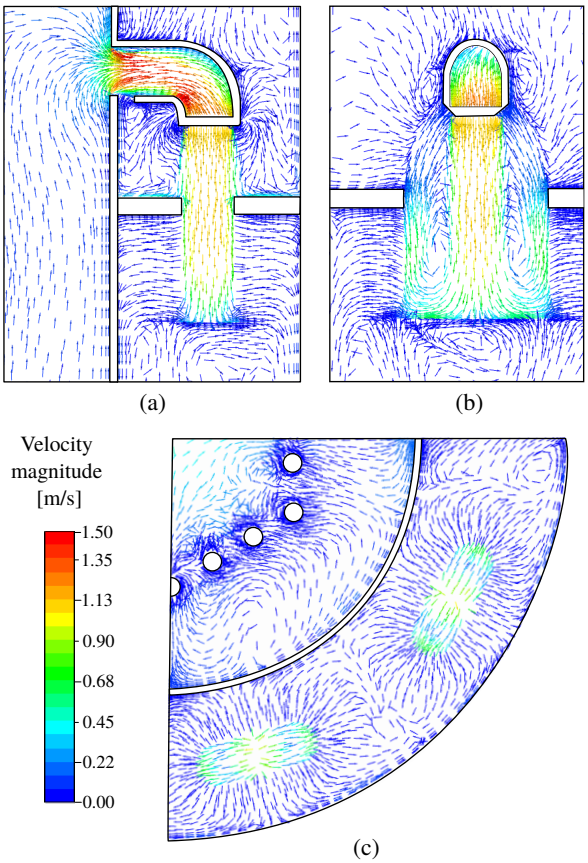

Figure 4.20: SG Velocity vector fields - (a) SG transversal plane, (b) SG longitudinal plane, and (c) $Y = 2.5\ m$ cross-section plane.

4.4 Partial Conclusions

In this Chapter, the SEALER model was expanded from the Core Barrel region to its full primary circuit. Aside from the included regions (Hot Pool and Cold Leg) that were sectioned with the Periodic Boundary Condition assumptions, the pumps and SGs were included in the model. The pumps were simplified to a constant mass flow rate Recirculating Boundary Condition, and the SGs volumes were modeled as porous media, with a temperature-dependent heat sink function.

The results evaluated from the employment of these methods allowed for the following conclusions:

1. The PBC was the right and most adequate BC for this case;

2. The RBC was adequate for the pump modeling;
3. The heat sink function was correctly calibrated;
4. The Žukauskas model should be the one chosen for modeling SG porous media; and
5. The whole combination of the models in Chapter 3 and the ones presented in Chapter 4 work in conjunction, which makes it possible to simulate the full SEALER primary loop in a steady-state condition.

Finally, once the SEALER CFD model is successfully set, with the main hydraulic and thermal aspects functional, the final chapter can proceed, where more thermal BC are explored. The following chapter analysis could only be carried out once this chapter provided robust indications that the CFD model is adequate for normal steady-state simulations.

Chapter 5

SEALER Heat Transfer Analysis

This Chapter is the third part of the proposed SEALER analysis, in which a more complete thermal evaluation is carried out. The results from Chapter 4 showed that the full SEALER steady-state modeling strategies could be used to accurately simulate both the basic thermal aspects and the full hydraulic behaviors.

Now, the SEALER model is expanded to account for additional thermal effects, namely the Conjugate Heat Transfer (CHT) between solids and fluids, conduction within solid regions, and natural convection and radiation on the Reactor Vessel (RV) outer surface. New volume regions were included in this Chapter's model, and their influence is assessed by comparing the temperature field results with the last Chapter's model. A parameter space investigation approach is used to understand how these variations in modeling affect SEALER's temperature field in steady-state conditions.

Additionally, a fuel temperature analysis for a steady-state Beginning of Life (BOL) condition is carried out using the analytical formulations from [83]. This part is complementary to the first part of the SEALER analysis, focused on the Core Barrel Region, and the core modeling. The primary motivation for this evaluation is to understand how the new thermal considerations (CHT, natural convection, and radiation) impact the fuel's temperature under the simulated conditions. With this more complete thermal model, the temperature fields within the FAs can be considered more accurate for the fuel temperature analysis when compared to the model from Chapter 3.

5.1 Motivation and objectives

This Chapter takes the SEALER analyses, which have mostly been hydraulic up to this point, and add a more complete thermal approach that takes into account some of

the main ways energy moves around, like conduction, natural convection, and radiation. All the already established engineering methods, including the porous media and heat generation/sink functions, were kept as they were.

Ultimately, this Chapter aims to demonstrate the importance of considering (and modeling) these thermal behaviors when simulating nuclear systems, in this case, a lead-cooled SMR. Although this statement might sound obvious at first, it is important to reiterate that many models based on conventional STH codes and even on more complex CFD approaches tend to ignore these thermal effects [79][78]. As will be presented later on, the considerations of these effects lead to noticeable temperature field differences when compared to the previous adiabatic model's results.

5.2 Methodology

5.2.1 CAD model and meshing

The model employed in this Chapter is an expanded version of the previous model, including the Core region outside the FAs, representing the secondary assemblies (control, shield, and reflector) and by-pass volumes, and the control rods' hexagonal wrapper extensions volumes. Fig. 5.1 highlights these added volumes.

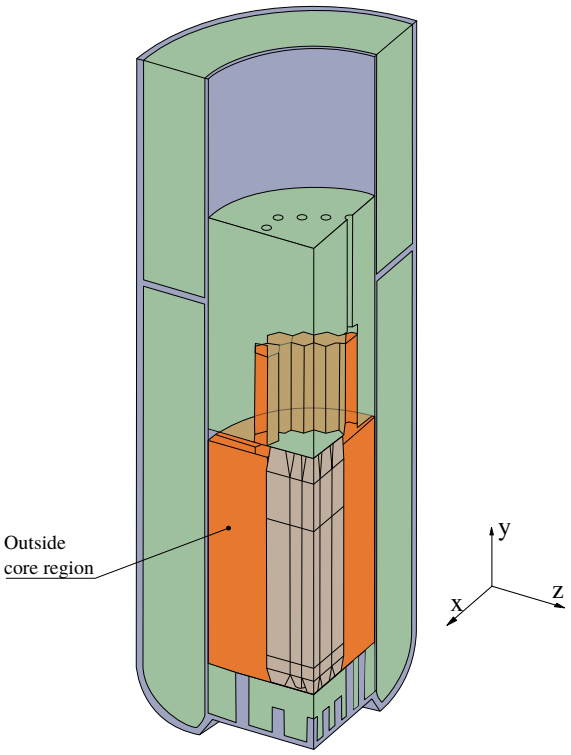

Figure 5.1: Highlighted added volumes to the model.

Once the new regions were included, the number of shared region interfaces conse-

quently increased. The excessive overlapping of surfaces usually leads to meshing difficulties in ANSYS Fluent Mesher, especially during the Shared Topology (ST) step [11]. For this reason, gaps between those regions were considered, as seen in Fig. 5.2 Although some completely filled models were tested, all failed in this ST meshing step, especially on the Cold Pool/Core and Core/Hot Leg interfaces, where more detailed geometries are found (e.g.: the cylindrical feet and hexagonal wrapper extensions).

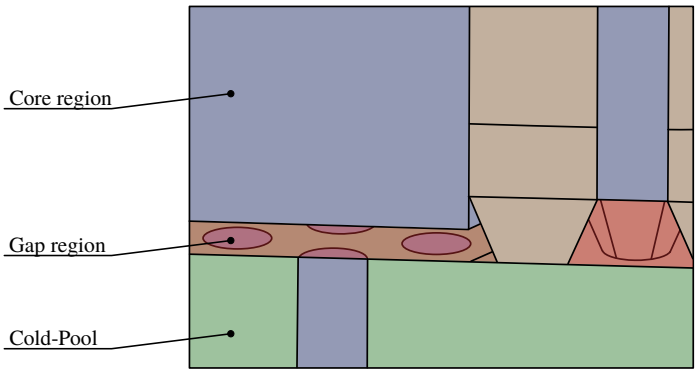

Figure 5.2: Gap in the Cold Pool/Core interface.

5.2.2 Solid materials' thermophysical properties

As previously mentioned in this work, the coolant flow within the secondary core assemblies, by-pass regions, and the control rods' wrapper extensions is mostly negligible. Because of this consideration, the added volumes were modeled as solid lead with the same material properties as the coolant, presented in Tab. 3.5, except for the density, which was defined with a constant value. This approach was chosen to avoid the computational costs of solving momentum and continuity equations in stagnant flow regions without losing insights from the thermal aspects, which could be restricted to simple heat conduction.

The structural Stainless Steel (SS) 316L parts were modeled using the temperature-dependent thermophysical properties from [91]. Tab. 5.1 presents the property functions for all valid temperature ranges of $298\ K < T < 1670\ K$.

Table 5.1: Thermal-physical properties of Stainless Steel 316L. Adapted from [91].

Property	**Function**	**Units**
Density (ρ)	$\rho = 7771$	$[kg/m^3]$
Thermal Conductivity (k)	$k(T) = 9.248 + 0.01571 \cdot T$	$[W/m\ K]$
Specific Heat (C_p)	$C_p(T) = 459.292 - 0.132889 \cdot T$	$[J/kg\ K]$

The other materials considered in this chapter are the cladding 2R72 (15-15Ti alloy, and the UO_2 fuel pellets with 4% porosity and 19.75% enrichment. Both these materials

are not in the CFD model but were considered in the fuel temperature analysis, where their conductivity had to be calculated at certain temperatures. Eq. 5.1 and Eq. 5.2 present the temperature-dependent functions used for the cladding, and the fuel, respectively [92].

$$k_{clad}(T) = 7.598 + 2.391 \times 10^{-2} \cdot T - 8.899 \times 10^{-6} \cdot T^2 \tag{5.1}$$

$$k_{UO_2}(\tau) = 1.158 \left(\frac{100}{7.5408 + 17.692 \cdot \tau + 3.6142 \cdot \tau^2} + \frac{6400}{\tau^{5/2}} \cdot e^{(16.35/\tau)} \right) \cdot \left(\frac{1 - p_o}{1 + 2p_o} \right) \tag{5.2}$$

where $\tau = T/1000$ and p_o is the fuel porosity, considered equal to 0.04.

5.2.3 Conjugate Heat Transfer (CHT)

The CHT condition was applied to all the two-sided walls, which are interfaces between fluid and solid regions. In Fluent, to allow heat transfer between these separated regions, different approaches can be implemented, e.g.: by defining a fixed heat flux value, a heat generation rate, a fixed temperature, or by coupling both sides of a two-sided wall, which was the option adopted. There were, however, two different situations for coupled walls in the model, presented below.

On thin walls

In some cases, where walls are too thin, modeling the wall solid region would lead to an excessively skewed, or refined volume mesh, both undesired outcomes. There is an alternate option, which is to model them as zero-thickness walls and define their parameters of interest when applicable. This was the case for the FA wrapper walls (2 mm), modeled with zero-thickness since Chapter 3, having in mind the addition of the solid lead region around the FAs (explained in subsection 5.2.1).

The coupled thermal boundary condition was applied to all the FA walls and also to the control rods' extensions. To account for the thermal resistance of these SS 316L walls, a virtual thickness of 2 mm was defined, as per the original design [23]. There is, nonetheless, a peculiarity for thin-wall coupled conditions in Fluent, that for the wall materials, only constant values can be specified for the thermal conductivity (k) [11]. To satisfy this restriction, a material with a constant k was employed on these walls, with its value calculated using the function in Tab. 5.1 at 683 K, the volume-average temperature

within the FAs.

Another important point to address in this subsection is the use of the "shell conduction" BC, which Fluent uses to calculate two-dimensional heat conduction within the wall, not only across it. Although it was tested, negligible differences were noted in the results, possibly because of the steady-state condition of the problem. The main issue found with its use was the Fluent case instability errors when trying to save the ".cas" file whenever the case had the outer radiation activated. This issue, combined with the lack of contribution to results, led to avoiding the shell conduction BC altogether.

On thick walls

On the other hand, the thick walls, such as the Core Barrel and the Reactor Vessel, were indeed modeled as solids with their real thickness. The surfaces separating fluid from solids could be defined as "coupled", without additional considerations since the solids are the heat conductors in this case. This situation also allows the use of temperature-dependent properties without impediments.

5.2.4 Thermal BCs on the outer Reactor Vessel

In this Subsection, the thermal BCs on the outer RV are explained. Combined with the CHT, the external energy loss on the domain's boundary is expected to lead to differences in the temperature fields when compared to the adiabatic model from the previous chapter.

Since no details could be found in the available references, some assumptions were made to account for the heat loss on the outer surfaces, they are: I) The RV wall is surrounded by air at atmosphere pressure, and the natural convection phenomenon is present; II) The RV surface is plain SS 316L, and energy losses from thermal radiation are present; and III) temperatures from 300 K to 550 K, with 50 K steps, were considered as possible outside environment (controlled or not) conditions.

Based on those three assumptions, both natural convection of air and radiation effects were modeled. Table 5.2 presents the different BC used in the cases simulated, which differ by varying the convective free stream temperature (T_{fs}) and the radiative external temperature (T_{∞}). "A" stands for "Adiabatic", "R" for "Radiation only", and "RC" for "Radiation and Convection". The cases will be referred to by the combination of BC and temperature, for example: "RC550K" refers to the case with radiation and convection BC at a reference temperature of 500 K. Although a "C" (Convection only)

condition was envisaged, it is understood that radiation alone can occur (if in a vacuum surrounding), but convection alone is not as likely, considering that the convective fluid would need to be completely opaque for this to happen.

Table 5.2: Cases for comparing the thermal losses on the outer RV wall.

	Case							
	A	**R**	**RC**					
Radiation T_∞ $[K]$	-	300	300	350	400	450	500	550
Convection T_{fs} $[K]$	-	-	300	350	400	450	500	550

To evaluate the influence of the inclusion of the new volume regions, presented in subsection 5.2.1, the adiabatic model used in Chapter 4 is used for reference, and compared with the CHT A condition. To evaluate the influence of the natural convection and radiation BCs, the A, R300K and RC300K are compared. Cases RC300K to RC550K evaluate the influence of different outer temperatures for the RC conditions. Further details are presented in the Partial Results Section.

The average surface temperature on the RV wall of $T_w = 675\ K$ is used as a reference for the convection calculations for all the other cases. It is worth noting that while T_w should be defined through an iterative process of defining the convective coefficient ($\hbar$), then T_w, and so forth, no difference was observed when doing so. The tests done indicated that the surface temperature (variations in the order of a few K) did not affect significantly the natural convection as much as the free stream bulk temperature.

To model the combination of the two heat transfer methods in ANSYS Fluent, there is the combined external heat transfer condition (or Mixed option), which accounts for the sum of the convective and radiative effects, presented in Eq. 5.3 [11]:

$$q'' = \hbar(T_{fs} - T_w) + \varepsilon\sigma(T_\infty^4 - T_w^4) \tag{5.3}$$

where q'' is the total heat flux on a surface, ε its radiative emissivity, $\hbar$ the convective heat transfer coefficient, and $\sigma = 5.67037 \times 10^{-8}\ W/m^2\ K^4$ is the Stefan-Boltzmann's constant.

Radiation

The External Radiation BC was considered to happen mainly on the outer RV but also on the zero-shear walls, which represent the lead coolant's free surface. As inputs in Fluent, just the External Emissivity (ε) and External Radiation Temperature are sufficient

to define this boundary condition.

The value of $\varepsilon = 0.329$ was considered for the outer RV SS 316L surface, based on the studies and experimental measurements of ε by [93] and [94] of SS 316L hemispheres at different temperatures and surface finish conditions. The used value was obtained using the available data for a 1000-hour oxidized SS 316L hemisphere surface at 675 K. Fig. 5.3 presents the used data plot for this sample and the interpolated region.

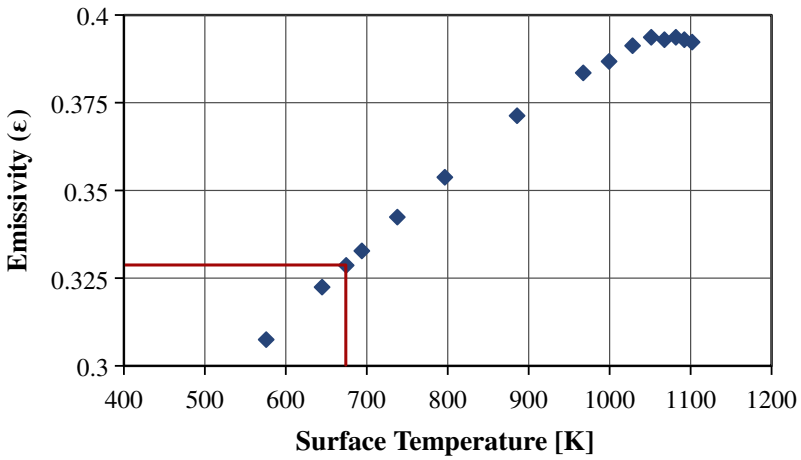

Figure 5.3: SS 316L Emissivity as function of surface temperature. Adapted from [94].

For the coolant's free surfaces region, $\varepsilon = 0.95$ was set, based on the estimations used in the work of [82], and the External Radiation Temperature was set at 600 K, considering that these surfaces are contained within SEALER's physical boundaries and subjected to higher temperatures.

Natural Convection

The natural convection was accounted for on the outer surface by considering the bulk temperatures of air from Tab. 5.2, flowing around the RV with an isothermal consideration. For such, the convective heat transfer coefficient ($\hbar$) was obtained based on the approximation of the cylindrical geometry as a flat vertical plate, within a 5% error margin. Although there are some more modern and lower error methods (around 3%) [95], this approach is widely used, simple, and sufficiently accurate, as described by [95].

The flat plate assumption can be made when the cylinder's diameter (D) is considerably larger than the boundary layer thickness of the buoyant flow around this cylinder. The criterion used in this work is the one derived by [96], presented in Inequality 5.4.

$$D \geq \frac{35L}{Gr_L^{0.25}} \tag{5.4}$$

Where L is the cylinder's equivalent length, and Gr_L is the Grashof's number for this length L. As per the criterion, if the Inequality 5.4 is true, then the problem of natural convection around the cylinder can be simplified to a flat plate one. Gr_L, the dimensionless number that approximates the ratio of the buoyancy to viscous forces acting on a fluid, was calculated using Eq. 5.5.

$$Gr_L = \frac{\rho^2 g \beta \Delta T L^3}{\mu^2} \tag{5.5}$$

Where ρ and μ are the density and dynamic viscosity of air, g is gravity, ΔT is the difference between free stream (T_{fs}) and the surface temperatures (T_w), and β is the coefficient of volume expansion (approximated as $1/T_f$ in the case of air as an ideal gas), with $T_f = (T_w + T_{fs})/2$. Tab. 5.3 presents the values of these variables used to assess the criterion validity for each temperature.

Table 5.3: Air properties at the evaluated free stream temperatures. Adapted from [97].

Air Free Stream Temp. (T_{fs}) [K]	**T_f [°C]**	**ρ [kg/m^3]**	**k [W/kgK]**	**$\mu \times 10^{-5}$[kg/m s]**	**Pr**
300	214.35	0.7254	0.0387	2.6295	0.6966
350	239.35	0.6898	0.0403	2.7210	0.6952
400	264.35	0.6577	0.0419	2.8099	0.6943
450	289.35	0.6283	0.0435	2.8969	0.6937
500	314.35	0.6016	0.0450	2.9819	0.6936
550	339.35	0.5769	0.0466	3.0654	0.6937

Upon evaluation of the criterion for the given temperatures, all respected the Inequality 5.4, thus allowing us to proceed with the steps to calculate the convective heat transfer coefficient $\hbar$. For the vertical flat plate case, the Nusselt number is given by Eq. 5.6 [98], valid for an extensive $1 < Ra_L < 10^{12}$ number range, ($Ra_L = Gr_L \cdot Pr$).

$$Nu^{1/2} = 0.825 + \frac{0.387 Ra^{1/6}}{\left[1 + (0.492/Pr)^{9/16}\right]^{8/27}} \tag{5.6}$$

Finally, with Nu defined, the convective heat transfer coefficient can be obtained with Eq. 5.7.

$$\hbar = \frac{Nu \cdot k}{L} \tag{5.7}$$

Table 5.4 presents the calculated values for Gr_L, Ra_L, Nu and, ultimately, $\hbar$, for the evaluated air free-stream temperatures.

Table 5.4: Air convection coefficients $\hbar$ at the evaluated free stream temperatures.

Air Free Stream Temp. (T_b) [K]	**T_f [°C]**	**$Gr_L \times 10^{11}$**	**$Ra_L \times 10^{11}$**	**Nu**	**$\hbar$ [W/m^{2}K]**
300	214.35	12.434	8.662	1044.566	6.747
350	239.35	8.633	6.002	926.550	6.230
400	264.35	5.940	4.124	819.834	5.731
450	289.35	3.987	2.766	719.920	5.221
500	314.35	2.569	1.782	624.208	4.687
550	339.35	2.109	1.463	585.556	4.544

5.2.5 Fuel temperature analysis

In this subsection, the analytical methods for evaluating the fuel temperature are presented. The thermal resistance analogy for a cylindrical fuel is used as the main approach, as it develops from the coolant's bulk temperature results and analytically calculates the temperatures on the clad surfaces, gas gap, and ultimately, in the fuel itself, using radial one-dimensional considerations. Fig. 5.4 presents the schematic for the thermal resistances analogy.

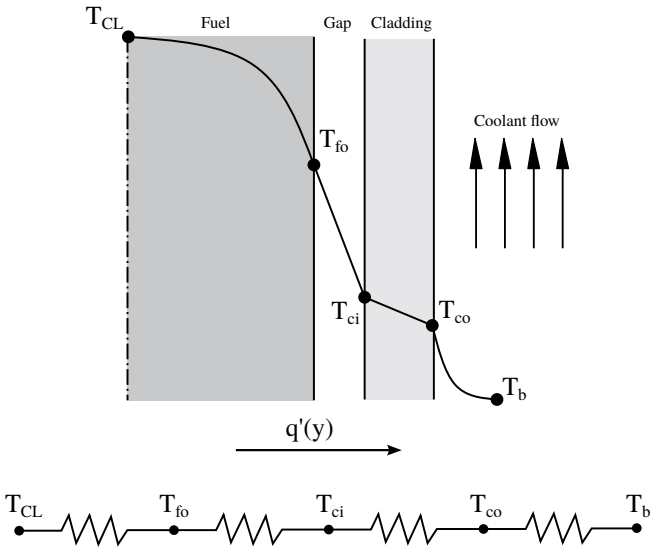

Figure 5.4: Thermal resistance analogy circuit. Adapted from [83].

Cladding outer temperature

Essentially, for each FA, the coolant's bulk temperature values are collected along the y active height (in the same FA's center lines evaluated in Chapter 3), resulting in a

function $T_b(y)$. With an array of coolant temperatures for the different y heights, and with a power distribution function $q'(y)$, the fuel's cladding outer surface temperature (T_{co}) can be obtained with Eq. 5.8.

$$T_{co}(y) = T_b(y) + \frac{q'(y)}{2\pi R_{co} h_{bundle}} \tag{5.8}$$

Where the $q'(y)$ linear power distribution function is presented in 5.9. The q'_0 is the peak linear power for a given FA. R_{co} is the cladding's outer radius, and h_{bundle} is the convective heat transfer coefficient for the wire-wrapped fuel bundle.

$$q'(y) = q'_0 \cdot \cos\left(\frac{\pi(y - H/2)}{H_e}\right) \tag{5.9}$$

The h_{bundle} can be calculated through the known sequence of finding its applicable Nusselt number first, as presented in Eq. 5.10. Nu_{bundle} is given by Eq. 5.11, D_{bundle} is the bundle's hydraulic diameter, given by 5.12 for a triangular array interior channel, and k_{Pb} is the coolant's conductivity, whose value is taken from Tab. 3.5.

$$h_{bundle} = \frac{Nu_{bundle} \cdot k_{Pb}}{D_{bundle}} \tag{5.10}$$

$$Nu_{bundle} = 0.4 + 0.33 \cdot \left(\frac{P}{D_{co}}\right)^{3.8} \cdot \left(\frac{Pe}{100}\right)^{0.86} + 0.16 \cdot \left(\frac{P}{D_{co}}\right)^{5.0} \tag{5.11}$$

$$D_{bundle} = 4 \cdot \frac{(\sqrt{3/4}) \cdot P^2 - \pi\left(D_{co}^2/8\right)}{\pi(D_{co}/2)} \tag{5.12}$$

The Péclet number (Pe) present in Eq. 5.11, is given by Eq. 5.13. The reference values for Vel_{FA} in each FA are taken from Tab. 3.1. The coolant's properties are taken from Tab. 3.5. The cladding's outer diameter is represented by D_{co}.

$$Pe = Re \cdot Pr = \frac{\rho_{Pb} \cdot Vel_{FA} \cdot D_{bundle} \cdot Cp_{Pb}}{k_{Pb}} \tag{5.13}$$

Cladding inner temperature

Having the cladding outer temperature (T_{co}) defined, its inner temperature (T_{ci}) can be obtained by solving for heat conduction with Eq. 5.14, where k_{clad} is the cladding's conductivity and R_{ci} is the cladding's inner radius.

$$T_{ci}(y) = T_{co}(y) + \frac{q'(y)}{2\pi k_{clad}} \cdot \ln\left(\frac{R_{co}}{R_{ci}}\right) \tag{5.14}$$

Fuel outer temperature

From the cladding's inner surface to the fuel's outer surface temperature, the gap heat conduction can be solved through Eq. 5.15, where R_{gap} is the gap's effective radius, and h_{gap} is its conductance.

$$T_{fo}(y) = T_{ci}(y) + \frac{q'(y)}{2\pi R_{gap} h_{gap}} \tag{5.15}$$

Fuel center-line temperature

Finally, from the fuel's outer surface temperature profile, the center-line temperature T_{CL} can be solved by conduction through Eq. 5.16, where k_{fuel} is the fuel's material conductivity.

$$T_{CL}(y) = T_{fo}(y) + \frac{q'(y)}{4\pi k_{fuel}} \tag{5.16}$$

All of the variables' values employed in the calculations, and not mentioned in the text are presented in Tab. 5.5. Fuel-related dimensions were taken from [23]. The q'_0 value for the Central FA was calculated by multiplying the core's axial and radial peak factors by its linear average power ($q'_0 = 1.41 \times 1.55 \times 4.2\ [kW/m]$). The gap conductance was estimated from [83], considering the gap size and the local linear power. The fuel conductivity was obtained from Eq. 5.2 evaluated at the average temperature of 830 K, and the cladding conductivity from Eq. 5.1, evaluated at the average bulk temperature of 700 K. Both reference temperatures were obtained by an iterative process, where the conductivity values were adjusted to their respective average temperatures (cladding or fuel), until convergence of both.

Table 5.5: Parameters used in the fuel temperature calculations.

Parameter	Value	Unit
q'_0 (Central FA)	5.922	kW/m
Clad outer radius (R_{co})	7.26	mm
Clad inner radius (R_{ci})	6.76	mm
Clad thickness ($R_{co} - R_{ci}$)	0.5	mm
Gap radius (R_{gap})	6.73	m
Fuel radius (R_{fo})	6.7	mm
Cladding conductivity (k_{clad})	19.9745	$W/m\ K$
Gap conductance (h_{gap})	250 000	W/m^2K
Fuel conductivity (k_{fuel})	4.1648	$W/m\ K$
h_{bundle}	15 284.93	W/m^2K

5.2.6 Meshing and solver

As mentioned in Subsection 5.2.1, the inclusion of the new solid volumes led to some difficulties in the meshing process, especially in the tight regions between the FAs, and in complex regions around the FA's inlets. Because of this, ANSYS Fluent's meshing tool of Shared Topology had to be more explored, along with some CAD simplifications of those complex regions, leading to small volume gaps.

Nonetheless, the meshing parameters for both the surface and volume meshes were kept the same as the ones used in Chapter 3 and Chapter 4. Tab. 5.6 presents its general quality parameters and Fig. 5.5 presents two cross-sections of the CHT model volume mesh, across the outer core and the control rod extensions regions.

Table 5.6: Mesh quality parameters.

Mesh Quality Parameter	Value
Number of Volume Cells	661,205
Minimum Orthogonal Quality	0.15
Average Orthogonal Quality	0.937
Maximum Aspect Ratio	64.145

The numerical solving schemes were the same, starting with a steady simulation, followed by a 10 s transient. Although it was noticed that the results for volume-averaged temperatures were not influenced by the transient solving, the fields and plots still needed stabilization. Thus, if not only for average comparisons, the other presented results still required the stabilizing transient solutions anyways.

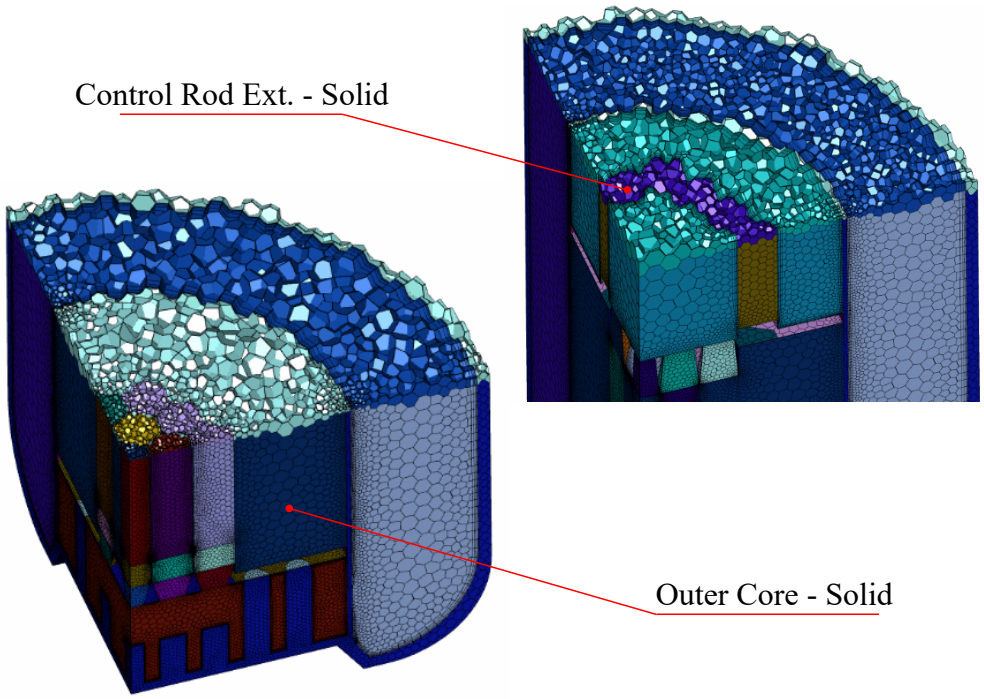

Figure 5.5: Volume mesh cross sections.

5.3 Partial Results

This results section is mainly focused on the comparison of the many cases simulated for this chapter, using a parameter space investigation approach, to understand the effects of the CHT modeling within the reactor, and the convection and radiation, outside the reactor.

1. The first analysis is on the influence of the added volumes, and their impact on the SEALER's temperature fields, due to the heat conduction through them.

2. The second analysis is on the influence of the mixed BC (natural convection and radiation energy loss). This comparison is made between the R300K and the RC300K models.

3. The third analysis is on the influence of the different outside reference temperatures. The models RC300K through RC550K were compared.

4. The fourth and last analysis is on the influence of the CHT, radiation, and convection considerations on the fuel temperature. The temperature plots and maximum values are compared for the Adiabatic, RC300K, and RC550K.

Before evaluating the results, it is important to present the planes and lines of interest. In addition to the lines and planes evaluated in Tab 3.10 and Tab 3.11, new lines

Table 5.7: Evaluation lines for the CHT models.

Line Name	Line Origin [m]	Line End [m]
Y550X		(-1.424, 0.55, 0)
Y550Z	(0, 0.55, 0)	(0, 0.55, -1.424)
Y550XZ		(-1, 0.55, -1)
Y1290X		(-1.424, 1.29, 0)
Y1290Z	(0, 1.29, 0)	(0, 1.29, -1.424)
Y1290XZ		(-1, 1.29, 1)
Y2300X		(-1.424, 2.3, 0)
Y2300Z	(0, 2.3, 0)	(0, 2.3, -1.424)
Y2300XZ		(-1, 2.3, 1)
Y3100X		(-1.424, 3.1, 0)
Y3100Z	(0, 3.1, 0)	(0, 3.1, -1.424)
Y3100XZ		(-1, 3.1, 1)

are used to analyze this chapter's results, as presented in Tab. 5.7. An additional core cross-section plane at $Y = 0.55\ m$ is also considered in the evaluation of the results.

5.3.1 Conduction through the added volumes

The inclusion of the new volumes around the reactor's core and within the control rods' hexagonal wrapper extensions led to new volume cells, through which heat conduction was considered. To evaluate the impact of these additions, comparisons between this Chapter's adiabatic CHT model and the last Chapter's adiabatic model (hereinafter referred to as 'SEALER Full Loop') were carried out. Both models had their outer reactor vessel (RV) wall modeled with adiabatic considerations.

Fig. 5.6 presents the temperature fields for both models. The first relevant difference can be seen in the filling of the void regions, where temperature gradients are now present. The Full Loop model used the adiabatic consideration for all the walls, leading to their noticeable outline. For the CHT model, as the walls allow for heat conduction, they have intermediary values when interfacing with hot and cold regions. Fig 5.7 presents the temperature field at the core's mid-height ($y = 0.55\ m$). For both figures, aside from the additional gradients in the new regions, the rest of the contours remain mostly similar. Due to this, quantitative results are presented next.

To quantify the impact of the added volumes, Tab. 5.8 presents the volume-averaged temperature of SEALER's main regions for both the Full Loop and the CHT models. From this table, it is possible to infer that the inclusion of the new volumes, along with the CHT consideration, tends to equalize the temperatures, by lowering the temperature in the hot regions and increasing in the cold regions. The conduction of heat from the core directly

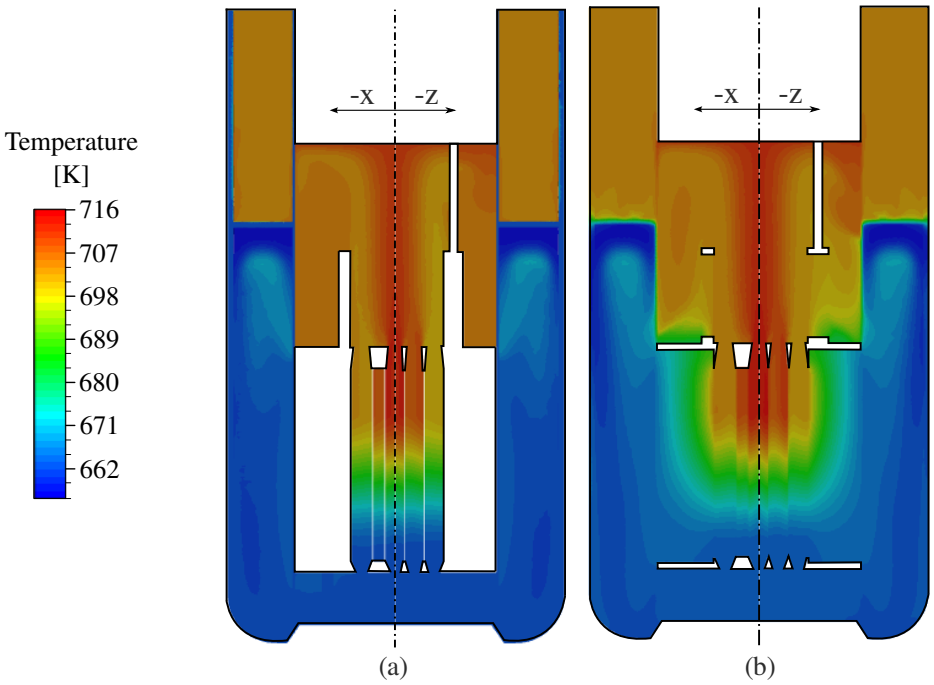

Figure 5.6: Longitudinal cross-section temperature field - (a) Adiabatic SEALER Full Loop and (b) SEALER CHT.

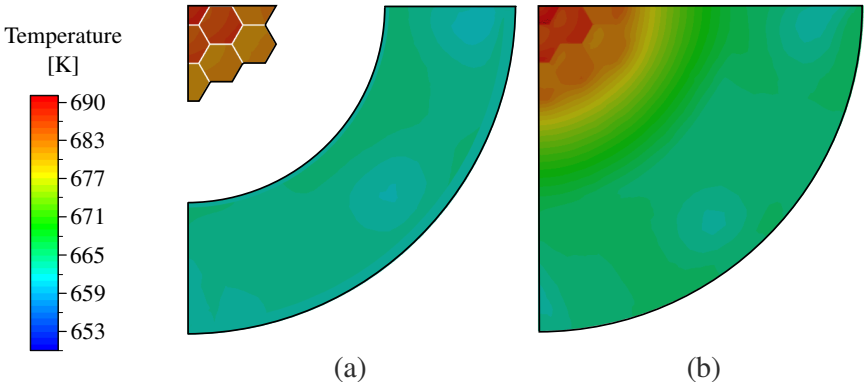

Figure 5.7: Core cross-section temperature field - (a) Adiabatic SEALER Full Loop and (b) SEALER CHT.

to the Cold Leg leads to the highest increase, which in turn, increases the Core's inlet temperature in the Cold Pool. However, since the Core's power remains the same, and there is now loss, the bulk temperature variation is not as high.

Table 5.8: Volume-averaged temperature comparison for the SEALER Full Loop and CHT with Adiabatic RV wall.

	SEALER Full Loop A	**SEALER CHT A**	**Difference**
Cold Leg $[K]$	663.74	664.98	+0.19%
Cold Pool $[K]$	662.92	663.84	+0.14%
Hot Leg $[K]$	704.82	703.11	-0.24%
Hot Pool $[K]$	703.79	703.49	-0.04%
Average $[K]$	681.76	682.08	+0.05%

The difference in the ΔT in the coolant's temperature rise is presented in Fig. 5.8, where the Core's average bulk temperature is plotted for both models, along with an absolute difference curve in the graph's secondary vertical axis.

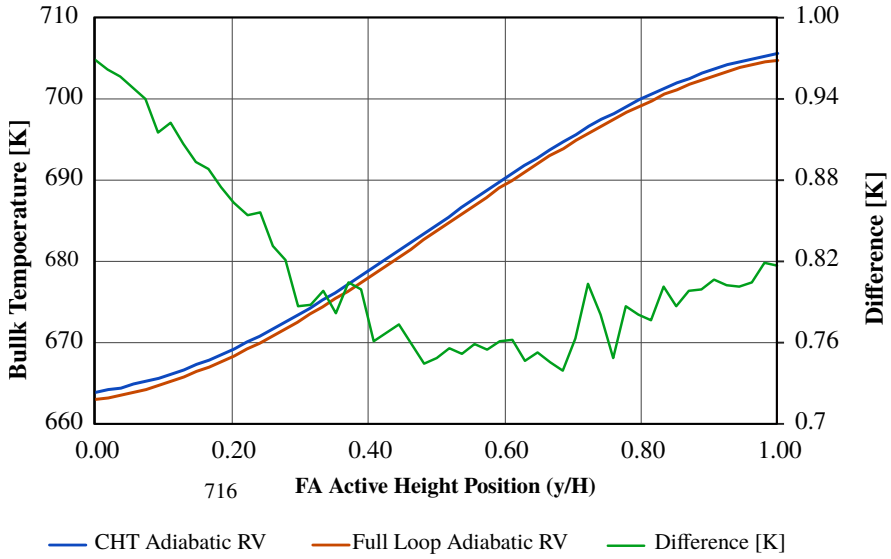

Figure 5.8: Core average bulk temperature versus axial position comparison - Adiabatic SEALER Full Loop and SEALER CHT A.

Although the absolute and relative differences are slight, not surpassing 1 K, both the Tab. 5.8 and Fig. 5.8 reinforce the understanding that there is an impact of the new volumes inclusion, however, they are most likely negligible.

5.3.2 Influence of the mixed radiation-convection BC

To assess the influence of varying the outer BCs, namely the adiabatic, radiation-only, and mixed radiation-convection, this Subsection compares the results of the CHT Adiabatic, R300K, and RC300K cases. The 300 K was chosen for being the coldest BC temperature, which should provide the most noticeable differences to understand the influence of each BC type.

Fig. 5.9 presents, in the form of a bar graph, the evaluated volume-averaged temperatures for each of the models in question. The largest differences observed are in the Hot Pool region, where the energy is lost from both the upper free surface and the RV. Tab. 5.9 presents these temperature values and their absolute difference in comparison with the adiabatic model.

For both the R300K and the RC300K, the greatest variation is in the Hot Pool region, with -7.88 K and -10.44 K respectively. Despite the significant variation, these values are volume-averaged. Fig. 5.10 and Fig. 5.11 present plots for temperature along the lines Y550X and Y3100Z respectively. In both cases, the sharpest drops in temperatures

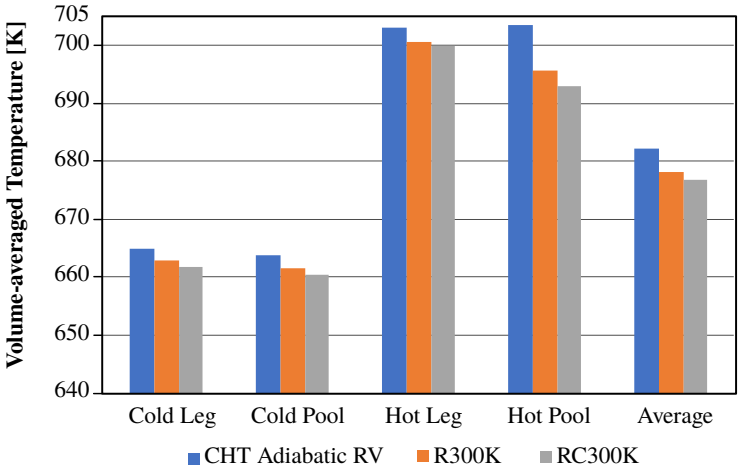

Figure 5.9: Influence of the R and RC conditions, compared with the A condition.

Table 5.9: Influence of the outer BC on the volume-averaged temperature of the main regions.

	CHT Adiabatic	**R300K**		**RC300K**	
	Temp. [K]	**Temp. [K]**	**Δ T [K]**	**Temp. [K]**	**Δ T [K]**
Cold Leg	664.98	662.81	−2.17	661.84	−3.14
Cold Pool	663.84	661.45	−2.39	660.31	−3.53
Hot Leg	703.11	700.58	−2.54	699.82	−3.29
Hot Pool	703.49	695.61	−7.88	693.05	−10.44
Average	682.08	678.20	−3.88	676.80	−5.28

are observed in the regions close to the RV wall. For the adiabatic case, the curves are horizontal, indicating that the zero-gradient value is respected.

The greater difference observed in the near-wall temperature drop in Fig. 5.11 is due to the curve ending in the Hot Pool, while Fig. 5.10 ends in the Cold Leg. Nonetheless, the RC300K model resulted in a drop $\sim 10\ K$ lower than the R300K, and in turn, $\sim 20\ K$ colder than the adiabatic model. For some additional information, the total heat transfer rate on the RV for the RC300K case is 73.8 kW, which is short of 1% of the total power generated in the core. Closer to the Core's center line ($y/H = 0$), the temperature difference is more subtle, around 5 K at most. A more detailed fuel comparison will be presented later in this section.

The results presented above show that the additional thermal BC on the RV wall impact significantly the average temperatures in the reactor regions, and mostly around the near-wall regions. Thus, it should be a consideration to be made when CFD modeling, whenever a more detailed understanding of the temperature fields should be required.

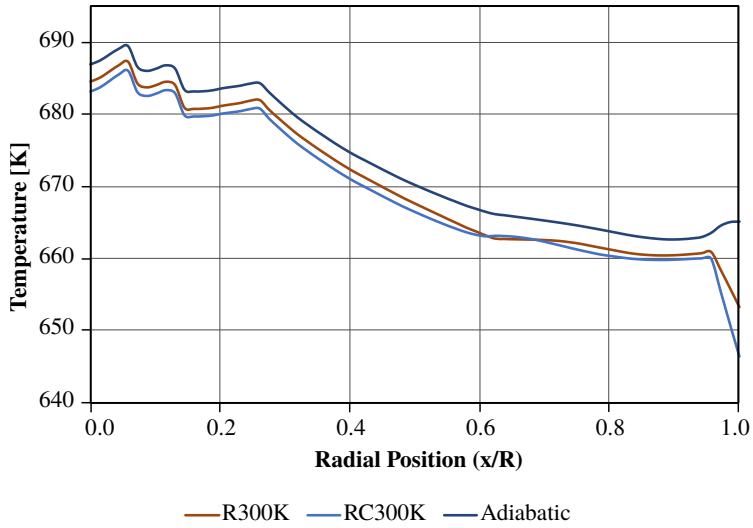

Figure 5.10: Temperature at Y=0.55 m along X comparison for the Adiabatic, R300K, and RC300K BCs.

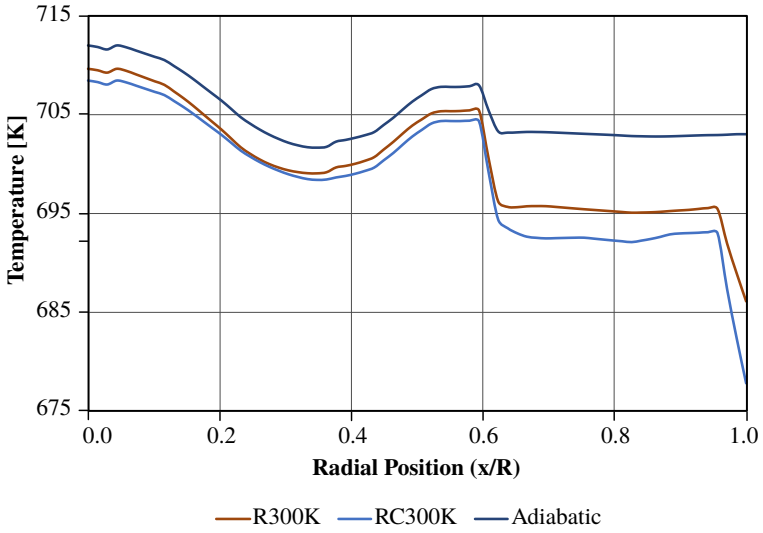

Figure 5.11: Temperature at Y=3.1 m along Z comparison for the Adiabatic, R300K, and RC300K BCs.

5.3.3 Influence of outside reference temperatures

Given the importance of the mixed radiation-convection BC on the outer RV wall, this subsection presents results for the influence of varying the radiation outer temperatures, as per Tab. 5.2, and the natural convection coefficients, per Tab. 5.4.

Fig. 5.12 presents the volume-averaged temperatures for SEALER's main regions. The progression from the colder RC300K to the hotter RC550K is physically coherent, however, the absolute differences are slight, not surpassing 5 K.

Taking a similar approach to the previous subsection analysis, Fig. 5.13 includes the other RC cases. The curves are all close in shape and value, in accordance with the volume-averaged values in Fig. 5.12, nevertheless, they diverge in the RV region, where the RC BC evidently has more impact.

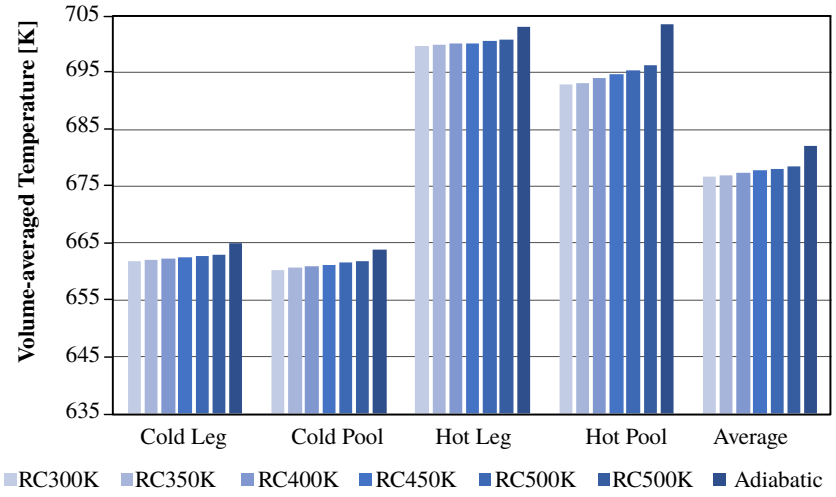

Figure 5.12: Influence of the outside temperature variation on the volume-averaged temperatures of the SEALER regions.

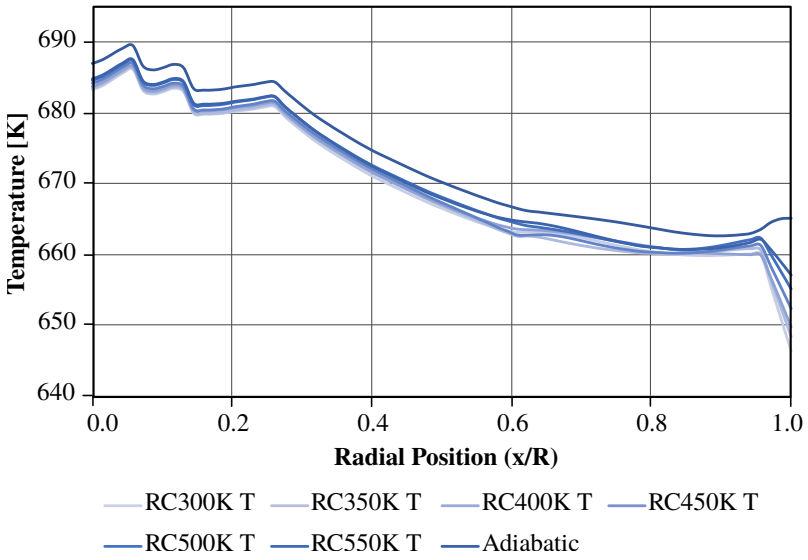

Figure 5.13: Temperature at Y=0.55 m along X comparison for different RC values.

Fig. 5.14 presents the temperature contours at the YZ plane for the RC300K, RC550K, and Adiabatic cases. It is possible to observe the colder temperatures close to the RV wall, for the RC300K, and a hotter Hot Pool for the Adiabatic case.

Tab. 5.10 explores the area-averaged temperature on the RV's outer wall. Although the relative differences, when compared to the Adiabatic case, are lower than 4%, the absolute values can reach close to 24 K, for the RC300K.

Fig. 5.15 presents the mid-core cross-section temperature contours for the RC300K, RC550K, and Adiabatic cases. In this figure, the temperature gradient close to the RV wall is more distinguishable, in accordance with the quantitative values presented in Tab. 5.10.

Although the temperature variation in the RC has an impact on the extremities of the domain, it can be observed that this impact is smaller as the temperature is measured

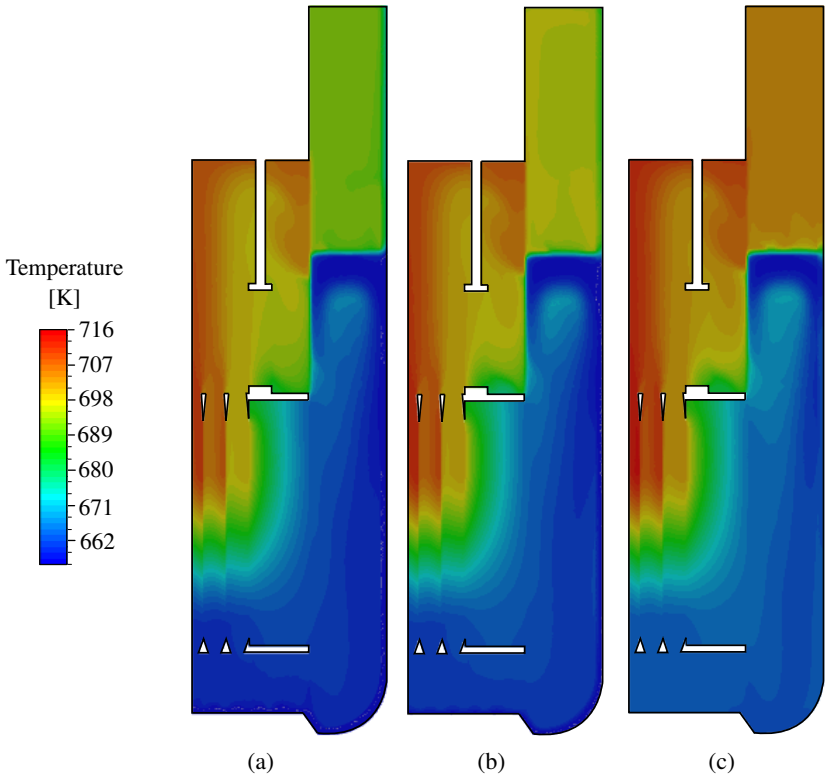

Figure 5.14: Temperature contours at the YZ plane for (a) RC300K, (b) RC550K, and (c) Adiabatic.

Table 5.10: RV Wall surface-averaged temperature comparison

	RV Wall Avg. Temp.[K]	**Δ T [K]**	**Difference**
Adiabatic	676.13	-	-
RC550K	664.77	-11.36	-1.68%
RC500K	662.08	-14.05	-2.08%
RC450K	659.55	-16.58	-2.45%
RC400K	657.15	-18.98	-2.81%
RC350K	654.96	-21.17	-3.13%
RC300K	652.78	-23.35	-3.45%

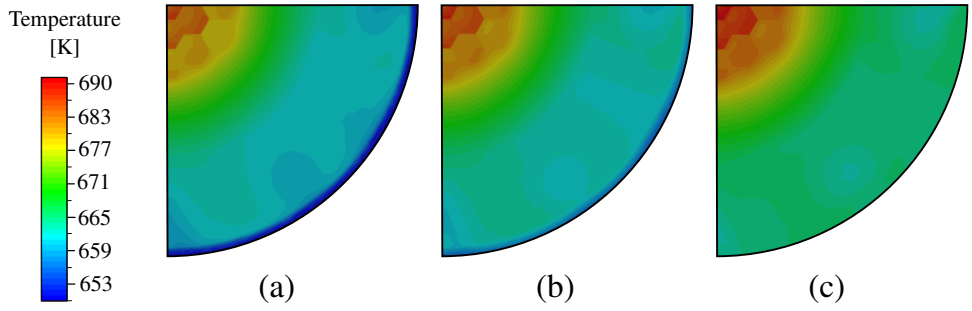

Figure 5.15: Temperature contours at Y=0.55 m for (a) RC300K,(b) RC550K, and (c) Adiabatic.

closer to the radial center, namely in the Central FA of the Core. Fig. 5.16 presents the Central FA bulk temperature for each RC case. Close temperature measurements for all cases are present throughout the entire length of the core. Upon closer examination of the

upper limit of the active height, it is observable a maximum difference of 4 K between the RC300K and Adiabatic scenarios.

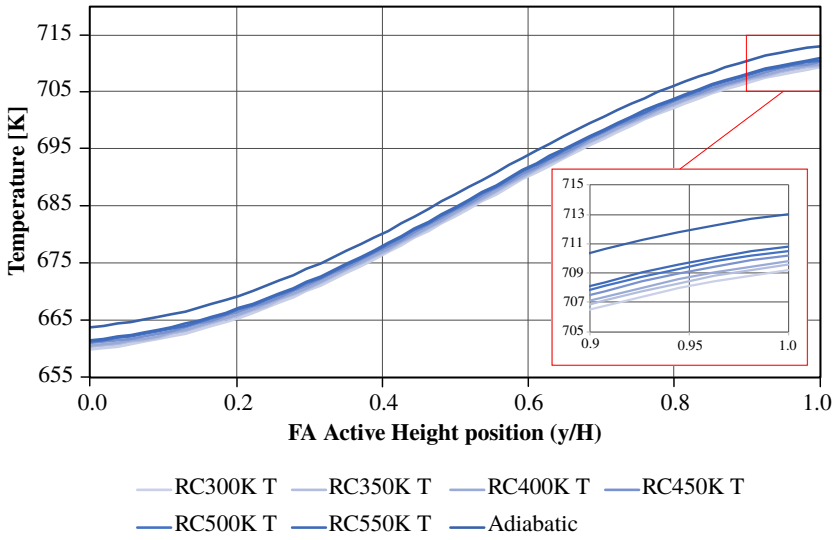

Figure 5.16: Central FA bulk temperature comparison for different RC values.

This behavior leads to the understanding that varying the outer temperature in the different RC cases has little impact on the core region, even though the disparities on the RV wall are considerable, and proportional to the BC temperature.

5.3.4 Fuel temperature analysis

Following the established approach for calculating fuel temperature, this subsection presents a comparative analysis of the fuel temperature across various RC boundary conditions. It is relevant to note that these findings are solely intended for comparative reasons and for the goal of offering a methodology for determining fuel temperature. Nevertheless, even little fluctuations in certain constants, such as cladding or fuel conductivity, gap conductance, and so on, can result in temperature variations of a few Kelvin. Furthermore, the incorporation of neutronic computations was not considered.

For the purpose of evaluating the influence of the RC BC variation on the reactor's behavior, only the Central FA results are used in the comparison, given its higher temperatures and relevance for nuclear safety matters.

Fig. 5.17 presents the temperature curves for the RC300K case, coming from the bulk temperature (obtained from the CFD results), to the clad outer, clad inner, fuel outer, and ultimately, the fuel center-line (CL) temperatures. Fig. 5.18 leaves out the fuel CL and zooms on the cladding temperature values. All curves are physically coherent regarding shape and value magnitude.

Fig. 5.19 presents the comparison, between the adiabatic and all RC cases, for

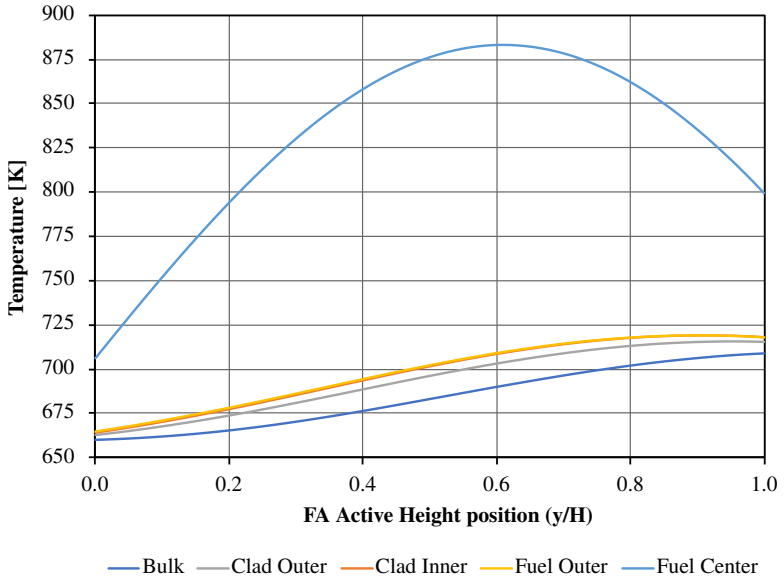

Figure 5.17: Central Assembly RC300K - Fuel pin temperatures.

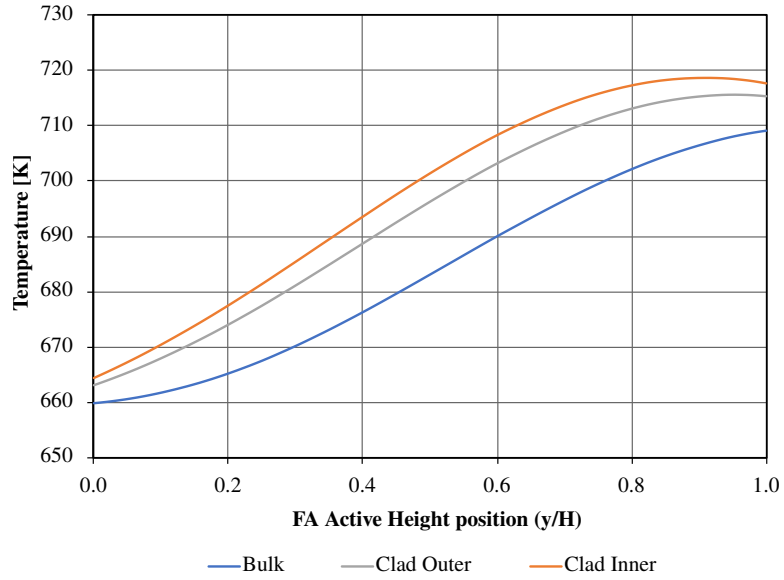

Figure 5.18: Central Assembly RC300K - Clad temperatures.

the Central FA Fuel CL temperature, with a magnification detail around the peak values. Following the behavior shown in all the previous temperature curve comparisons, the gaps from RC300K to RC500K are mostly proportional to the RC temperatures themselves, and then there is a larger jump to the Adiabatic case.

The maximum difference of 4 K does not suggest any significant impact, in terms of fuel safety, considering that normal operation oscillations in temperature could be greater than 4 K. In any case, the results for maximum fuel and cladding temperature are within the order of magnitude expected in the original design [23] of around 918 K and 709 K

respectively.

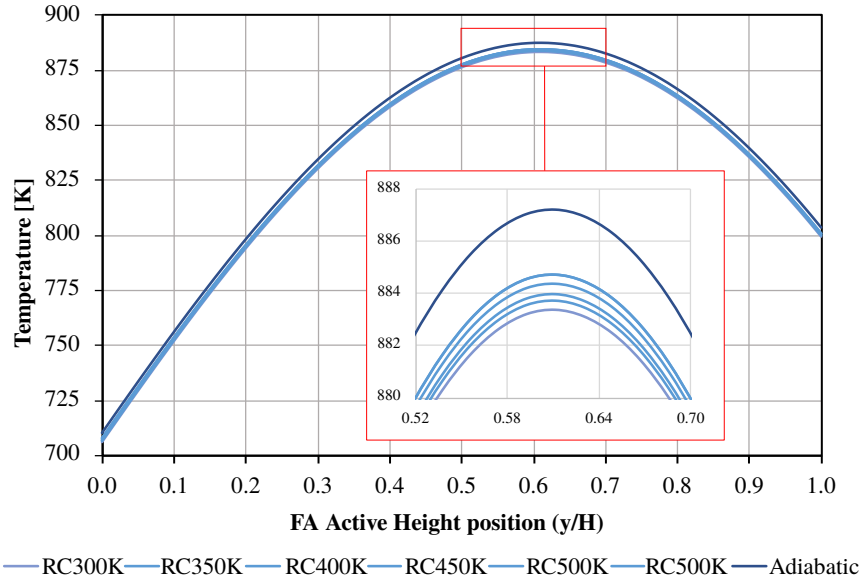

Figure 5.19: Fuel CL temperature comparison.

5.4 Partial Conclusions

In this Chapter, the SEALER model was expanded to account for new volume regions and additional thermal considerations, namely the CHT between fluids and solids and the mixed radiation and convection outer BC. From these modifications, the results were mainly comparative and focused on the temperature field variations.

The inclusion of the outer core region, modeled as a solid for conduction, allowed for a clear visualization of the temperature field as heat flows from the active core regions to the Cold Pool. By comparing with the last Chapter's model, it was possible to observe that this heat flow impacts very slightly the volume-averaged temperature values in all SEALER's main regions.

The variation of the RC BC from the RC300K to the RC550K allowed the verification that the models behave proportionally to their reference temperature, but with close enough results to infer that the RC temperature range is within an asymptotic value region. That is, if colder temperatures were evaluated, greater differences could be observed. However, the coldest 300 K was understood as the room-temperature reference for natural cooling.

Although there is a maximum temperature difference of 250 K between both extreme cases, the comparison results indicate that departing from the RV close-wall region to the core's center, the difference in local temperature tends to diminish rapidly, as shown in the fuel temperature analysis comparison. Nonetheless, values for surface temperature

did show some absolute differences, above 20 K.

From the CFD results for the FAs coolant bulk temperature, the cladding and fuel temperature values could be obtained using analytical approaches. The values, magnitudes, and curve shapes were considered to be reasonable and, thus, acceptable for the intent of straight comparison. This comparative analysis indicated that the outer RC BC temperature variation had minimal impact on the fuel temperature, as the maximum difference did not surpass around 4 K.

Although this parameter variation study did not indicate significant differences between the RC300K and the RC550K, when they are compared to the Adiabatic case, absolute differences could indeed be noticed. This leads to the conclusion that considering mixed BC brings non-negligible contributions to modeling systems such as SEALER, especially when the understanding of its thermal behavior is still in development.

As for the inclusion of the new conduction regions, although the differences were also slight, the RC studies would not be possible without them. Additionally, the Author suggests that the heat capacity of these regions could have greater contributions in a transient simulation where the core temperature is varied rapidly (e.g.: UTOP or ULOF situations), with energy still contained in these volumes, it could balance the temperature in the other main regions.

Chapter 6

Conclusions

This final Chapter presents the conclusions drawn from this Dissertation, followed by a list of derived publications and presentations from this Master's studies period, and some recommendations for future work.

6.1 Conclusions from this Dissertation

In this Dissertation, several CFD modeling approaches were incrementally combined to reach the general goal of simulating a Small Modular Lead-cooled Fast Reactor, the SEALER Arctic. Conclusively, this goal was indeed achieved, with a significant side of computational efficiency, given that choices ranging from the mesh size to the pump model, resulted in an average of 64 core-hours of calculation (steady and transient) for each case.

In Chapter 3, the simulation domain was limited to the Core Barrel region and focused on specific core modeling strategies, such as the Porous Media and Porous Jumps to simulate the pressure drop along the fuel assemblies, and the position-dependent thermal power functions applied to the active regions. Additionally, CFD solving schemes, the appropriate mesh size, and the turbulence model were explored and defined for use in the following Chapters. Ultimately, Chapter 3 presented that the used FA porous models combined with the power functions were adequate to represent the Core steady behavior, given that the coolant's temperature rise matched the original design data, as well as the velocity magnitude field within the Core Barrel region.

Chapter 4 expanded the simulation domain to account for the Hot Pool and Cold Leg regions, thus closing the primary loop. The recirculation pumps and steam generators (SGs) were included in the full loop model to add the new regions and to remove the simplified inlet and outlet boundary conditions in the isolated Core Barrel. The pumps

were modeled using a constant mass flow rate interface, the SGs employed a combination of porous media (two methods were compared) with a temperature-dependent heat sink model calibrated for the designed SEALER loop temperature drop. This expanded model was primarily intended to demonstrate the possibility of modeling the hydraulic loop of a small pool-type LFR, so no additional thermal conditions were considered, besides the Core-SG-Core heating and cooling cycle. Chapter 4's main results presented that the full primary loop was successfully calibrated to simulate steady condition operation, with a stabilized thermal and velocity field within the reactor, and that a combination of symmetry and rotational periodic boundary conditions was adequate for the expanded domain.

Chapter 5 was the last model expansion, in which some further thermal considerations were made to the full primary loop model. The main domain modification was in the inclusion of regions through which heat could be transferred by conduction, namely the Core's outside assemblies and the control rod's extensions. Both were modeled as solid lead but with the same temperature-dependent thermophysical properties as the fluids, since the flow velocity is mostly stagnant in those regions, and only heat conduction was accounted for. The Conjugate Heat Transfer condition was also considered in this Chapter so that energy flow could be observed between FAs and from hot to cold volumes. Thus, a brief study of parameter variation was carried out on the Reactor Vessel's outer surface, by evaluating different combinations of natural convection and radiation heat loss boundary conditions. The main result of this Chapter indicated that the thermal effects considered indeed influence the system's temperature fields, especially when comparing the adiabatic condition with any other radiation and convection BC case, leading to average temperature differences of as much as 20 K on the RV outer surface. Additional analytical calculations were made to understand these impacts on fuel temperature and maximum differences of around 4 K were observed at the peak of the center lines. Finally, Chapter 5 showed that additional thermal considerations are relevant and should be used whenever possible, for more accurate simulation results for temperature.

6.2 Fruits from this Master's studies and Dissertation

This work raised considerably interesting findings regarding thermal considerations in CFD modeling of small pool-type LFRs and also presented detailed descriptions of the various methods employed, all without completely innovative approaches or technical complexity. The thorough illustration of the modeling methods studied should be, in the Author's opinion, the most relevant for now, since very little information is so openly

available for these types of simulations.

The period taken to develop this Master's Dissertation can be considered challenging but fruitful. Around 250 different CFD cases were prepared and many more simulations were run, ranging from the most basic local geometry tests to the complete SEALER models presented earlier. Ultimately, this evolving effort led to some works presented at conferences, events, and workshops, and also a couple of articles published in journals and proceedings. Listed below are the works derived from this Master's and Dissertation:

Journal Papers

- I. K. Umezu, A. L. Costa, D. M. Godino, and A. A. C. Santos. CFD analysis of a wire-wrapped infinite sub-channel using temperature-dependent LBE properties. Brazilian Journal of Radiation Sciences, 10(3A), October 2022. ISSN 2319-0612. doi: 10.15392/2319-0612.2022.1949.[87].

- C. A. M. da Silva, N. G. L. Oliveira, I. K. Umezu, A. L. Costa, and C. Pereira. Neutronic evaluation of a small lead-cooled nuclear reactor as an actinides burner. Nuclear Engineering and Design, vol. 417, 112796, ISSN 0029-5493, doi.org/10.1016/j.nucengdes.2023.112796. [99].

Conference Proceedings

- I. K. Umezu, D. M. Godino, D. E. Ramajo, C. Pereira, C. A. M. Silva, and A. L. Costa. RECIRCULATING FLOW ANALYSES IN A LEAD-COOLED SMALL MODULAR REACTOR. In Anais da Semana Nacional de Engenharia Nuclear e da Energia e Ciências das Radiações, Belo Horizonte, Minas Gerais, 2023. Even3. ISBN 978-85-5722-483-4. doi: 10.29327/VI SENCIR.560069.

Presentations

- I. K. Umezu, J. C. Silva, A. L. Costa, C. E. Velasquez, and C. Pereira. ADS LBE spallation target design: A review on geometrical influences on neutronic and thermal behavior. International Nuclear Atlantic Conference - INAC 2021, Rio de Janeiro, Brazil, December 2021.

- I. K. Umezu, A. L. Costa, and A. A. C. Santos. CFD analysis of an infinite wire-wrapped LBE-cooled fast reactor sub-channel. International Nuclear Atlantic Conference - INAC 2021, Rio de Janeiro, Brazil, December 2021.

- I. K. Umezu, D. M. Godino, C. E. Velasquez, A.L. Costa, and C. Pereira. Homogenized Fuel Assembly CFD Modelling: A Comparison of Coolant Temperature Fields with a Porous Media Model. Joint ICTP-IAEA Advanced School/Workshop on Computational Nuclear Science and Engineering, Trieste, Italy, May 2022.

- I. K. Umezu, D. M. Godino, D.E. Ramajo, C. Pereira, and A. L. Costa. Simulación CFD del Núcleo de un Pequeño Reactor Modular Refrigerado por Plomo, MECOM 2022, Bahía Blanca, Argentina, November 2022.

- I. K. Umezu, D. M. Godino, D.E. Ramajo, C. Pereira, C. A. M. Silva, and A. L. Costa. RECIRCULATING FLOW ANALYSES IN A LEAD-COOLED SMALL MODULAR REACTOR. Semana Nacional de Engenharia Nuclear e da Energia e Ciências das Radiações - SENCIR VI, Belo Horizonte, Brazil, November 2022.

- I. K. Umezu, D. M. Godino, D.E. Ramajo, and C. Pereira. POROUS MEDIA IN CFD MODELLING FOR SIMULATING COOLANT FLOW BEHAVIORS IN A LEAD-COOLED SMR, Joint ICTP-IAEA Workshop on Physics and Technology of Innovative Nuclear Energy Systems, Trieste, Italy, December 2022.

- I. K. Umezu, D. M. Godino, D.E. Ramajo, C. Pereira, and A. L. Costa. DESARROLLO DE UNA METODOLOGÍA CFD PARA SIMULAR UN PEQUEÑO REACTOR MODULAR REFRIGERADO POR PLOMO, MECOM 2023, Concordia, Argentina and Salto, Uruguay, November 2023.

6.3 Future work recommendations

Advancements departing from what was developed so far should be focused on both applicability for safety analyses and technical aspects. The main recommendations for future work are listed below, in no particular order:

- Extension of the simulated time of operation. This work employed transient simulations of 10 s of operation, just for result stabilization. Future works could experiment with longer simulations (in hundreds of seconds) to observe time-dependent behavior, even under steady assumptions;

- Experimentation with different cooling fluids on the outer surface of the reactor vessel. Water, for example, was considered but not explored due to the possibility of boiling (because of the RV surface temperatures hotter than 100 $°C$), under atmospheric

pressure. Other fluids were not also explored due to a lack of definitive information on this boundary condition (temperature, type of circulation, containment size, etc.).

- Employment of two-phase (liquid lead and gas) models, to account for free-surface level variations on the Hot Leg and Hot Pool during transient situations;
- Experimentation with transient cases, such as start-up, loss of power accidents, FA blockage, etc. Using time-dependent pump functions for mass flow rate control (inertial deceleration), and porous media permeability variation in the FAs;
- Validation of the SG functions developed, by comparing with experimental results, if ever available;
- Update of the Turbulent Prandtl number used on the models. Research on this topic has been ever-evolving, as in the recent work of [50], where a $Pr_t = 1.5$ is recommended for better predictions of local temperature distributions and global Nusselt number, against the $Pr_t = 2.0$ used in this work. Although the simulations carried out in this work are more globally and bulk-oriented, this modification is worth investigating;
- Inclusion of the Core's outer assemblies, i.e.: control, shielding, and reflector assemblies, with their respective calculated porous media coefficients, to observe how differently the velocity and temperature fields behave. It should be expected harder simulation convergence, especially for the velocity and continuity residuals, given the coolant's density variations within slow-moving regions;
- Development of the CAD model and meshing strategies to allow the complete interface between the suppressed regions in Chapter 5; and
- Comparison of the obtained results with other thermal-hydraulic analysis tools, such as RELAP5 3D.

References

[1] U. Nations, "The Paris Agreement," 2015.

[2] IAEA, "Nuclear Energy for a Net Zero World," tech. rep., IAEA, Vienna, Austria, 2021.

[3] IPCC, *Global Warming of 1.5°C: IPCC Special Report on Impacts of Global Warming of 1.5°C above Pre-industrial Levels in Context of Strengthening Response to Climate Change, Sustainable Development, and Efforts to Eradicate Poverty*. Cambridge University Press, 1 ed., June 2022.

[4] IEA, "Net Zero by 2050 - A Roadmap for the Global Energy Sector," tech. rep., IEA, 2021.

[5] IAEA, "Energy, Electricity and Nuclear Power Estimates for the Period up to 2050," Tech. Rep. RDS-1/42, IAEA, Vienna, Austria, 2022.

[6] M. Carelli, P. Garrone, G. Locatelli, M. Mancini, C. Mycoff, P. Trucco, and M. Ricotti, "Economic features of integral, modular, small-to-medium size reactors," *Progress in Nuclear Energy*, vol. 52, pp. 403–414, May 2010.

[7] IAEA, "Technology roadmap for small modular reactor deployment," Tech. Rep. NR-T-1.18, IAEA, Vienna, Austria, 2021.

[8] GIF, "GIF Annual Report 2021," tech. rep., Generation IV International Forum, 2021.

[9] OECD - Nuclear Energy Agency, *Handbook on Lead-bismuth Eutectic Alloy and Lead Properties, Materials Compatibility, Thermalhydraulics and Technologies*. Nuclear Science, OECD, Nov. 2015.

[10] I. ANSYS, *ANSYS Fluent Theory Guide*. ANSYS, Inc., 2019.

[11] I. ANSYS, *Fluent User's Guide*. ANSYS, Inc., 2019.

[12] I. Pioro, *HANDBOOK OF GENERATION IV NUCLEAR REACTORS*. Woodhead Publishing Series in Energy, S.l.: WOODHEAD PUBLISHING, 2 ed., 2023. OCLC: 1354993283.

[13] M. Frogheri, A. Alemberti, and L. Mansani, "THE ADVANCED LEAD FAST REACTOR EUROPEAN DEMONSTRATOR (ALFRED)," in *NURETH-15 Proceedings*, 2013.

[14] A. Alemberti, M. Caramello, M. Frignani, G. Grasso, F. Merli, G. Morresi, and M. Tarantino, "ALFRED reactor coolant system design," *Nuclear Engineering and Design*, vol. 370, p. 110884, Dec. 2020.

[15] E. O. Adamov, A. V. Kaplienko, V. V. Orlov, V. S. Smirnov, A. V. Lopatkin, V. V. Lemekhov, and A. V. Moiseev, "Brest Lead-Cooled Fast Reactor: From Concept to Technological Implementation," *Atomic Energy*, vol. 129, pp. 179–187, Feb. 2021.

[16] A. G. Glazov, V. N. Leonov, V. V. Orlov, A. G. Sila-Novitskii, V. S. Smirnov, A. I. Filin, and V. S. Tsikunov, "Brest reactor and plant-site nuclear fuel cycle," *Atomic Energy*, vol. 103, pp. 501–508, July 2007.

[17] A. Zrodnikov, G. Toshinsky, O. Komlev, V. Stepanov, and N. Klimov, "SVBR-100 module-type fast reactor of the IV generation for regional power industry," *Journal of Nuclear Materials*, vol. 415, pp. 237–244, Aug. 2011.

[18] J. Wallenius, E. Suvdantsetseg, and A. Fokau, "ELECTRA: European Lead-Cooled Training Reactor," *Nuclear Technology*, vol. 177, pp. 303–313, Mar. 2012.

[19] J. Wallenius, E. Suvdantsetseg, S. Bortot, M. Pukari, M. Jolkkonen, A. Claisse, P. Olsson, J. Ejenstam, and P. Szakalos, "ELECTRA: A LEAD COOLED REACTOR FOR TRAINING AND EDUCATION," *PROBLEMS OF ATOMIC SCIENCE AND TECHNOLOGY.*, vol. 4, 2015.

[20] H. A. Abderrahim and P. D'Hondt, "MYRRHA: A European Experimental ADS for R&D Applications Status at Mid-2005 and Prospective towards Implementation," *Journal of Nuclear Science and Technology*, vol. 44, pp. 491–498, Mar. 2007.

[21] H. A. Abderrahim, D. de Bruyn, M. Dierckx, R. Fernandez, and L. P. Popescu, "MYRRHA accelerator driven system programme: recent progress and perspectives," *Izvestiya Wysshikh Uchebnykh Zawedeniy, Yadernaya Energetika*, vol. 2019, pp. 29–42, June 2019.

[22] C. F. Smith, W. G. Halsey, N. W. Brown, J. J. Sienicki, A. Moisseytsev, and D. C. Wade, "SSTAR: The US lead-cooled fast reactor (LFR)," *Journal of Nuclear Materials*, vol. 376, pp. 255–259, June 2008.

[23] J. Wallenius, S. Qvist, I. Mickus, S. Bortot, P. Szakalos, and J. Ejenstam, "Design of SEALER, a very small lead-cooled reactor for commercial power production in off-grid applications," *Nuclear Engineering and Design*, vol. 338, pp. 23–33, Nov. 2018.

[24] IAEA, *Benefits and challenges of small modular fast reactors: proceedings of a technical meeting. IAEA Tecdoc series - 1972.* Vienna, Austria: International Atomic Energy Agency, 2021. OCLC: 1273673965.

[25] S. Choi, I. S. Hwang, J. H. Cho, and C. B. Shim, "URANUS: Korean Lead-Bismuth Cooled Small Modular Fast Reactor Activities," in *ASME 2011 Small Modular Reactors Symposium*, (Washington, DC, USA), pp. 107–112, ASMEDC, Jan. 2011.

[26] Y. Wu, "CLEAR-S: an integrated non-nuclear test facility for China lead-based research reactor," *INTERNATIONAL JOURNAL OF ENERGY RESEARCH*, vol. 40, pp. 1951–1956, 2016.

[27] J. Liao and D. Utley, "Study on Reactor Vessel Air Cooling for Westinghouse Lead Fast Reactor," *Nuclear Technology*, vol. 206, pp. 191–205, Feb. 2020.

[28] J. Liao, P. Ferroni, R. F. Wright, U. Bachrach, J. H. Scobel, T. Sofu, A. M. Tentner, S. J. Lee, M. Epstein, M. Frignani, and M. Tarantino, "Development of phenomena identification and ranking table for Westinghouse lead fast reactor's safety," *Progress in Nuclear Energy*, vol. 131, p. 103577, Jan. 2021.

[29] S. J. Lee, J. Liao, R. F. Wright, and P. Ferroni, "Preliminary assessment of the safety performance of Westinghouse LFR," *Nuclear Engineering and Design*, vol. 411, 2023.

[30] M. Rawool-Sullivan, P. D. Moskowitz, and L. N. Shelenkova, "Technical and proliferation-related aspects of the dismantlement of Russian Alfa-Class nuclear submarines," *The Nonproliferation Review*, vol. 9, pp. 161–171, Mar. 2002.

[31] G. Thamm, "The ALFA SSN: Challenging Paradigms, Finding New Truths, 1969–79," *Studies in Intelligence*, vol. 52, 2007.

[32] A. E. Waltar, D. R. Todd, and P. V. Tsvetkov, eds., *Fast Spectrum Reactors*. Boston, MA: Springer US, 2012.

[33] A. Alemberti, V. Smirnov, C. F. Smith, and M. Takahashi, "Overview of lead-cooled fast reactor activities," *Progress in Nuclear Energy*, vol. 77, pp. 300–307, Nov. 2014.

[34] M. Bugreev, E. Efimov, S. Ignatiev, D. Pankratov, and V. Tchitaykin, "Assessment of Spent Fuel of Alfa Class Nuclear Submarines," *MRS Proceedings*, vol. 713, p. JJ11.61, 2002.

[35] G. I. Toshinsky, A. V. Dedul, O. G. Komlev, A. V. Kondaurov, and V. V. Petrochenko, "Lead-Bismuth and Lead as Coolants for Fast Reactors," *World Journal of Nuclear Science and Technology*, vol. 10, no. 02, pp. 65–75, 2020.

[36] J.-B. Vogt and I. Proriol Serre, "A Review of the Surface Modifications for Corrosion Mitigation of Steels in Lead and LBE," *Coatings*, vol. 11, p. 53, Jan. 2021.

[37] W. Wang, C. Yang, Y. You, and H. Yin, "A Review of Corrosion Behavior of Structural Steel in Liquid Lead–Bismuth Eutectic," *Crystals*, vol. 13, p. 968, June 2023.

[38] J. Zhang, "A review of steel corrosion by liquid lead and lead–bismuth," *Corrosion Science*, vol. 51, pp. 1207–1227, June 2009.

[39] J. Ejenstam and P. Szakálos, "Long term corrosion resistance of alumina forming austenitic stainless steels in liquid lead," *Journal of Nuclear Materials*, vol. 461, pp. 164–170, June 2015.

[40] V. Sobolev, "Thermophysical properties of lead and lead–bismuth eutectic," *Journal of Nuclear Materials*, vol. 362, pp. 235–247, May 2007.

[41] H. K. Versteeg and W. Malalasekera, *An introduction to computational fluid dynamics: the finite volume method*. Harlow: Pearson/Prentice Hall, 2. ed., [nachdr.] ed., 2007.

[42] T.-H. Shih, W. W. Liou, A. Shabbir, Z. Yang, and J. Zhu, "A new k-epsilon eddy viscosity model for high Reynolds number turbulent flows," *Computers & Fluids*, vol. 24, pp. 227–238, Mar. 1995.

[43] B. Launder and D. Spalding, "The numerical computation of turbulent flows," *Computer Methods in Applied Mechanics and Engineering*, vol. 3, pp. 269–289, Mar. 1974.

[44] J. H. Ferziger and M. Peric, *Computational Methods for Fluid Dynamics*. Springer-Verlag, 3 ed., 2002.

[45] D. D. Gray and A. Giorgini, "The validity of the boussinesq approximation for liquids and gases," *International Journal of Heat and Mass Transfer*, vol. 19, pp. 545–551, May 1976.

[46] W. Ni, S. Qiu, G. Su, W. Tian, and Y. Wu, "Numerical investigation of buoyant effect on flow and heat transfer of Lithium–Lead Eutectic in DFLL–TBM," *Progress in Nuclear Energy*,

vol. 58, pp. 108–115, July 2012.

[47] A. Barletta, M. Celli, and D. A. S. Rees, "On the Use and Misuse of the Oberbeck–Boussinesq Approximation," *Physics*, vol. 5, pp. 298–309, Mar. 2023.

[48] A. Mohamad and R. Viskanta, "Modeling of turbulent buoyant flow and heat transfer in liquid metals," *International Journal of Heat and Mass Transfer*, vol. 36, pp. 2815–2826, July 1993.

[49] J. Pacio, T. Wetzel, H. Doolaard, F. Roelofs, and K. Van Tichelen, "Thermal-hydraulic study of the LBE-cooled fuel assembly in the MYRRHA reactor: Experiments and simulations," *Nuclear Engineering and Design*, vol. 312, pp. 327–337, Feb. 2017.

[50] Y. Yu, E. Shemon, and E. Merzari, "LES simulation on heavy liquid metal flow in a bare rod bundle for assessment of turbulent Prandtl number," *Nuclear Engineering and Design*, vol. 404, p. 112175, Apr. 2023.

[51] M. Duponcheel, L. Bricteux, M. Manconi, G. Winckelmans, and Y. Bartosiewicz, "Assessment of RANS and improved near-wall modeling for forced convection at low Prandtl numbers based on LES up to Ret= 2000," *International Journal of Heat and Mass Transfer*, vol. 75, pp. 470–482, Aug. 2014.

[52] E. Merzari, F.-B. Cheung, S. M. Bajorek, and Y. Hassan, "40th Anniversary of the first international topical meeting on nuclear reactor thermal-hydraulics: Highlights of thermal-hydraulics research in the past four decades," *Nuclear Engineering and Design*, vol. 373, p. 110965, Mar. 2021.

[53] E. Merzari, H. Yuan, A. Kraus, A. Obabko, P. Fischer, J. Solberg, S. Lee, J. Lai, M. Delgado, and Y. Hassan, "High-Fidelity Simulation of Flow-Induced Vibrations in Helical Steam Generators for Small Modular Reactors," *Nuclear Technology*, vol. 205, pp. 33–47, Jan. 2019.

[54] C. Fiorina, K. Mikityuk, and A. Pautz, "GeN-Foam: a novel multi-physics solver for reactor analysis – Status and ongoing developments," in *Transactions of the American Nuclear Society*, (Washington, D.C.), Nov. 2015.

[55] C. Fiorina, I. Clifford, M. Aufiero, and K. Mikityuk, "GeN-Foam: a novel OpenFOAM® based multi-physics solver for 2D/3D transient analysis of nuclear reactors," *Nuclear Engineering and Design*, vol. 294, pp. 24–37, Dec. 2015.

[56] F. Roelofs, *Thermal Hydraulics Aspects of Liquid Metal Cooled Nuclear Reactors*. Woodhead Publishing, 2019.

[57] F. Roelofs, D. Dovizio, H. Uitslag-Doolaard, D. De Santis, A. Mathur, B. Mikuz, and A. Shams, "Core thermal hydraulic CFD support for liquid metal reactors," *Nuclear Engineering and Design*, vol. 355, p. 110322, Dec. 2019.

[58] L. Koloszar, P. Planquart, K. Van Tichelen, and S. Keijers, "Numerical simulation of Loss-of-Flow transient in the MYRRHA reactor," *Nuclear Engineering and Design*, vol. 363, p. 110675, July 2020.

[59] K. Van Tichelen, G. Kennedy, F. Mirelli, A. Marino, A. Toti, D. Rozzia, E. Cascioli, S. Keijers, and P. Planquart, "Advanced Liquid-Metal Thermal-Hydraulic Research for MYRRHA," *Nuclear Technology*, vol. 206, pp. 150–163, Feb. 2020.

[60] V. Moreau, M. Profir, S. Keijers, and K. Van Tichelen, "An improved CFD model for a MYRRHA based primary coolant loop," *Nuclear Engineering and Design*, vol. 353, p. 110221, Nov. 2019.

[61] A. Toti, J. Vierendeels, and F. Belloni, "Coupled system thermal-hydraulic/CFD analysis of a protected loss of flow transient in the MYRRHA reactor," *Annals of Nuclear Energy*, vol. 118, pp. 199–211, Aug. 2018.

[62] M. Vanderhaegen, J. Vierendeels, and B. Arien, "CFD analysis of the MYRRHA primary cooling system," *Nuclear Engineering and Design*, vol. 241, pp. 775–784, Mar. 2011.

[63] V. Moreau, M. Profir, A. Alemberti, M. Frignani, F. Merli, M. Belka, O. Frybort, T. Melichar, M. Tarantino, S. Franke, S. Eckert, A. Class, J. Yanez, D. Grishchenko, M. Jeltsov, P. Kudinov, F. Roelofs, K. Zwijsen, D. Visser, A. Badillo, B. Niceno, and D. Martelli, "Pool CFD modelling: lessons from the SESAME project," *Nuclear Engineering and Design*, vol. 355, p. 110343, Dec. 2019.

[64] D. C. Visser, S. Keijers, S. Lopes, F. Roelofs, K. Van Tichelen, and L. Koloszar, "CFD analyses of the European scaled pool experiment E-SCAPE," *Nuclear Engineering and Design*, vol. 358, p. 110436, Mar. 2020.

[65] D. Visser, F. Roelofs, F. Mirelli, and K. Van Tichelen, "Validation of CFD analyses against pool experiments ESCAPE," *Nuclear Engineering and Design*, vol. 369, p. 110864, Dec. 2020.

[66] A. Cervone, A. Chierici, L. Chirco, R. Da Vià, V. Giovacchini, and S. Manservisi, "CFD simulation of turbulent flows over wire-wrapped nuclear reactor bundles using immersed boundary method," *Journal of Physics: Conference Series*, vol. 1599, p. 012022, Aug. 2020.

[67] A. Shams, F. Roelofs, E. Baglietto, and E. Komen, "High fidelity numerical simulations of an infinite wire-wrapped fuel assembly," *Nuclear Engineering and Design*, vol. 335, pp. 441–459, Aug. 2018.

[68] D. V. Fomichev and V. I. Solonin, "Structure of the turbulent flow in the BREST-OD-300 wire-spaced fuel assemblies," in *2015 5th International Youth Conference on Energy (IYCE)*, (Pisa, Italy), pp. 1–6, IEEE, May 2015.

[69] D. V. Fomichev and V. I. Solonin, "A CFD Analysis of Hydraulic Characteristics of the Rod Bundles in the BREST-OD-300 Wire-Spaced Fuel Assemblies," in *International Conference on Nuclear Energy Science and Technology (ICNEST)*, vol. 8, (Zurich, Switzerland), July 2014.

[70] I. Di Piazza, F. Magugliani, M. Tarantino, and A. Alemberti, "A CFD analysis of flow blockage phenomena in ALFRED LFR demo fuel assembly," *Nuclear Engineering and Design*, vol. 276, pp. 202–215, Sept. 2014.

[71] O. Bovati, M. A. Yildiz, Y. Hassan, and R. Vaghetto, "RANS simulations for transition and turbulent flow regimes in wire-wrapped rod bundles," *International Journal of Heat and Fluid Flow*, vol. 90, p. 108838, Aug. 2021.

[72] M. Song, J.-H. Jeong, and E. S. Kim, "Investigation on subchannel flow distribution in wire-wrapped 37 and 61-pin bundle using computational fluid dynamics," *Nuclear Engineering and Design*, vol. 370, p. 110904, Dec. 2020.

[73] F. Roelofs, H. Uitslag-Doolaard, D. Dovizio, B. Mikuz, A. Shams, F. Bertocchi, M. Rohde, J. Pacio, I. Di Piazza, G. Kennedy, K. Van Tichelen, A. Obabko, and E. Merzari, "Towards validated prediction with RANS CFD of flow and heat transport in a wire-wrap fuel assembly," *Nuclear Engineering and Design*, vol. 353, p. 110273, Nov. 2019.

[74] D. Dovizio, B. Mikuž, A. Shams, and F. Roelofs, "Validating RANS to predict the flow behavior in wire-wrapped fuel assemblies," *Nuclear Engineering and Design*, vol. 356, p. 110376, Jan. 2020.

[75] J. Martínez, Y.-H. Lan, E. Merzari, and M. Min, "On the use of LES-based turbulent thermal-stress models for rod bundle simulations," *International Journal of Heat and Mass Transfer*, vol. 142, p. 118399, Oct. 2019.

[76] V. Coppo Leite, E. Merzari, J. Mao, V. Petrov, and A. Manera, "High-Fidelity Simulation of Mixing Phenomena in Large Enclosures," *Nuclear Science and Engineering*, pp. 1–18, 2023. Publisher: Taylor & Francis.

[77] D. Shaver, A. Obabko, A. Tomboulides, V. Coppo-Leite, Y.-H. Lan, M. Min, P. F. Fischer, and C. Boyd, "Nek5000 developments in support of industry and the NRC," tech. rep., Argonne National Laboratory, United States, Sept. 2020.

[78] C. Reale Hernandez, D. Grishchenko, P. Kudinov, J. Wallenius, and J. Luxat, "Development of a CFD-based model to simulate loss of flow transients in a small lead-cooled reactor," *Nuclear Engineering and Design*, vol. 392, p. 111773, June 2022.

[79] C. Reale Hernandez, J. Wallenius, and J. Luxat, "Simulation of a loss of flow transient of a small Lead-Cooled reactor using a CFD-Based model," *Nuclear Engineering and Design*, vol. 412, p. 112462, Oct. 2023.

[80] J. Wallenius, S. Bortot, and I. Mickus, "Unprotected transients in SEALER: A small lead-cooled reactor for," in *PHYSOR 2018 Proceedings*, 2018.

[81] M. Gómez, *Porous Media Approach in CFD Thermohydraulic Simulation of Nuclear Generation-iv Lead-cooled Fast Reactor ALFRED*. PhD thesis, Politecnico di Milano, Milano, Italy, 2021.

[82] C. Howlett and A. Wimshurst, "Nuclear Heat Transfer and Passive Cooling: Technical Volumes and Case Studies," Tech. Rep. Study C, Frazer-Nash Consultancy, 2021.

[83] N. E. Todreas and M. S. Kazimi, *Nuclear Systems*, vol. I. CRC Press, 3rd ed., 2021.

[84] J. R. Lamarsh, *Introduction to Nuclear Reactor Theory*. Addison-Wesley Publishing Company, 2002.

[85] P. Spalart and S. Allmaras, "A One-Equation Turbulence Model for Aerodynamic Flows," *AIAA*, vol. 439, Jan. 1992.

[86] I. Celik, U. Ghia, P. Roache, and C. Freitas, "Procedure for Estimation and Reporting of Uncertainty Due to Discretization in CFD Applications," *Journal of Fluids Engineering*, vol. 130, no. 7, p. 078001, 2008.

[87] I. K. Umezu, A. L. Costa, D. M. Godino, and A. A. C. Santos, "CFD analysis of a wire-wrapped infinite sub-channel using temperature-dependent LBE properties," *Brazilian Journal of Radiation Sciences*, vol. 10, Oct. 2022.

[88] I. E. Idelchik, *Handbook of Hydraulic Resistance, 4th Edition Revised and Augmented*. Begell House Inc., 2008.

[89] A. Žukauskas, "Heat Transfer from Tubes in Crossflow," *Advances in Heat Transfer*, vol. 8, pp. 93–160, 1972.

[90] F. P. Incropera and D. P. Dewitt, *Fundamentos de Transferência de Calor e de Massa*. LTC, 5 ed., 2003.

[91] C. S. Kim, *Thermophysical Properties of Stainless Steels*. ANL-75-55, Argonne, Illinois: Argonne National Laboratory, 1975.

[92] J. J. Carbajo, G. L. Yoder, S. G. Popov, and V. K. Ivanov, "A review of the thermophysical properties of MOX and UO2 fuels," *Journal of Nuclear Materials*, vol. 299, pp. 181–198, Dec. 2001.

[93] T. S. Hunnewell, K. L. Walton, S. Sharma, T. K. Ghosh, R. V. Tompson, D. S. Viswanath, and S. K. Loyalka, "Total Hemispherical Emissivity of SS 316L with Simulated Very High Temperature Reactor Surface Conditions," *Nuclear Technology*, vol. 198, pp. 293–305, June 2017.

[94] F. N. Al Zubaidi, K. L. Walton, R. V. Tompson, T. K. Ghosh, and S. K. Loyalka, "The Effect of Long-Term Oxidation on the Total Hemispherical Emissivity of Type 316L Stainless Steel," *Nuclear Technology*, vol. 205, pp. 790–800, June 2019.

[95] S. K. S. Boetcher, *Natural Convection from Circular Cylinders*. SpringerBriefs in Applied Sciences and Technology, Cham: Springer International Publishing, 2014.

[96] E. M. Sparrow and J. L. Gregg, "Laminar Free Convection from a Vertical Plate With Uniform Surface Heat Flux," *Transactions of the American Society of Mechanical Engineers*, vol. 78, no. 2, pp. 435–440, 1956.

[97] Yunus A. Çengel and M. A. Boles, *Thermodynamics: An Engineering Approach*. Mcgraw-hill Series in Mechanical Engineering, McGraw-Hill, 5 ed., 2005.

[98] S. W. Churchill and H. H. Chu, "Correlating equations for laminar and turbulent free convection from a vertical plate," *International Journal of Heat and Mass Transfer*, vol. 18, pp. 1323–1329, Nov. 1975.

[99] C. A. da Silva, N. G. Oliveira, I. K. Umezu, A. L. Costa, and C. Pereira, "Neutronic evaluation of a small lead-cooled nuclear reactor as an actinides burner," *Nuclear Engineering and Design*, vol. 417, p. 112796, Feb. 2024.

Appendix A

Symmetry BC Applicability

This Appendix's goal is to present the applicability of the Symmetry Boundary Condition when modeling the SEALER as a 1/4 of the domain. Since it is a major modeling decision, as explained in Chapter 3, a detailed comparison between the SEALER models for the 1/4 (Quarter Model) and the 1/1 (Full Model) is carried out. The temperature and velocity results from both are visually compared and it is asserted that, for the intentions of this work, the employment of Symmetry BC to reduce the model to a 1/4 is adequate.

For his comparison study, the Full Model case was meshed and set up using the same parameters (i.e.: $\kappa-\epsilon$ turbulence model, coupled solver for steady and transient solutions, $CFL = 10$, PM coefficients, etc.) as the final Quarter Model, whose complete results are presented in Chapter 3. Tab. A.1 presents the main quality parameters for each case. The Full Model mesh size is about 4.4× larger than the Quarter Model, which is within the expected range.

Table A.1: Mesh quality parameters comparison.

	1/4 Model	**1/1 Model**
Number of Volume Cells	131,231	578,684
Minimum Orthogonal Quality	0.178	0.108
Average Orthogonal Quality	0.930	0.939
Maximum Aspect Ratio	78.495	89.776

For all the plane cuts and contours presented below, the Quarter Model's results are shown mirrored on the symmetry planes used, represented with the dash-dotted line, to allow for an equivalent comparison with the Full Model.

A.1 Temperature fields

Fig. A.1 and Fig. A.2 present the temperature contours on the XY and YZ planes, respectively. In both Figures, the symmetry in the Full Model is well captured in the Quarter Model, an understandable behavior given that those planes are mostly parallel to the outflow jets from the core. Fig. A.3 still captures this behavior, for being closer to the core's outlet. However,

a less symmetrical temperature distribution is observable in Fig. A.4, where the flow is likely disturbed by the pumps' lower pressure suction zones.

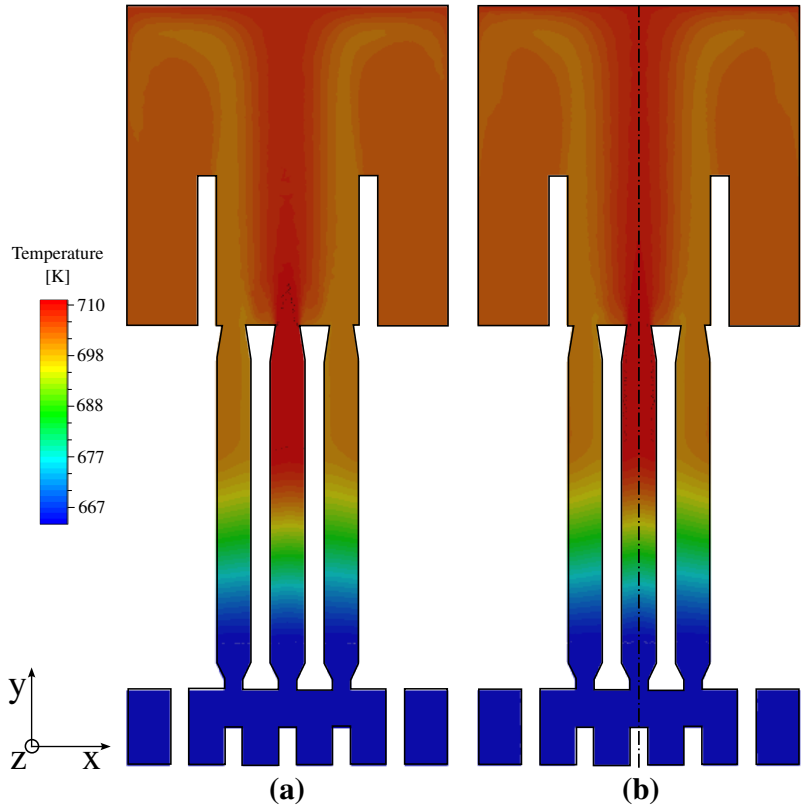

Figure A.1: Temperature contour on the XY plane. (a) 1/1 model and (b) 1/4 model.

For a quantitative measure, the volume-averaged temperature in the Hot Pool for the Quarter and Full Models are 703.315 K and 703.289 K, respectively. Considering that the absolute difference does not surpass 0.05 K and that the comparisons of the temperature distributions are not considerably distinct, the Symmetry BC can be considered appropriate for the temperature results.

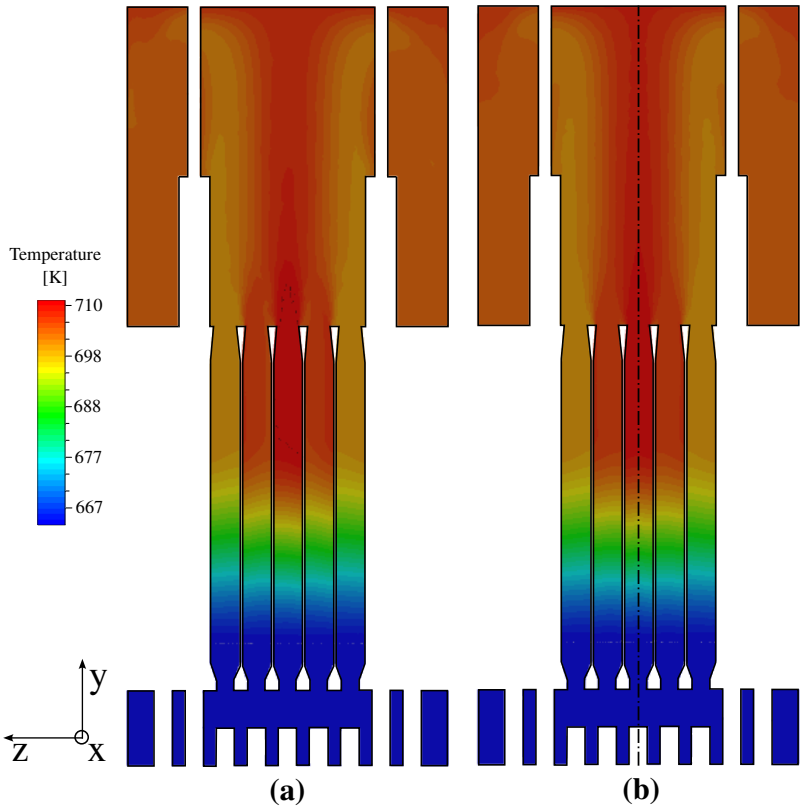

Figure A.2: Temperature contour on the YZ plane. (a) $^1/_1$ model and (b) $^1/_4$ model.

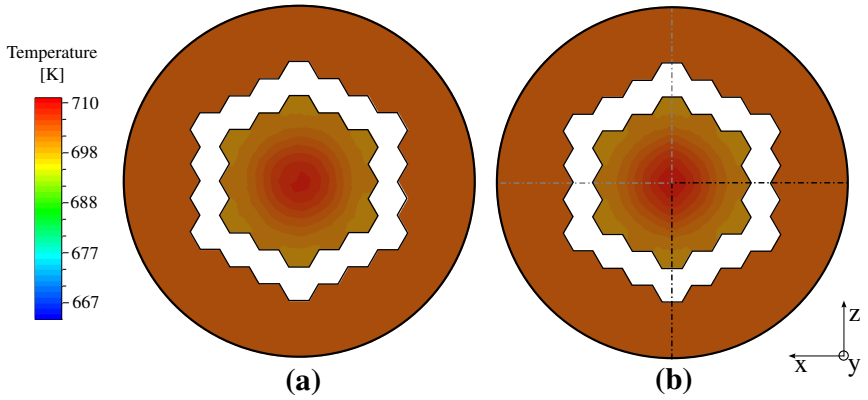

Figure A.3: Temperature contour on the $Y = 2.3\ m$ plane. (a) $^1/_1$ model and (b) $^1/_4$ model.

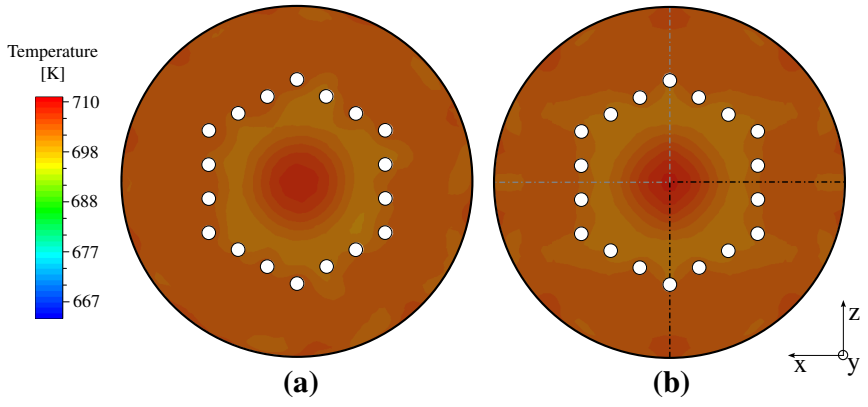

Figure A.4: Temperature contour on the $Y = 3.1\ m$ plane. (a) $^1/_1$ model and (b) $^1/_4$ model.

A.2 Velocity fields

For the velocity fields comparison, Fig. A.5 and Fig. A.6 present the velocity magnitude contours on the XY and YZ planes, respectively. Again, the symmetrical fields are still much present, under the same argument of the parallelism between the core's outflow jet direction and the planes themselves.

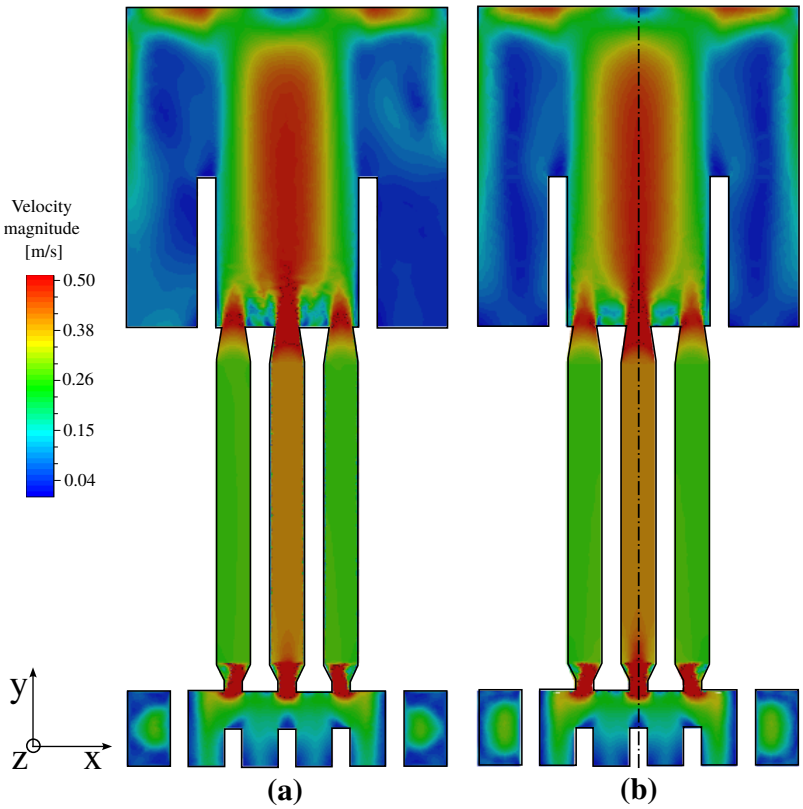

Figure A.5: Velocity magnitude contour on the XY plane. (a) $^1/_1$ model and (b) $^1/_4$ model.

Fig. A.7 presents the combined velocity magnitude and streamline fields on the $Y = -0.41\ m$ plane, located in the Cold Pool. The use of Symmetry BC in this region was the main point of concern raised in Chapter 3, since the cuts were not symmetrical when considering the placing of the inlets. This is very clear in the side-by-side comparison, where in Fig. A.7 (a) there is a well-distributed flow from the equally-spaced inlets, whereas in Fig. A.7 (b) there is a low-velocity region along the x axis, and high-velocity region along the z axis.

Despite these two major disparities, in both models, the velocity fields around the center region are similar, which is what matters the most in this study, since it is where the coolant flows into the modeled FAs. Nonetheless, if in a future SEALER model the outer core assemblies are included, the use of the Symmetry BC in this region should be reviewed, or avoided altogether.

Fig. A.8 and Fig. A.9 present the combined velocity magnitude and streamline fields on the $Y = 2.3\ m$ and $Y = 3.1\ m$ planes. Now with the aid of the streamlines, local imbalances in flow direction are visible, especially closer to the imposed symmetry planes, where the normal components of vector values are equated to zero. However, in terms of magnitude, both Figures

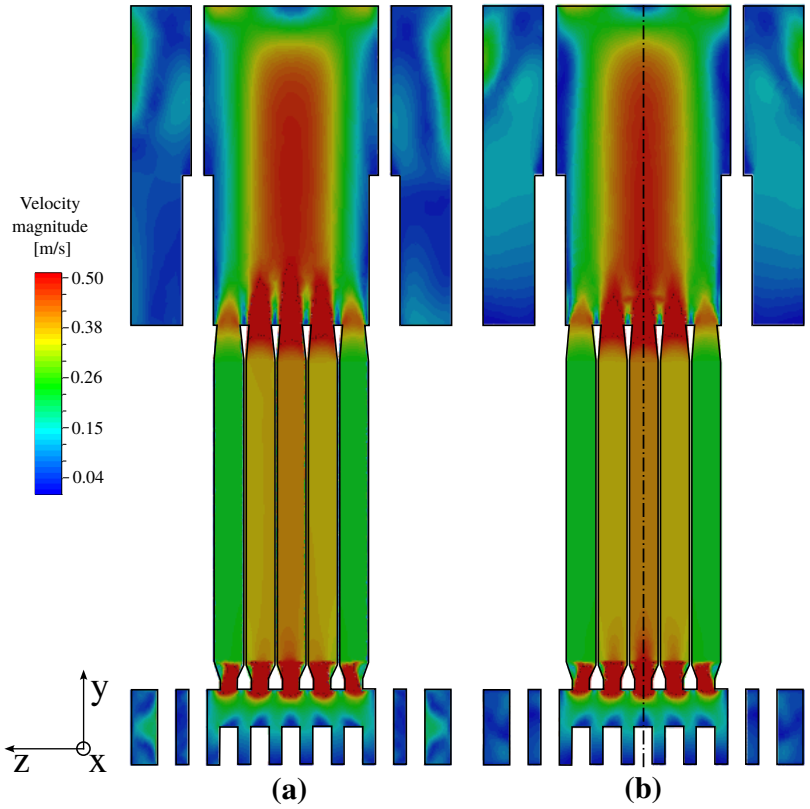

Figure A.6: Velocity magnitude contour on the YZ plane. (a) $^1/_1$ model and (b) $^1/_4$ model.

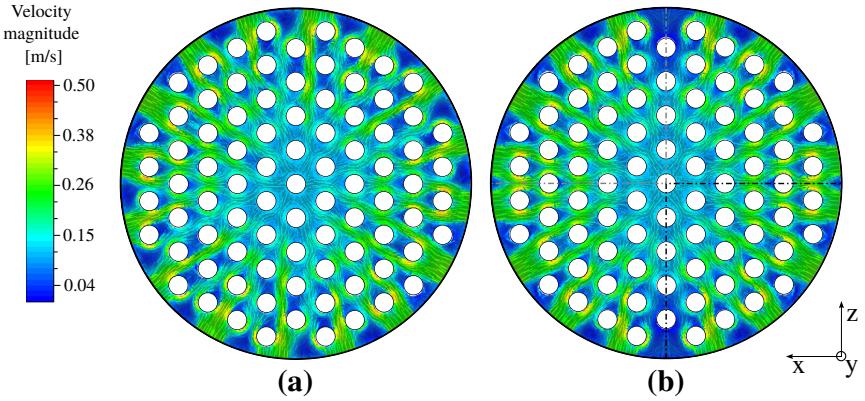

Figure A.7: Velocity magnitude contour and streamlines on the $Y = -0.41\ m$ plane. (a) $^1/_1$ model and (b) $^1/_4$ model.

show reasonable agreement.

Additionally, Fig. A.9 falls under similar conditions to the analysis made in Fig. A.7, where the pumps are not placed symmetrically (visible in the higher velocity spots, and where the streamlines point to). Still, when compared with the Full Model, the bulk behavior is mostly resembling. This shows that the pumps' placements do have an influence, however, reserved for the closer regions, thus not impacting the bulk flow.

In conclusion, the use of Symmetry BC as an approach to reduce a full $^1/_1$ model to a $^1/_4$ of its size was analyzed in this Appendix. Temperature and velocity field comparisons were used to show that, for this specific case, Symmetry BC can be considered adequate, since the observed

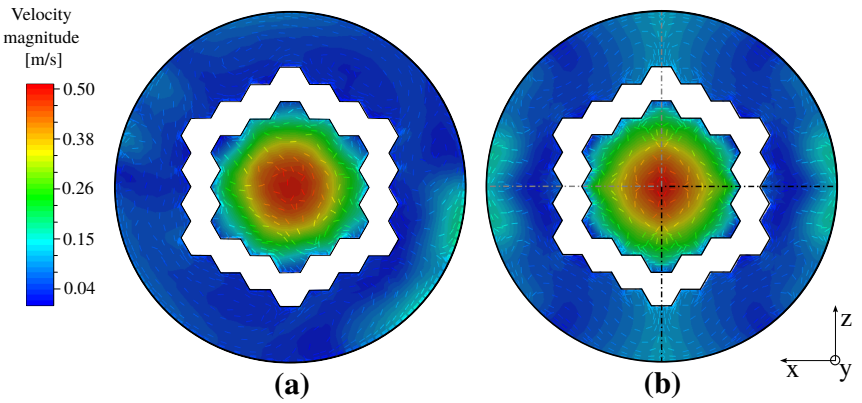

Figure A.8: Velocity magnitude contour and streamlines on the $Y = 2.3\ m$ plane. (a) 1/1 model and (b) 1/4 model.

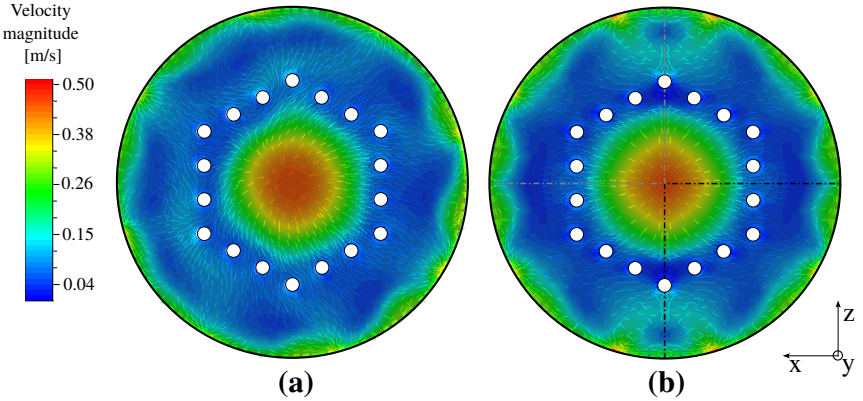

Figure A.9: Velocity magnitude contour and streamlines on the $Y = 3.1\ m$ plane. (a) 1/1 model and (b) 1/4 model.

differences are slight and localized. Given that the focus of the Core Barrel modeling was on the bulk flow and temperature results, the small compromises brought by the reduced model should be considered acceptable.